The POLARBEAR Cosmic Microwave Background Polarization Experiment and Anti-Reflection Coatings for Millimeter Wave Observations

by

Erin Elizabeth Quealy

A dissertation submitted in partial satisfaction of the

requirements for the degree of

Doctor of Philosophy

in

Physics

in the

Graduate Division

of the

University of California, Berkeley

Committee in charge:

Professor Adrian T. Lee, Chair

Professor William L. Holzapfel

Professor Geoffrey C. Bower

Fall 2012

The POLARBEAR Cosmic Microwave Background Polarization Experiment and Anti-Reflection Coatings for Millimeter Wave Observations

Erin Elizabeth Quealy

Abstract

The POLARBEAR Cosmic Microwave Background Polarization Experiment and Anti-Reflection Coatings for Millimeter Wave Observations

by

Erin Elizabeth Quealy

Doctor of Philosophy in Physics

University of California, Berkeley

Professor Adrian T. Lee, Chair

New technology has rapidly advanced the field of observational cosmology over the last 30 years. This trend will continue with the development of technologies to measure the Cosmic Microwave Background (CMB) polarization. The B-mode component of the polarization map will place limits on the energy scale of inflation and the sum of the neutrino masses. This thesis describes the POLARBEAR instrument which will measure the CMB polarization anisotropy to unprecedented sensitivity. POLARBEAR-I is currently observing, and an upgraded version, POLARBEAR-II , is planned for the future.

The first version of the experiment, POLARBEAR-I , is fielding several new technologies for the first time. POLARBEAR-I has high sensitivity due to its detector count. It employs a 1274 detector Transition-Edge Sensor (TES) bolometer array. The bolometers are coupled to a planar array of polarization sensitive antennas with contacting lenslets. The antennas are lithographed on the same substrate as the TES detectors, allowing on-chip band defining filters between the antenna and detector. The focal plane is composed of seven hexagonal detector modules. This modular scheme can be extended to create larger focal plane arrays in the future. POLARBEAR-I is observing at a single band near 150 GHz, the peak in the CMB blackbody curve.

The lenslet antenna coupled detector technology, fielding for the first time in POLARBEAR-I , is naturally scalable to larger arrays with multi-chroic pixels. This broadband technology will have higher sensitivity and better capability for astronomical foreground contaminant removal. The antenna geometry can be changed to receive a wider frequency bandwidth. This bandwidth can be broken into multiple frequency bands with the on-chip band defining filters. Each band will be read out by one TES detector. A dual band instrument, POLARBEAR-II , is in development with bands at 90 and 150 GHz.

One challenge for all CMB polarization measurements is minimization of systematic errors. One source of error is polarized reflections off of the refractive optics

inside the receiver. Specifically, the antenna-coupled detector scheme relies on a high dielectric lenslet for each pixel on the focal plane. A large portion of this thesis discusses development of anti-reflection (AR) coatings for the high curvature lenslet surface. The AR coating technologies discussed are also applicable to other optical elements, such as reimaging lenses and half-wave plates. A single layer coating is used on the POLARBEAR-I lenslet array, and a two layer coating is presented for use in POLARBEAR-II . The two layer coating method can be extended to wider bandwidth AR coatings.

Wtih gratitude to my numerous teachers
and
to my family, April, Tim, and Cristin.

Contents

List of Figures

List of Tables

Acknowledgments

I have had the great fortune to work with bright and interesting people during my time at Berkeley. My advisor, Adrian Lee, along with Professors Bill Holzapfel and Paul Richards have provided guidance, insight, and created opportunities for students to work on interesting projects. I have good memories of bouncing around wacky anti-reflection coating ideas with Adrian, learning most of thermodynamics from Bill in two intense sit-downs, and troubleshooting the Fourier Transform spectrometer with Paul. Along with them, I would like to acknowledge our late colleague Huan Tran who was a postdoc and project manager during my tenure. His mentorship had a tremendous impact on my graduate career and will be forever appreciated.

The POLARBEAR collaboration as a whole is responsible for the design and execution of the experiment. In particular, I would like to acknowledge the people I worked most closely with at Berkeley on POLARBEAR. Multiple invididuals made contributions to each part of the instrument, but significant contributions were made by Kam Arnold and Mike Myers on the antenna coupled bolometers and fabrication, Ziggy Kermish on the cryostat design and construction, and Bryan Steinbach on the half-wave plate. While not part of the POLARBEAR collaboration, Martin Lueker and Erik Shirokoff helped me with design and fabrication of the POLARBEAR LC boards, as did collaborator Helmuth Spieler. Mike Sholl provided me valuable knowledge of telescope optics. I would also like to acknowledge the work of the field team, including those I spent time in Cedar Flat with: Aubra Anthony, Dave Boettger, Daniel Flanigan, Nathan Miller, Haruki Nishino, Professor Hans Paar, Ian Schanning, and Chase Shimmin. I'd like to thank Professors Brian Keating and Nils Halverson for their responsiveness to my questions about projected sensitivity, systematics, and focal plane spacing.

I also worked closely with other students on the single frequency and broadband anti-reflection coatings. My undergraduate mentee, William Krantz, helped with fabrication of the POLARBEAR-I AR coatings, design of the production process, and is currently simulating AR coating performance on a curved surface. Thanks, Will, for making the hours in that overheated clean box more fun. Roger O'Brient and Aritoki Suzuki have made huge progress on the antennas and filters for broadband antenna-coupled bolometers, and they have both contributed significantly to the development of the broadband anti-reflection coatings. We also had assistance from past undergraduate Craig Peters, back in the first days of this project, and current undergraduate Darin Rosen who is working on the tunable dielectrics. Praween Siritanasak of UCSD helped with the most recent epoxy molding tests and will be taking over the POLARBEAR-II AR coating development.

I'd like to thank the larger research group. Sherry Cho, Matt Dobbs, and Trevor Lanting patiently trained me during my first months in the lab. Other group members who have taught me and entertained me include Brad Benson, Liz George,

Adnan Ghribi, Nick Harrington, Brad Johnson, Jared Mehl, Tom Plagge, Christian Reichardt, Dan Schwan, Yuki Takahashi, Ben Westbrook, and Oliver Zahn.

Many individuals in the UC Berkeley Physics Department also contributed to my success. I'd like to thank fellow physics graduate students Miguel Daal, Michelle Dolinski, and Sabrina Leslie for their peer mentoring and friendship. Thanks to Geoff Bower for serving as my outside committee member. Professors George Smoot, Frances Hellman, and Robert Littlejohn were helpful faculty mentors. Donna Sakima and Anne Takizawa helped me navigate the Berkeley system. The Physics machine shop has been a valuable resource; Marco Ambrosini, Dean Colomb, and Pete Thuesen in particular have helped us realize the anti-reflection coatings. Thanks to Anthony Vitan and the purchasing department for helping me obtain the needed equipment.

Finally, I'd like to acknowledge those who helped me secure my next position. My advisor, Adrian, called my future employers from a mountain top in Chile. Professor Bob Jacobsen and Dr. Jody Lewen were also proactive references. I got a lot of good advice from Andrew Green, Xiaosheng Huang, Peter Hyland, Christopher Johnson, Rich Mueller, and Brian Welch. Thanks also to Roberto Barrueto and James Little of the UC Berkeley Lecture Demonstration department.

The POLARBEAR project is funded by the National Science Foundation under grant AST-0618398. Antenna-coupled bolometer development at Berkeley is also funded by NASA under grant NNG06GJ08G. Broadband anti-reflection coating research was supported this summer by the Student Mentoring and Research Teams (SMART) Pilot Project at UC Berkeley.

Chapter 1

The Cosmic Microwave Background as a Cosmological Tool

The field of cosmology has rapidly progressed over the last 30 years due to precision measurements of the Cosmic Microwave Background (CMB), supernovae luminosity measurements, and observed light element abundances in agreement with Big Bang nucleosynthesis. Together these data form a picture of the universe and its evolution in agreement with a ΛCDM Hot Big Bang cosmological model. This model describes a universe with significant mass fractions of Dark Energy and Dark Matter. The nature of Dark Energy and Dark Matter are not understood at this point, and their existence is one of the biggest puzzles in contemporary physics. [22] [71]

As the oldest observed cosmic signal, the CMB has great potential to unlock these puzzles. Future measurements of CMB polarization anisotropies will help advance the field of cosmology by constraining:

- Inflationary models
- The sum of neutrino masses
- The dark energy equation of state

This chapter describes the CMB formation, temperature and polarization anisotropies, and the information to be gained from CMB measurement.

1.1 Formation of the CMB

The observed CMB is understood to be relic radiation initially produced in a hot Big Bang. As the oldest observable source of electromagnetic radiation, it is clearly a tool with which to study the early universe and its evolution.

The current CMB observations are in excellent agreement with a hot Big Bang model which includes inflation. [22] [71] In this model, the universe begins with a

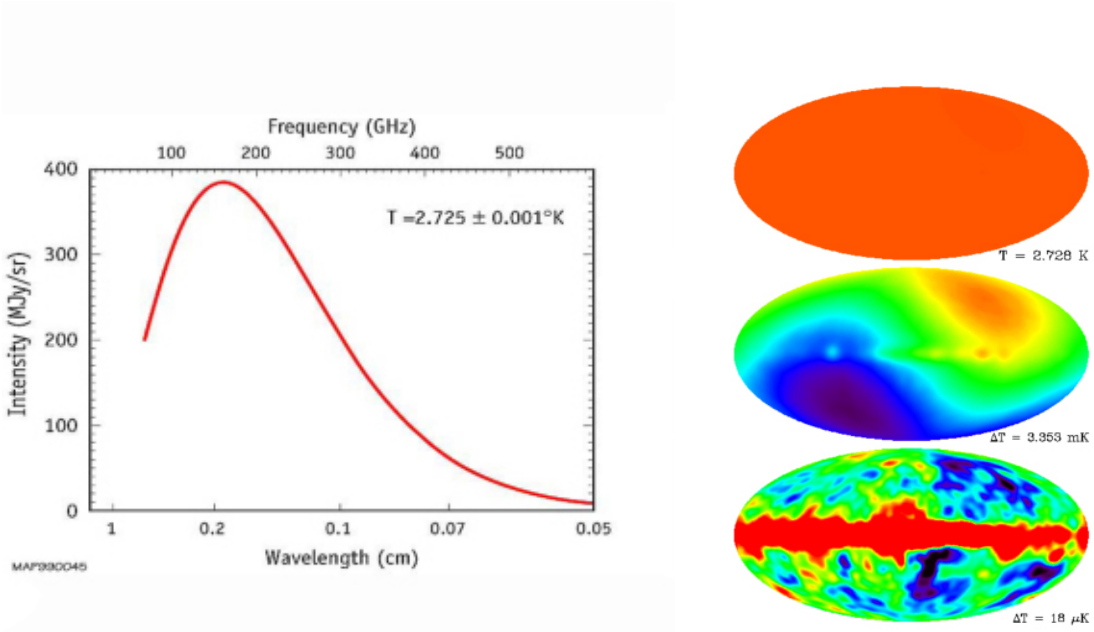

(a) (b)

Figure 1.1: COBE Satellite CMB Measurements. (a) The observed CMB spectrum as seen by COBE FIRAS, where the data point error bars are smaller than the width of the blackbody fit. [63] (b) COBE DMR measurement of the temperature map. The temperature scales are set so that (from top to bottom) we observe the isotropy of the CMB, the observer's motion with respect to the CMB, and CMB temperature anisotropies. [11]

hot, dense Big Bang, where generated energy is in the form of mass (particles) and radiation. The matter is ionized, so it couples electromagnetically to the background radiation, forming a photon-baryon fluid. This coupling ensures a thermalized universe. As the universe expands and cools, the kinetic energy of the ionized matter is reduced, so electrons can be captured by protons to form hydrogen (helium is also formed in smaller quantities). With the formation of atoms, there is less ionized matter for the electromagnetic radiation to interact with. Additionally, the average distance between particles increases with expansion, and photons are therefore less likely to interact with matter due to the low number density of particles. These two effects conspire so that, within a time window, radiation decouples from matter. This is referred to as the *surface of last scattering*. Between the surface of last scattering and our observation of the CMB, the photons are redshifted by cosmic expansion, but they otherwise are predominantly unaffected by interactions along their path.

The CMB we measure is homogeneous to 1 part in 100,000 across the sky and follows a blackbody curve. Measurements from the COBE satellite displaying this are shown in Figure 1.1. To explain this homogeneity, it is necessary that the observable

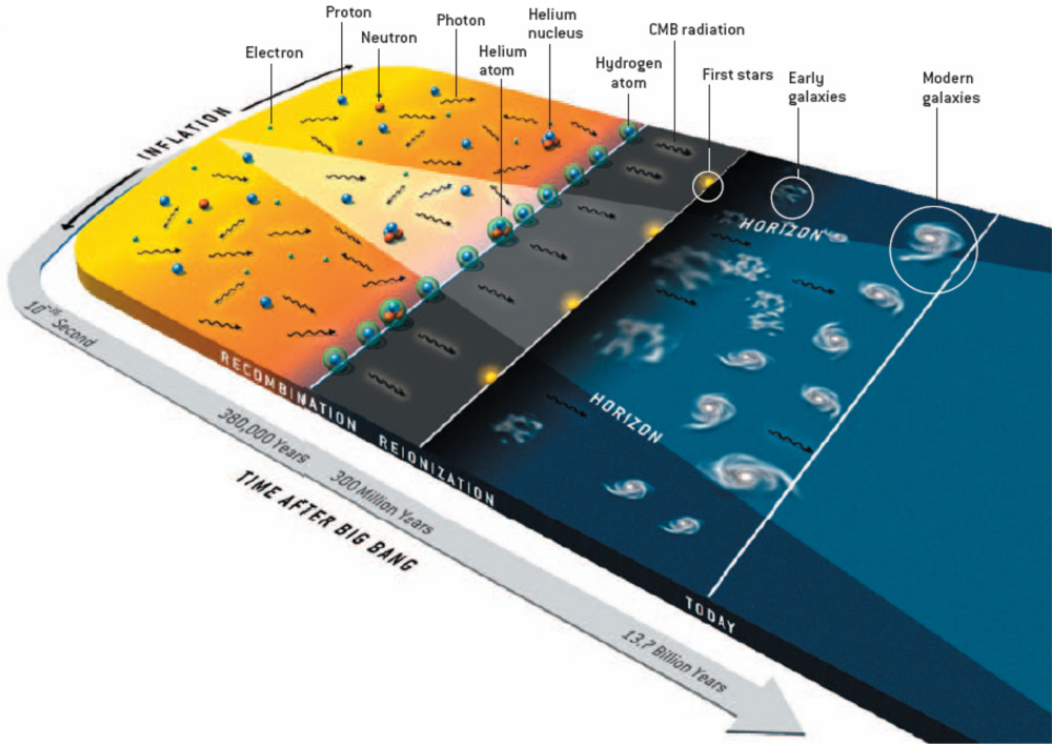

Figure 1.2: Evolution of the universe. This cartoon shows the evolution of the universe with a time axis. The Big Bang is at the time origin, and inflation, the formation of atoms, and recombination (which is temporally close to the surface of last scattering) are shown. Figure from [39]

universe was once in causal contact and thus able to thermalize. This thermalization was preserved to span the horizon we currently observe. This issue, called the *horizon problem*, is explained by the theory of inflation.

Inflation postulates superluminal expansion of spacetime in the very early universe. Inflationary expansion is faster than the speed of light. The causal horizon (in comoving coordinates) therefore shrinks during inflation, solving the horizon problem. Figure 1.2 illustrates the phases of the universe and the associated timescales.

1.1.1 Formation of the CMB temperature anisotropy

Aside from solving the horizon problem, inflation also predicts inhomogeneities in the observed CMB at approximately one degree and smaller scales. Quantum mechanical fluctuations in the gravitational potential are stretched to macroscopic scales by inflation. Thus, there are gravitational potential peaks and troughs which attract and repel matter and radiation. These variations set density waves in motion in the photon-baryon fluid. A spring analogy is commonly used to illustrate this, see for

example Wayne Hu's tutorial material [37], where the existing potential fluctuations and self gravitation of matter are opposed by radiation and thermal pressure.

At the surface of last scattering, we observe increments and decrements in observed power, depending on whether the radiation is coming from a compressed or rarefied region of space. These temperature variations are due to photons being redshifted as they climb out of gravitational potential wells and blueshifted as they leave peaks. The physical size of the potential well compared to the age of the universe at last scattering dictates whether a scale, or mode, is able to effect the CMB. For example, a mode that is physically larger than the horizon at the time of decoupling will not have had a chance to compress or rarefy, and this mode will leave no observable imprint on the CMB. Conversely, if a fluctuation is physically small enough so that there are many cycles of compression and rarifaction, frictional forces will damp that mode and reduce the strength of that signal. The strongest temperature anisotropy happens at a scale where the CMB photons only compress or rarify one time between inflation and the surface of last scattering. This anisotropy happens at an angular scale which corresponds to the *primary* peak in the CMB anisotropy. Figure 1.7 shows the temperature map scaled to view the anisotropies. The map is decomposed into spherical harmonics, with a primary peak occurring at multipole $l = 200$, which corresponds to one degree.

1.1.2 Formation of the CMB polarization anisotropy

Another prediction of inflation is the existence of gravitational waves at the surface of last scattering. These *primordial gravitational waves* are represented by tensor perturbations to the gravitational metric, whereas temperature anisotropies are associated with scalar perturbations. Both types of perturbations cause CMB polarization anisotropies. [38]

Net polarization of the CMB is caused by the Thomson scattering, i.e. the scattering of a photon off of a charged particle. The Thompson cross section, or radiation scattered per solid angle, is

$$\frac{d\sigma}{d\Omega} \propto |\hat{\epsilon} \cdot \hat{\epsilon}'|^2 \tag{1.1}$$

where $\hat{\epsilon}$ and $\hat{\epsilon}'$ are the polarization vectors of the incident and scattered radiation respectively. This formula shows that no radiation is scattered with polarization perpendicular to the incident polarization. Using the Thomson cross section, Figure 1.3 shows how net polarization is generated by a quadrupole anisotropy. For simplicity, only one quadrant of the quadrupole is illustrated. This quadrant mirrored left to right and top to bottom would represent the full quadrupole.

Anisotropies about a given point can be decomposed into spherical harmonics. Net polarization is produced solely by quadrupole terms, i.e. spherical harmonics $\mathrm{Y}_2{}^{\mathrm{m}}$. [48] The $m = 0$ mode corresponds to scalar perturbations of the metric and

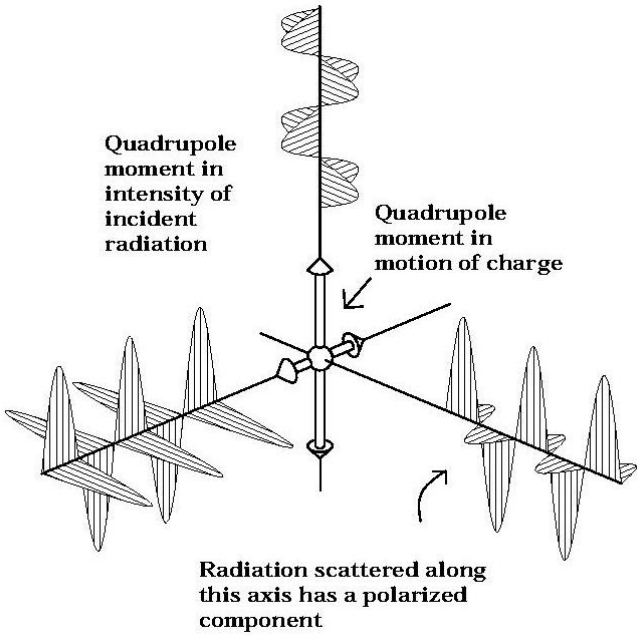

Figure 1.3: Generation of CMB polarization anisotropy. The Thomson cross section dictates the dependance of scattered radiation on the incident polarization. Here, we see unpolarized radiation from incident on a free electron from above and to the left. The signals have different intensity, thus the transmitted radiation along the third axis has a net polarization in the vertical direction. Figure courtesy of CAPMAP team at University of Chicago. [18]

the $m = 2$ mode corresponds to tensor perturbations (gravitational waves). These modes are illustrated in Figure 1.4.

The net observed signal is a super position of these modes across the sky. These polarization maps can be decomposed into modes with even and odd parity, called E-modes and B-modes. The nomenclature comes from an analogy to the E- and B-vector fields of electromagnetism, which are curlless and divergenceless respectively. Figure 1.5 illustrates these modes.

E-modes are generated by scalar and tensor perturbations whereas B-modes are generated solely by tensor perturbations. To see this, we must consider the projection of the modes across a sky. For a single plane wave perturbation, the angle between the line of sight and the mode wavevector, $\vec{k}$, varies across the sky. The azimuthal angle of the observer with respect to the perturbation also varies. Figure 1.6 illustrates specific examples of this for scalar and tensor perturbations.

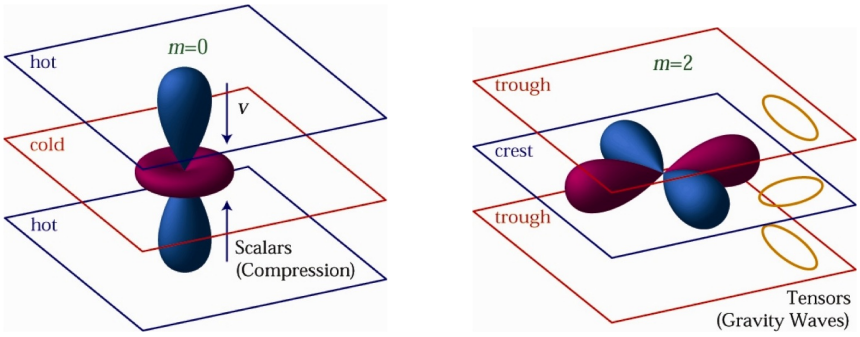

(a) (b)

Figure 1.4: Quadrupole anisotropies. Perturbations represented by the spherical harmonic terms $Y_2{}^m$ cause CMB polarization. (a) Scalar perturbations, $m = 0$, correspond to a compressional wave where the relative velocities are labeled. (b) Tensor perturbations, $m = 2$ also contribute. The incident quadrupole in the latter case is caused by compression and decompression in orthogonal directions, with relative velocities implied by the yellow ellipses. [38]

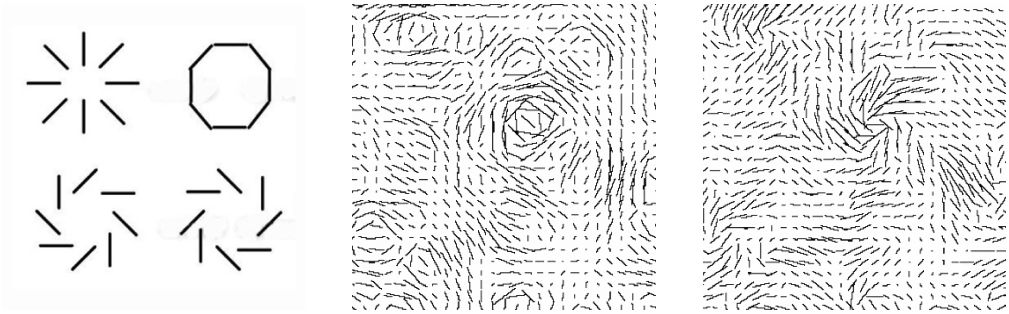

(a) Divergence and Curl (b) Pure E-mode (c) Pure B-mode

Figure 1.5: E-modes and B-modes. (a) Schematic vector fields with no curl (top) and no divergence (bottom). Here arrows on the vector field have been omitted to symbolize direction only, as polarization intensity maps show. (b) An example polarization field with no curl, representing an E-mode map. (c) An example polarization field with no divergence, representing a B-mode map. Maps adapted from talk by Bruce Winstein, University of Chicago.

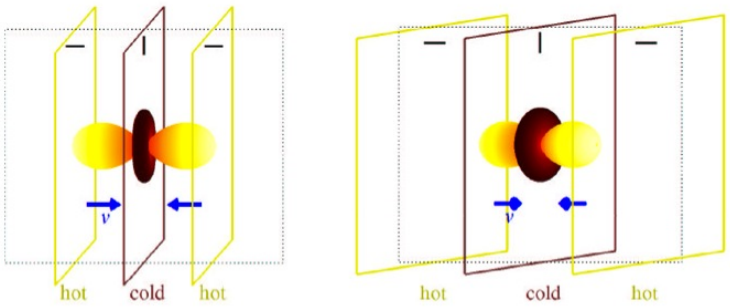

(a) Scalar perturbation

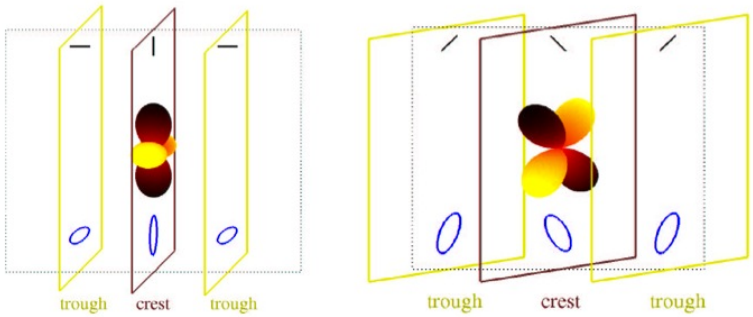

(b) Tensor perturbation

Figure 1.6: Scalar and Tensor Modes on the sky. (a) The scalar mode generates polarization parallel or perpendicular to the mode wavevector $\vec{k}$ (left panel). Consider this mode at a different angle to the observer, for example rotated 45° out of the page, as shown on right. If the mode is now rotated about the $\hat{k}$ axis, the observed polarization is still parallel or perpendicular to the wavevector projected into the plane of the page, $\vec{k}_{\rm proj}$. Thus, the scalar perturbations produce E-modes. (b) The vector perturbations produce the a similar parallel or perpendicular pattern (on left) as the scalar perturbations. However, when viewed from a different angle (on right), we see that the perturbation is not axially symmetric. Rotation of this perturbation about the $\hat{k}$ axis leads to cross terms in the polarization, so this mode will have curl when projected across the sky. Thus, projected across the sky, tensor perturbations will generate E- and B-modes. Figure from [49].

1.2 Information contained in the CMB

The temperature and polarization anisotropies constrain many cosmological parameters which factor into cosmological models. To extract these parameters from a sky map, the variations in temperature and polarization maps are Fourier transformed into a power spectrum, which displays fluctuation power at various angular scales. This power spectrum is fit to a cosmological model, and the best fit values of the model parameters are reported.

1.2.1 Information in the CMB temperature anisotropy

The WMAP satellite made a high precision measurement of the temperature anisotropies. The finalized temperature map and power spectrum is shown in Figure 1.7. Analysis of the WMAP data (in conjunction with distance measurements of the Hubble constant and baryon acoustic oscillations in the distribution of galaxies) yielded stringent bounds on the simplest six-parameter ΛCDM model. From this, relevant cosmological parameters were calculated, as summarized in Table 1.1. [47]

The most intuitive and fundamental parameters constrained by the temperature power spectrum include the following: [37]

- Curvature. The first peak in the CMB angular power spectrum has a size based on the size of the horizon at the time of decoupling. From the surface of last scattering, the photons traverse space. Depending on the curvature of the universe, rays from the spot could converge or diverge. The observed scale of the first peak indicates a flat universe, where parallel lines remain parallel as they traverse space. Current measurements are consistent with a flat universe.

- Baryon Mass Fraction. Acoustic oscillations cause the series of peaks in the CMB. The first peak is the result of a perturbation which compresses the photon-baryon fluid once, through gravitational forces on the baryons. The second peak corresponds to a smaller scale which had the time to compress once and rebound by radiation pressure. The series continues with the odd peaks ending on compression and the even peaks ending on rebound. Increasing the baryonic matter changes the zero point of this oscillation, enhancing the odd peaks relative to the even peaks. Thus, the height of the second peak can be said to indicate Ω_{b}. Current measurements indicate $\Omega_{\mathrm{b}} = 0.0449 \pm 0.0028$. [47]

- Dark Matter Mass Fraction. Dark matter interacts gravitationally, but not electromagnetically. Thus, dark matter presents a drag force on rebounding acoustic oscillations. The drag force has a greater effect with the number of oscillations a mode under goes, so dark matter damps oscillations at smaller scales. The height of the third peak relative to the first is an indicator of

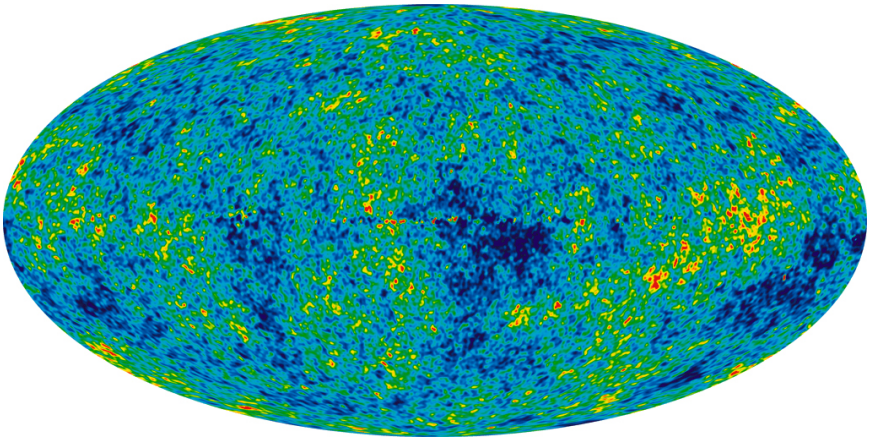

(a)

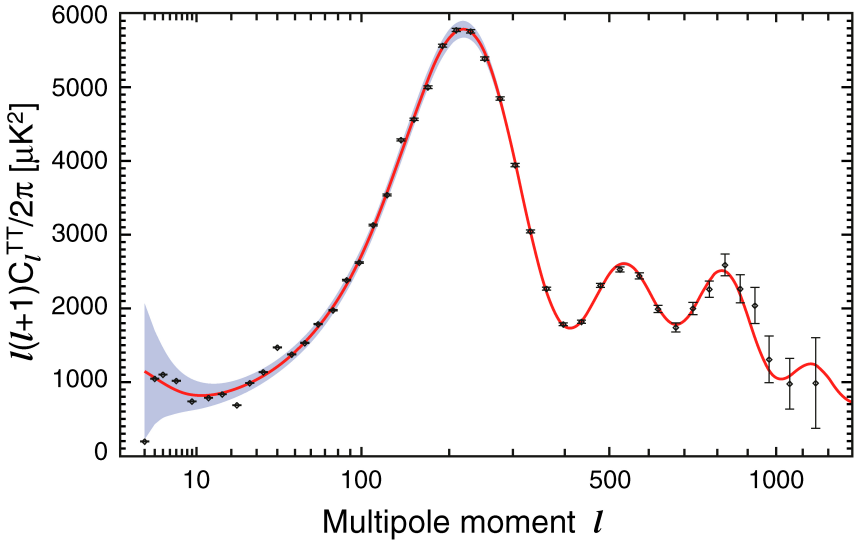

(b)

Figure 1.7: WMAP 7-year data. (a) WMAP observed temperature map across the full sky. Here, the color scale is set in reference to the 2.7 Kelvin average temperature. The range of the color scale is ± 200 μK. This map is a linear combination of maps taken at five wavelengths to minimize galactic foreground emission. *(Internal Linear Combination Map, courtesy of WMAP Science Team)* (b) The temperature map was decomposed into spherical harmonics, and fluctuation power is plotted as a function of multipole moment (the reciprocal of spot size). [56].

Table 1.1: WMAP 7-year analysis results from Komatsu et. al (2011).

Parameter	Value	Description
$100\Omega_{\rm b}h^2$	$2.258^{+0.057}_{-0.056}$	Baryon density
$\Omega_{\rm CDM}h^2$	0.1109 ± 0.0056	Cold Dark Matter density
Ω_Λ	0.734 ± 0.029	Dark Energy density
Ω_k	$0.080^{+0.071}_{-0.093}$	Curvature density
$n_{\rm S}$	0.964 ± 0.0114	Scalar Spectral Index
r	< 0.36 (95% confidence)	Tensor Scalar Ratio
Σm_ν	< 1.3 eV (95% confidence)	Neutrino mass sum
$t_{\rm o}$	13.75 ± 0.13 Gyr	Current age of the universe
$H_{\rm o}$	71.0 ± 2.5 km/s/Mpc	Current Hubble parameter

the dark matter mass fraction, $\Omega_{\rm CDM}$. Current measurements indicate $\Omega_{\rm CDM} = 0.222 \pm 0.026$. [47]

- Scalar Spectral Index. The power in the initial scalar perturbations may depend on the size of the perturbations. For a flat, or scale-invariant, power spectrum, the scalar spectral index, $n_{\rm S} = 1$. For $n_{\rm S} < 1$, there is less power in smaller modes. This will have the effect of reducing the observed CMB power spectrum at high l, and causes a tilt in the CMB power spectrum. WMAP found $n_{\rm S} = 0.964 \pm 0.0114$. [47]

1.2.2 Information in the CMB polarization anisotropy

Similar to the temperature map, the E-mode and B-mode polarization maps are separated and decomposed into spherical harmonics in order to extract cosmological parameters. Figure 1.8 shows a compilation of E- and B-mode measurements. The E-mode measurement shows the best fit power spectrum. Since B-modes have not been detected, theoretical curves are shown along with the B-mode upper limit data.

The scalar perturbations which source the temperature anisotropy also cause the compressional waves responsible for E-mode generation. Since the density and velocity of these waves are out of phase, the TT (temperature auto-correlation) and EE (E-mode auto-correlation) spectra are directly out of phase. The correlation between the two, the TE power spectrum, shows this. The TE and EE measurements are significant as they confirm the standard cosmological model.

As seen in Figure 1.8, only upper limits have been placed on the B-mode spectra, and detecting B-modes is the goal of current CMB measurements. As seen in the BB panel of the figure, the B-modes have components from two sources: primordial tensor perturbations and gravitational lensing of E-modes.

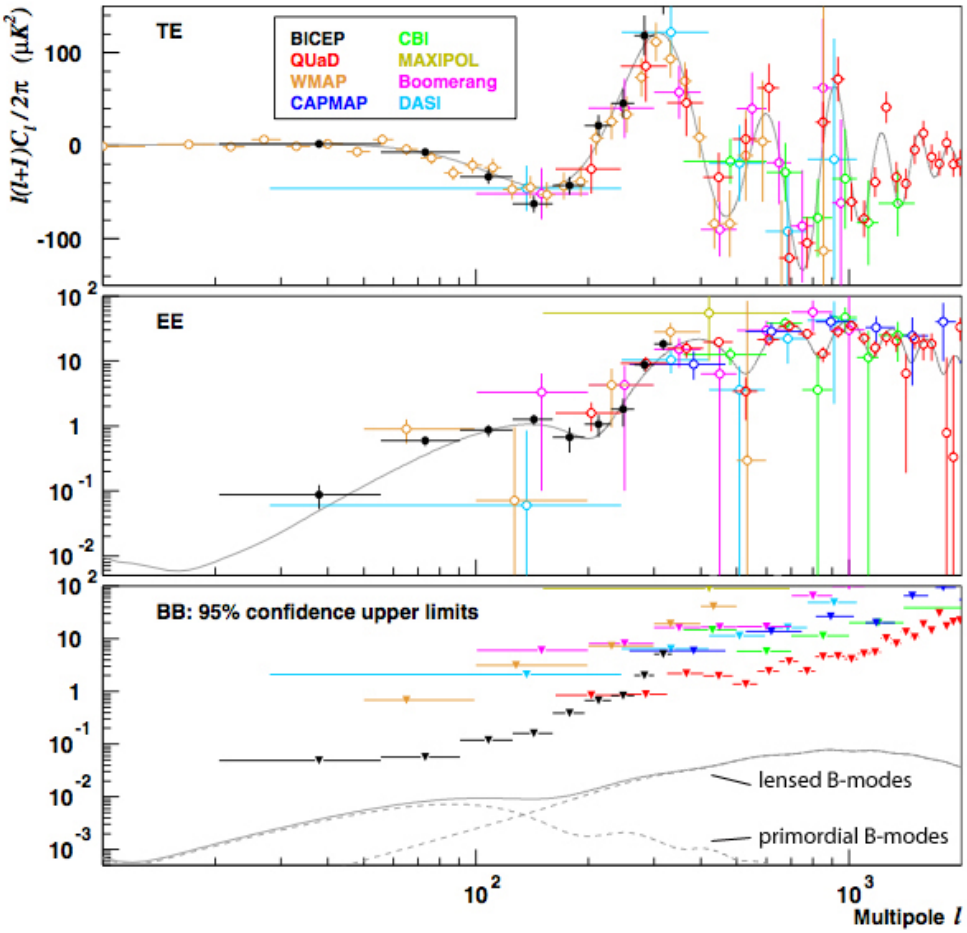

Figure 1.8: CMB polarization measurements. From top to bottom, the TE, EE, and BB power spectra measurements and best fit curves are shown. The B-mode, BB, spectra has two components shown in dashed lines. At low l, the B-modes from primordial gravitational waves dominate. Here, the primordial BB signal is shown for $r = 0.1$. At high l the B-modes from lensing dominate. The observable signal is the sum of these effects, shown in the solid grey line. The BB spectra has not been detected, and the upper limit set by BICEP yields $r < 0.72$ at 95% confidence. This upper bound was lowered by WMAP in combination with other datasets to $r < 0.2$. [47] Figure modified from [19].

The B-mode signal level of the primordial tensor waves depends on the relative power of tensor and scalar perturbations. The amplitude of this contribution to theoretical B-mode plots thus depends on the tensor to scalar ratio, $r \equiv T/S$. This ratio is a parameter in inflationary models, and if this parameter is large enough, primordial B-modes will be observable. WMAP data, along with supernova type Ia, and baryon-acoustic oscillations, yields the most strict upper bound on this parameter, $r < 0.2$ at 95% confidence. [47]

Detection of the tensor modes is considered proof of inflationary theory, and the B-modes have often been called a smoking gun of inflation. The measured r value would help constrain theoretical inflationary models, including the mechanisms for and energy scale of inflation. This energy scale may be related to the grand unification (GUT) scale $\approx 10^{15}$ GeV. The simplest single-field inflation models have an energy scale which is of order

$$V^{1/4} \approx (\frac{r}{0.1})^{1/4}(10^{16} GeV) \tag{1.2}$$

Thus, a detection of $r = 0.1$ corresponds to an inflationary energy scale of 10^{16} GeV. [61] [9]

Many models of inflation yield an r value which will render the primordial B-modes undetectable. If primordial B-modes are not detected, the result will still rule out many classes of inflationary models. [8] [9]

At scales of $l \gtrsim 100$ (depending on the tensor to scalar ratio), the primordial B-modes are dominated by a B-mode signal due to lensing. The comparatively larger primordial E-modes are lensed into B-modes. [60] While the lensed signal unfortunately obscures a primordial B-mode signal for large values of l and small values of r, the lensed signal is scientifically interesting. The lensed signal is related to structure formation, and it is dependent on the the dark energy equation of state and sum of the neutrino masses. [84] [17] [41]

Characterizing the B-mode signal is at the forefront of our field. As discussed, B-mode detection will constrain inflationary theories (the energy of which may be related to the GUT scale). The lensed signal will further constrain the sum of neutrino masses, and has the potential to give us insight into the nature of dark energy. The following chapter describes the strategy for making this measurement and the associated instrumental challenges.

Chapter 2

CMB Polarization Measurement

Precision measurements of the CMB polarization anisotropy have great scientific potential as motivated in Chapter 1. Goals of future CMB polarization experiments include characterizing the B-mode lensing signal at high l, for science in its own right and so it can be subtracted from a low l primordial B-mode signal. Limits will be placed on primordial B-modes, or they will be detected, depending on the value of the tensor to scalar ratio, r. Instruments will be designed to achieve the high sensitivity needed to detect or exclude low power B-mode signals which correspond to small r values.

This chapter outlines the strategies to achieve this high sensitivity measurement. We begin by describing considerations for a single frequency instrument, POLARBEAR-I . POLARBEAR-I is currently fielding in Chile after completing its engineering run at Cedar Flat, California in late 2010. Further details of the POLARBEAR-I telescope and receiver are presented in Chapter 3. Future versions of this experiment, e.g. POLARBEAR-II or satellite missions, will use the similar design principles with added technology of multichroic pixels. This broadband technology will allow foreground removal and increased mapping speed.

2.1 Single Frequency Measurement (POLARBEAR-I)

2.1.1 Signal to Noise

Thermal radiation sources have an intrinsic statistical source of noise dictated by quantum mechanics. In order to have a high signal to noise ratio, all other sources of noise should be subdominant to the photon noise. [78] In a ground-based experiment, thermal emission by the comparatively hot atmosphere dominates the photon noise. In a satellite system, it is possible to be limited by the photon noise of the CMB itself.

The use of sub-Kelvin detectors and a cold amplification stage allows reduction of thermal Johnson noise in the system. The POLARBEAR-I detectors, supercon-

ducting transition-edge sensor bolometers, are shown to be photon noise limited for detection of CMB signals. [92] [75] These detectors are discussed further in Section 3.3. The electrical signal is amplified at a cold stage using superconducting quantum interference devices (SQUIDS). The cold amplification is discussed in Section 3.4.2.

To reduce observation time, many detectors are used to integrate the signal rapidly. POLARBEAR uses a lithographed detectors and antennas, which naturally scale to kilo-pixel arrays. This scalability is a large driver in the development of our antenna-coupled bolometers. Section 3.3 describes this technology.

2.1.2 Sidelobes and Ground Pickup

Due to diffraction and diffuse reflections, there is always some power directed out of the main lobe of the telescope beam. Reflections occur throughout the optical path, with both a specular term (following the law of reflection) and a diffuse term which scatters at wide angles. Diffraction occurs in the system at the edges of the beam, for example at cold aperture stops and the edge of mirrors. The telescope geometry was selected for low sidelobe response (see 3.1), and additional baffling be either a fixed or comoving ground screen can further aid sidelobe reduction.

If sidelobes end up on the sky, the suppression due to the beam profile is sufficient to make these negligible. However, if the sidelobes hit the ground or other 300 Kelvin objects, the power in the sidelobes compared to the CMB, or CMB anisotropies, can be significant. Worse yet, signals generated via ground pickup are scan synchronous, making them difficult to subtract from true CMB.

For polarization measurements, removal of sidelobes is all the more important, since the polarization anisotropies are small, and sidelobes are polarized. We estimate 10% variation in the ground temperature, which yields a ground signal of 10 K. We hope to detect B-mode polarization estimated to be three orders of magnitude smaller than the temperature anisotropy measurement. [42] The desired POLARBEAR sensitivity is then 10^{-7} Kelvin. Therefore, we need at least -80 dB to -100 dB suppression of the ground signal.

Reflection and diffraction both induce polarization signals. The dependence of reflection on polarization is predicted by the Fresnel equations; see section 4.1.2. The dependence of diffraction on incident polarization can be analytically calculated via the geometrical theory of diffraction (GTD). GTD is a ray approximation to the full analytic solution, where rays couple to surfaces according to the appropriate boundary condition. In this theory, the electric field is treated as a scalar. Thus for each problem there are two solutions corresponding to two independent polarizations of the incoming wave.

Features on the scale of the wavelength tend to cause diffraction. For this reason, CMB observations have traditionally minimized diffraction effects by using horn antennas with flared edges, where the flare radius of curvature is large compared to the wavelength. [62] Using GTD, we can calculate the diffracted power a curved this

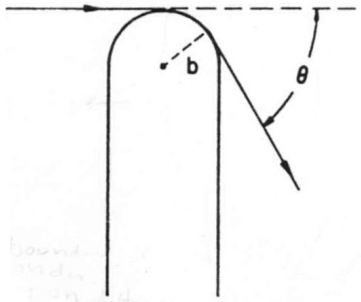

Figure 2.1: Curved Edge Geometry. The intensity of the diffracted pattern can be calculated for a ray normal to a curved edge of radius b and an angle θ. Here, the edge is in cross section and it has infinite extent along the axis out of the page. [44]

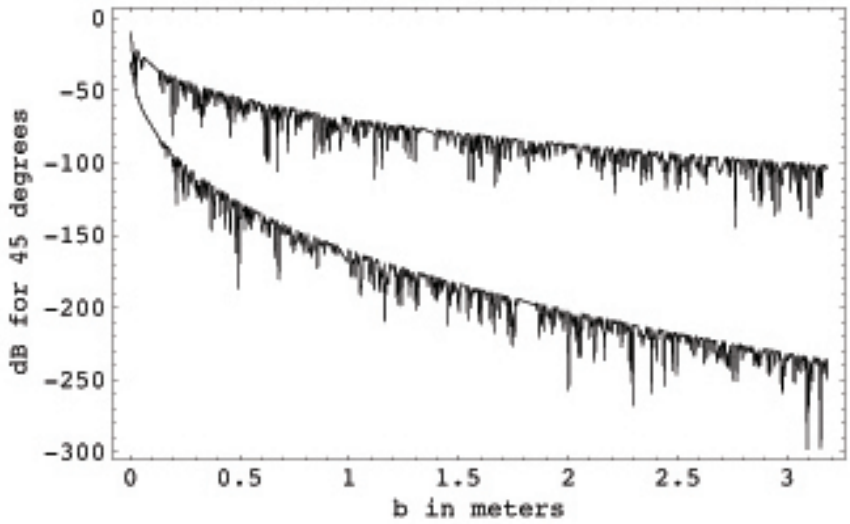

Figure 2.2: Suppression due to diffraction vs. flare radius. The suppression for diffraction over a flared edge is plotted as a function of the flare radius b for angle $\theta = 45$ degrees, calculated according to the method detailed in [44] . The vertical lines are an artifact of the computation method. The higher trend line is the solution for the E-field vertical in Figure 2.1. The lower trend line is the solution for the E-field normal to the page in Figure 2.1.

edge, according to Keller's method. [44] The geometry of this edge is shown in Figure 2.1.

Figure 2.2 shows the result of the diffraction calculation at an angle 45 degrees from the incident direction. As shown by the two curves, on polarization is suppressed by diffraction more than the other. Thus, diffracted power by unpolarized light will be strongly polarized.

The BICEP experiment dealt with polarized sidelobes by imposing a double diffraction criteria for their optical system. That is, any ray incident from the ground would need to diffract twice to reach the receiver.

Studying diffraction with the GTD yields the conclusion that -100 dB suppression is not possible due to diffraction over an edge of realistic proportions. A scheme was designed by the BICEP team in which -100 dB was achieved solely by diffraction. [88] [87] This design is based on the criteria that every ray from the ground must diffract two times before hitting the receiver; diffuse reflections are ignored in this scheme. In order to achieve double diffraction, two shields were used: an inner, comoving shield, and an outer, fixed shield.

The double diffraction criterion applied to the POLARBEAR telescope with a 3 meter primary yields a set of ground shields which are unrealistically large. In addition to construction costs, a large comoving ground screen would be susceptible to vibration due to wind. Fortunately, the -100 dB suppression does not need to come from diffraction alone. The intrinsic beam profile, a cold aperture stop, and a primary mirror guard ring yield low beam power near diffracting elements such as the edge of the primary mirror. The compromise for POLARBEAR-I is to use some baffling around the primary and secondary and add a fixed ground screen in the future if ground pickup is limits sensitivity.

2.1.3 Atmospheric Contamination

Ground-based observations need to take effects of the Earth's atmosphere into account. The following effects are considered:

- thermal radiation by the atmosphere
- absorption lines in the mm wave region by water vapor
- potential polarized emission by the atmosphere

These effects are mitigated by choice of observation frequency, use of dual polarized pixels, and choice of observation site. Should the atmosphere become a limiting factor in observations, a satellite mission would avoid this foreground.

Observation Site

POLARBEAR will observe at the Chajnantor Plateau in the Atacama desert. This site was selected for its thin, cold, and dry atmosphere.

The atmosphere emits thermal radiation at a temperature greater than the CMB, and the atmospheric temperature decreases with the altitude of the observatory. As mentioned in the detector sensitivity discussion, the photon noise from the atmosphere emission limits the noise in ground based experiments. Lower sky temperatures are

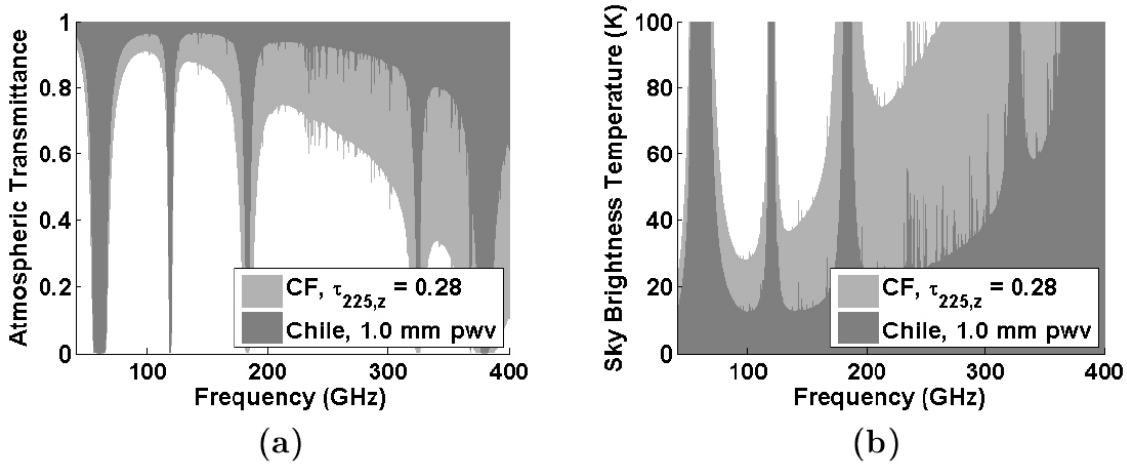

Figure 2.3: Atmospheric Simulations for the POLARBEAR-I observation sites. (a) Shows the transmittance of the atmosphere. Note the high transmittance around the POLARBEAR-I observation band at 150 GHz. (b) The atmosphere thermally radiates at the sky temperatures shown. The assumed observation angle is 30° from Zenith. Both (a) and (b) are shown for the Cedar Flat engineering run site (light grey), and the Chilean science observation site (dark grey). Courtesy of Kam Arnold [4].

desirable for reduction of noise and also thermal loading on the receiver. (The cryogenic system of POLARBEAR-I and heating of optical elements is discussed in Section 3.2.2.)

Further, the atmosphere has a series of water vapor absorption lines in the millimeter wave region. This absorption was calculated with the AM atmospheric model. [70] At the Chilean observation site, the Chajnantor Plateau, the nominal atmospheric conditions present 1 mm precipitable water vapor. The low water vapor is due to the climate and thin atmosphere of this high-altitude site. [74] The engineering run site at Cedar Flat, California presented a higher level of water vapor.

Figure 2.3 shows the transmittance through the atmosphere and the effective atmospheric temperature at the two observation sites. This figure displays the benefits of observing at the high and dry Chilean site: reduced atmospheric absorption and reduced thermal emission of the atmosphere.

Observation Frequency Choice

As seen in Figure 2.3(a), the atmosphere is opaque at certain frequencies, due to absorption of millimeter waves by water vapor. The series of water vapor absorption lines cause windows of high atmosphere transmittance, with peaks around 90, 150, and 220 GHz in the figure. These frequencies are thus ideal observation bands for ground-based experiments. Fortuitously, the transmittance window at 150 GHz also

corresponds with the peak of the blackbody curve of the CMB. POLARBEAR-I observes at a center frequency of 148 GHz, due to the combination of these effects.

Polarization Differencing

Fortunately for ground-based polarization measurements, the atmosphere emission is thought to be linearly polarized at a negligible level. The small level of polarization is due to Zeeman splitting of oxygen energy levels. Water vapor, which is associated with atmospheric absorption, has filled valence bands and does not contribute to polarized emission. [43] At midlatitudes, the power in circular polarization is up to 5 orders of magnitude higher than linear polarization (10^{-4}K for circular polarization and 10^{-9}K for linear polarization). [33] Thus, unless there is conversion of circular to linearly polarized light in the optical chain, atmospheric polarization is a removable foreground for ground-based observations.

To remove unpolarized atmospheric emission, POLARBEAR-I uses pixels with two detectors each, where the two detectors are sensitive to orthogonal polarizations. The beams from the two detectors are linearly polarized on the sky, and in the ray limit, the beams follow the same path through the optical system. For ideal propagation, the beams coincide perfectly on the sky. Differencing the detectors at each pixel subtracts out the common mode atmospheric signal. More on the dual polarized pixels is contained in 3.3.2. The next section addresses possible deviations from the perfect coincidence of beams on the sky.

If the low level of polarized atmospheric emission proves to be a contaminant, future versions of POLARBEAR will use broadband, multi-chroic detectors to remove this signal, see Section 2.2.3.

2.1.4 Beam Systematic Errors

Differencing bolometers at the pixel level leaves the instrument vulnerable to systematic errors. To understand the mechanism for these errors, it is helpful to think of the optics in the time-reversed sense. Each of the detectors at a pixel are coupled to an antenna which emits a linearly polarized beam. These beams traverse the receiver optics, reflect off of the secondary and primary mirrors, and propagate to the sky. In an ideal case, the beams from the two detectors align perfectly, and subtraction of these two orthogonally polarized beams yields the net polarization of the sky signal at that point.

However, the beams may not align perfectly on the sky due to propagation of the two beams differently through the receiver (for example by fabrication defects, reflections, or birefringence). The possible beam differences are illustrated in Figure 2.4. Differential gain and differential beam width show up as a monopole error at each pixel. Differential pointing shows up as a dipole term, and differential ellipticity shows up as a quadrupole term.

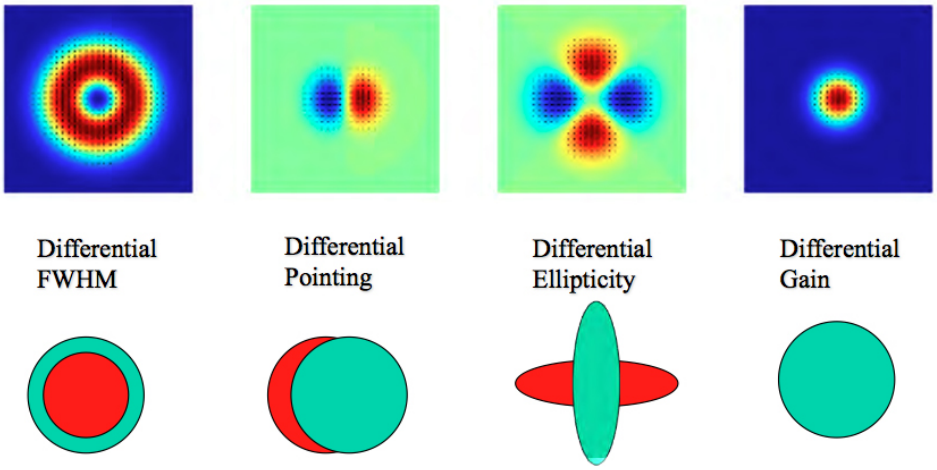

Figure 2.4: Beam systematic error types. Variation in beam properties at the pixel level are shown as a cartoon in the bottom panel, with one polarization in turquoise and one in red. The effect of differencing these beams on an unpolarized sky leads to erroneous monopole, dipole, and quadrupole polarization signals. [83]

All of these systematic errors are preceded by the term *differential* to emphasize that these are mechanisms which effect the two beams from each pixel differently. For example, the main source of beam ellipticity in POLARBEAR-I is reflection off of the primary mirror which generates ellipticity of both beams in the same direction. This is a common mode ellipticity. In contrast, differential ellipticity effects the two beams at cross angles on the sky, so that the subtraction of the two signals yields a quadrupole anisotropy.

A significant part of my thesis work was working to avoid differential ellipticity due to reflections at the surface of the focusing lenslet at each pixel. The focusing lenslet is a high dielectric constant, and reflections off of it are at the 30% level. Fresnel's equations show us that reflections are highly polarized. To make a sensitive polarization measurement, the reflective elements in the optical chain need anti-reflection coatings. Section 4.1.2 goes into detail about the reflection issue at the lenslet surface, and the ellipticity caused by polarization dependent reflections is shown.

2.1.5 Scan Strategy and Polarization Modulation

The scan strategy and polarization modulation by a half-wave plate work together to address systematic errors including: atmosphere subtraction, ground pickup, and instrumental polarization generated inside the receiver.

POLARBEAR-I uses constant elevation scans. Since the observed atmosphere thickness is a function of elevation on the sky, the nominal atmosphere thickness at a given

elevation presents a DC level offset to the scan. This DC level is subtracted out, obviating the need for an atmosphere fitting model.

Sky rotation provides polarization rotation of the sky with respect to the instrument. Thus, scans at a given elevation trace different patches of sky at different times. Signals which show up independent of the observed patch are due to warm ground signal contamination. To remove the ground pickup, a one-dimensional template can be made. Once characterized well, the template can be used to remove ground pick up from any scan. The constant elevation scan simplifies creation of the ground template, since it is a 1-D, instead of 2-D function.

Rotation of polarization with respect to the instrument can also be achieved with a half-wave plate. [20] A continuously rotating half-wave plate (HWP) is considered to be potentially the strongest configuration, as the signal from the HWP rotation can be demodulated from the observed signal. Any polarization signal which does not change with the same rotation frequency has been introduced on the detector side of the HWP (as opposed to the sky side). An unfeasible but illustrative example is a HWP rotating at the sky. Such a device would allow rejection of all instrumentally generated polarization.

POLARBEAR-I has a stepped half-wave plate which can be moved in increments. For practical fabrication reasons, the stepped HWP was more feasible for a field campaign at this time. Future experiments may explore a continuously rotating plate.

2.1.6 Galactic Foregrounds

In addition to the Earth's atmosphere, foreground signal also comes from emission within our own galaxy. Galactic foregrounds are the result of dust, free-free, and synchrotron emission. To minimize these foregrounds, we can observe in regions of low galactic emission. Also, with measurements at multiple frequencies, the unique spectral signatures of these sources can be used for their removal. Removing polarized galactic foregrounds from a primordial B-mode signal could be difficult due to the high intensity of synchrotron and dust sources, both of which are polarized. [14]

Synchrotron and polarized dust emission, discussed separately below, may be correlated on the sky. The production of both signals involves interaction with the galactic magnetic field. [81]

Free-free Emission

Free-free emission is the deceleration radiation (bremsstrahlung) produced by free electrons scattering off of ions. This is produced in plasma regions of the galaxy. Free-free emission is unpolarized at levels of concern to us. For the purposes of polarized foreground removal, it can be ignored. [79]

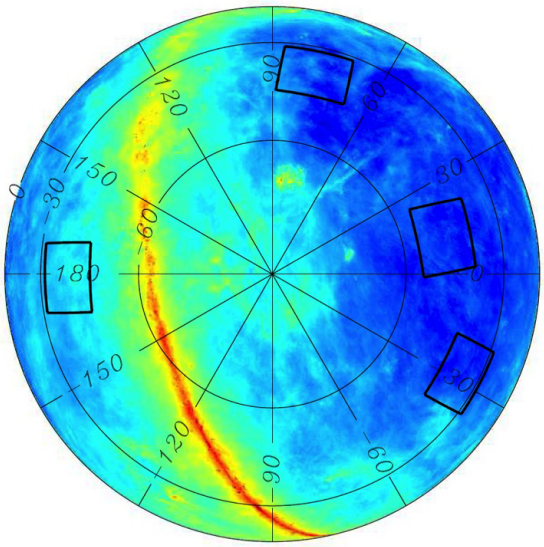

Figure 2.5: POLARBEAR-I scan regions. The four POLARBEAR-I proposed scan regions are shown in black boxes on top of the Schlegel-Finkbeiner-Davis galactic dust map. [82] These regions were chosen for low dust emission and to maximize the amount of time POLARBEAR-I will be able to observe, based on when these regions are above the horizon at the observation site in Chile.

Galactic Dust

The basic physical model for polarized dust emission is blackbody radiation by physically asymmetric, or elongated, dust grains. The grains are aligned by the incident galactic magnetic field to form a net polarization. For example, a single component model following a greybody scaling law would have an amplitude of dust emission

$$A_{\text{dust}}(\nu) \propto \frac{\nu^{\beta_d+1}}{e^{h\nu/kT_d-1}} \tag{2.1}$$

for dust parameters temperature T_d and an index β_d, which is related to the emissivity. [25] Since the CMB temperature is colder than the galactic dust, this dust emission spectrum increases with frequency over the CMB observation range. Dust is the dominant foreground at high frequencies.

Practically speaking, the model may be more complicated than listed above. Multi-component models have been proposed where the emissivity and temperature of different classes of dust grain come into play. For example, for the COBE/FIRAS dataset, the best fit dust model was a two component model. In this model, silicate and carbon-dominated dust grains had different emissivities and temperatures. [28] The dust components can also have unique spatial distribution.

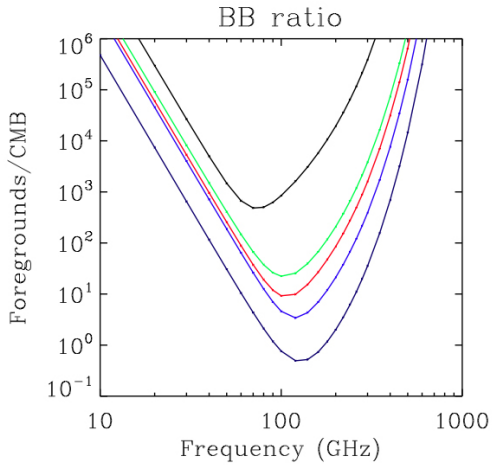

Figure 2.6: Dust Foreground Emission vs. Observation Patch size. Shown here is the ratio of dust foreground to an r = 0.01 B-mode inflationary gravitational wave signal as a function of frequency. As this ratio depends on the area of the sky covered, curves are drawn for 100%, 82%, 50%, 23% of the sky and finally a single 10 x 10 degree patch (with the smaller area selections corresponding to low dust sky regions). The foreground minimum moves to higher frequency with smaller patch size. For the 10 x 10 patch the minimum is below unity, i.e., the inflationary signal is larger than the dust signal. The assumed polarization fraction is 5% corresponding to Planck sky model v.1.6.2. Figure from [24]

To minimize galactic foregrounds, we chose low dust regions to observe in. Figure 2.5 shows these regions on top of a galactic dust map. The intensity shown in the figure is expected to be polarized at approximately 10%.

As expected, the ratio of polarized dust emission to a B-mode signal decreases as we select a smaller, low dust, region of the sky. This is illustrated in Figure 2.6. As shown in the figure, the frequency minimum of this ratio increases as the observation area is limited to cleaner patches of sky, and for small areas of sky, an $r = 0.01$ inflationary B-mode has more power than the dust foreground.

POLARBEAR-I will also take advantage of the frequency dependence of the dust foreground by using the Planck sky map for foreground removal. Planck HFI has channels at 217 and 353 GHz, enabling subtraction of a two parameter dust model. Planck beams are well matched to POLARBEAR-I , $5'$ and $4'$ respectively, so that the map resolution will be similar. Assuming the Planck Blue Book specifications [89] with updated sensitivity [72], a spectral index $\beta_d = 1.6$, a dust subtracted limit of $r = 0.04$ is expected. The official Planck data release slated for January 2013 will be precede the end of the POLARBEAR-I field campaign in 2015.

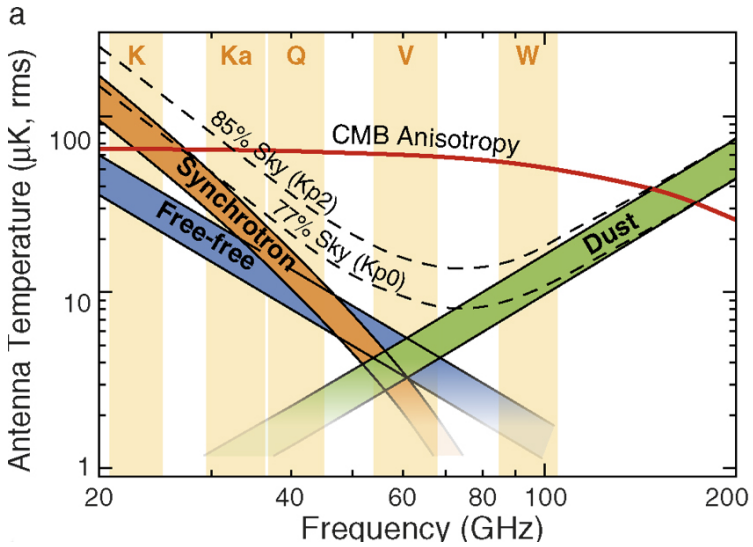

Figure 2.7: CMB foregrounds. The power in the foreground anisotropy is a minimum at just less than the peak of the CMB intensity, which occurs at 150 GHz.From [12]

Synchrotron

The motion of ultra-relativistic ions in the galactic magnetic field causes a synchrotron radiation. Cosmic rays and electrons from supernovae remnants are the main contributors to this foreground. The synchrotron spectrum follows a power law: [43]

$$T_{\text{synchrotron}}(\nu) = \nu^{\beta_s} \tag{2.2}$$

where β_s is the synchrotron spectral index. The value is taken to be $\beta_s = -3$ in POLARBEAR-I regions of interest. [25] WMAP showed that the index β_s varies from -3 in the galactic halo to -2.5 in star forming regions. [12]

Conveniently, synchrotron radiation decreases with frequency, so there is a foreground minimum around the peak of the CMB spectrum. Figure 2.7 shows this minimum in intensity anisotropy. For the purposes of polarized foreground measurements, these intensities must be multiplied by a polarization fraction (thus reducing the importance of free-free component).

The POLARBEAR-I sky patches were selected to have overlap with QUIET in two patches. The QUIET measurement at 40 and 90 GHz will be able to set a 95% upper limit on synchrotron polarization anisotropy which is equivalent to $r = 0.01$ to $r = 0.02$ (depending on the sky region). With this limit, the desired POLARBEAR-I sensitivity limit $r = 0.025$ will be achievable.

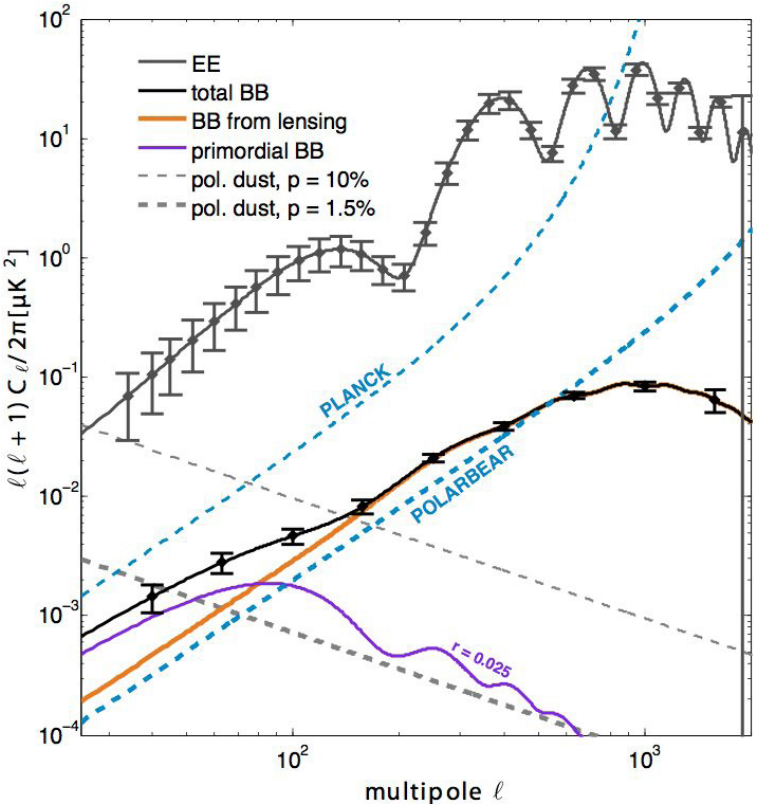

Figure 2.8: POLARBEAR-I expected sensitivity. With the design considerations presented here, POLARBEAR-I expects to be sensitive to primordial B-modes as low as $r = 0.025$ to 95% confidence (purple curve). A detection of lensed B-modes at 14σ is expected (gold curve). POLARBEAR-I is an order of magnitude more sensitive than the Planck satellite. [45]

2.1.7 POLARBEAR-I Sensitivity

Studies of the dust and synchrotron indicate that these astronomical foregrounds will not limit the detection of low r B-modes, as long as we use sufficiently precise frequency scaling models for foreground subtraction. [25] The combination of patch selection, Planck HFI, and QUIET data will be sufficient to detect inflationary B-modes to $r = 0.025$ to 95% confidence. This assumes a two year observation period at the Chajnantor Plateau. The projected POLARBEAR-I power spectra are shown in Figure 2.8.

The projected sensitivity changes with angular separation, or l value, on the sky. POLARBEAR-I was designed to measure a wide l range to measure both primordial and lensed B-modes. The pixel beam size, $4'$, limits the resolution for small features on the sky (high l). The observation patch size, 15°, limits the sensitivity to large features (low l)

As shown in Figure 2.8, the foreground power decreases at small angular scales (high l) so that the lensing B-mode signal will be detected above the foregrounds. In the Figure, polarized dust emission is shown at two levels, 1.5% and a conservative 10%. With the projected sensitivity, a 14σ lensed B-mode detection is predicted. This lensing signal would constrain the sum of neutrino masses to 75 meV with 68% confidence. [45] [85]

2.2 Broadband Measurements

Broadband, or multichroic, pixels are being developed at UC Berkeley to receive information from multiple frequency bands at once. This is in contrast to experiments that have pixels recording different frequencies, or even a split optical path with multiple receivers each measuring a unique frequency band. In the scheme being developed at Berkeley, the frequency bands are distinguished from each other by a series of resonant filters, and each frequency band is read out by a unique detector. Technology development for future broadband measurements is discussed in Chapter 6. New technology includes broadband millimeter wave antennas, readout for multiple channels, and broadband anti-reflection coatings.

The benefits of multichroic pixels include increased signal for a fixed focal plane area, better atmosphere removal, and frequency dependent foreground modeling and subtraction.

2.2.1 Systematic Error Reduction: Anti-Reflection Coatings

The types of possible systematic errors for a broadband system are generally same as for a single frequency system, discussed earlier in this chapter. We have previously discussed polarized reflections and the possible introduction of a differential ellipticity. These effects are minimized in a single frequency experiment via quarter-wavelength anti-reflection coatings on the refractive optical elements. Quarter-wavelength coatings are discussed in Section 4.1.2.

The quarter-wavelength coatings rely on a tuning of the thickness with respect to the wavelength, and this tuning cannot hold over a large bandwidth. Thus, new anti-reflection coating technologies are necessary to avoid systematic errors and harness the benefits of a broadband system. Development of this technology was a large part of the author's thesis work, and this topic is discussed in Chapter 6.

2.2.2 Signal and Mapping Speed

A broadband pixel collects more of the available CMB radiation, and due to this signal gain is expected to have a higher sensitivity. Intuitively, one may expect that the mapping speed provided by multichroic pixels would be simply the single

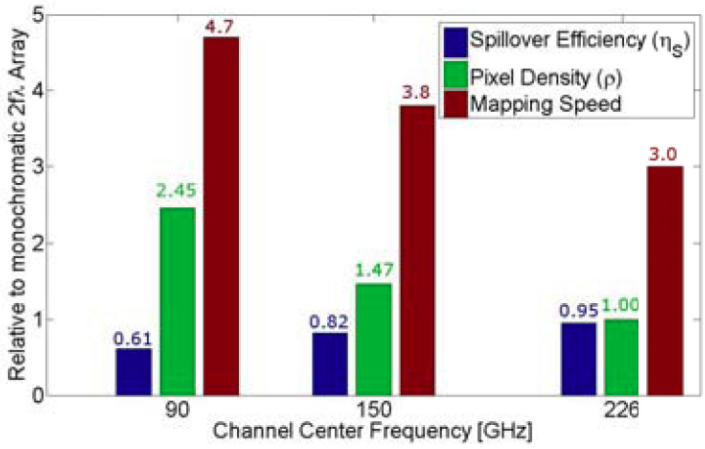

Figure 2.9: Mapping speed of triplexed pixels. Here the mapping speed, spillover efficiency, and pixel density are shown for pixels with three observation bands. The mapping speed is roughly 3 times the nominal speed of a single color detector at $2F\lambda$ spacing. Figure and calculation from Roger O'Brient's thesis. [69]

frequency mapping speed multiplied by the number of bands, i.e. for a pixel with N frequency bands, the mapping speed is a factor of N faster. There are some nuances, but this is approximately true. [69]

The details of the mapping speed involve the fact that the pixel spacing changes relative to a wavelength for the different band wavelengths. The nominal spacing used, $2F\lambda$, optimally samples the airy function caused by diffraction at the limiting aperture of the system, i.e. the main lobe of the airy function, before it goes negative, is perfectly filled by a pixel. Finer pixel spacing at $< 2F\lambda$ samples the airy function with finer spatial resolution. However, for these smaller pixels, the pixel beam is wider and more of the optical power hits the cold aperture stop. The fraction of beam power (in the time reverse sense) which hits the cold aperture increases photon noise (typically at a temperature $T_{stop} > T_{CMB}$) without adding to the amount of detected CMB signal. The sensitivity gain of smaller pixels is balanced by the photon noise trade-off. Optimal mapping speeds are usually found for pixels spaced at $1F\lambda$ to $2F\lambda$. The $2F\lambda$ is the optimal spacing for a fixed number of pixels (a readout limited system), and smaller pixel spacing is ideal for systems with a fixed focal plane area but unlimited pixel count. [30] [32]

Thus, for a broadband ground-based experiment such as POLARBEAR-II , the pixel spacing is chosen to be $2F\lambda$ for the highest frequency band. With this pixel size and spacing fixed, the longer wavelength bands thus have spacing $< 2F\lambda$ at their respective wavelengths. The low frequency bands have wider beams and thus more power on the cold aperture stop. The loss in power at this stop is compensated by the comparatively denser sampling at these frequencies. The net mapping speed gain

roughly scales as the number of channels. Detailed projections, as calculated in [69], are shown in Figure 2.9.

2.2.3 Atmosphere Removal

As previously discussed, differencing at the pixel level will remove unpolarized atmospheric emission. However, in the event that low level polarization is a limiting factor, ground-based experiments can use the thermal spectrum of the atmosphere (at about 20 Kelvin) to separate this signal from CMB and other foregrounds. Since the atmospheric fluctuations are expected to be on relatively large scale, following a Kolmogorov spectrum, it is possible to have observation pixels and separate pixels at a higher frequency for monitoring the atmosphere. The benefit of multichroic pixels is that the bands from each pixel are recording the same patch of atmosphere at the same time.

Removal of atmospheric emission by its thermal spectrum has previously been demonstrated in CMB intensity measurements. SuZIE-II, for example, observed with a small number of multichroic pixels at 145 GHz, 221 GHz, and 355 GHz, where the spectral information was used for removal of the atmosphere. [13]

2.2.4 Foreground Subtraction

As previously discussed, the contributors to polarized galactic foregrounds, dust and synchrotron emission, have unique spectral dependence. This dependance can be used to characterize and remove the foregrounds. POLARBEAR-I one plans to use Planck and QUIET data for foreground removal (dust) and limits (synchrotron) respectively. Fortunately, the beam resolution and sky overlap of these experiments are a close enough match to yield an $r = 0.025$ sensitivity for POLARBEAR-I .

To detect lower r signals, it will be advantageous to use the same beam size (or smaller) and completely overlapping sky patches for foreground removal. These goals would be accomplished by multichroic pixels, where the beam narrows with increasing frequency. [27] Smaller beams at higher frequencies would measure the dust foreground with high resolution.

2.2.5 Instruments in Development: POLARBEAR-II and Satellite Missions

Development of the POLARBEAR-I antenna coupled detector technology for broadband experiments is underway, see Chapter 6. POLARBEAR-II is a planned extension of POLARBEAR-I . It will use the same telescope design as POLARBEAR-I , as well as the systematic error controls already described for single frequency instruments. Each pixel will use a broadband sinuous antenna and two channels will be separated in readout: 150 and 220 GHz. In addition to the signal gains from the second

band, the 220 GHz channel will be used to remove polarized galactic dust emission. POLARBEAR-II is projected to detect a gravitational wave B-mode signal as low as $r = 0.01$.

It may be necessary to have more than two frequency bands for foreground removal, depending on the value of r and the complexity of the polarized foreground signal (such as multi-component dust models). A broadband sinuous antenna has been developed at UC Berkeley. This antenna is compatible with readout of seven frequency bands from 60-250 GHz. The frequency placement of these bands is dictated by a log-periodic scaling, and would be suited to a satellite mission where band placement is not dependent on the location of atmosphere absorption lines. [67]

The use broadband pixels is a change in technology and will allow low r detections. The technology in development at UC Berkeley is directly applicable to space missions, in particular due to the efficient use of the focal plane. Satellite missions under discussion include NASA's CMBPOL [8] [93] and Japan's LiteBIRD [35] [34].

Chapter 3

POLARBEAR-I Instrument Design

B-mode experiments require high sensitivity and low instrumental systematic error, so POLARBEAR-I was designed with these goals in mind. The optical design properties include diffraction-limited beams, low sidelobes, low cross-pol, and a large flat focal plane. The optics of the POLARBEAR-I experiment include the telescope, reimaging optics inside the receiver, and optics on the focal plane which focus radiation onto the antennas. These elements work in conjunction to meet the design criteria of the optical system. For high sensitivity, the detectors should be photon-noise limited, i.e. limited by statistics of the incoming signal, as opposed to readout noise limited. The detectors are Transition-Edge Sensor (TES) bolometers, which operate at their superconducting transition. Thus, the detectors are kept at sub-Kelvin temperatures in the receiver. Finally, overall sensitivity is improved by using multiple detectors. POLARBEAR-I has 1,274 optically active bolometers whose signal needs to be read out. The optical design, detectors, cryogenic receiver, and readout are described in this chapter.

3.1 Telescope Optics

3.1.1 Telescope Basics

Telescopes gather electromagnetic radiation and focus it to an image plane where it is viewed or recorded. In a single moded system, the beam size goes as the inverse of the primary mirror collecting area. The typical beam sizes used for CMB measurement correspond to large primary mirrors, on the scale of meters. Due to the aperture sizes, CMB measurements are almost always more suited to reflecting rather than refracting telescopes.

Reflecting telescopes are often made of conic sections. For a true conic, rays leaving one focal point will converge at the other focal point. This principle can be used to chain optical elements together by aligning their foci. For example, a parabola is commonly used as the first, or primary, mirror; it has two foci: one at

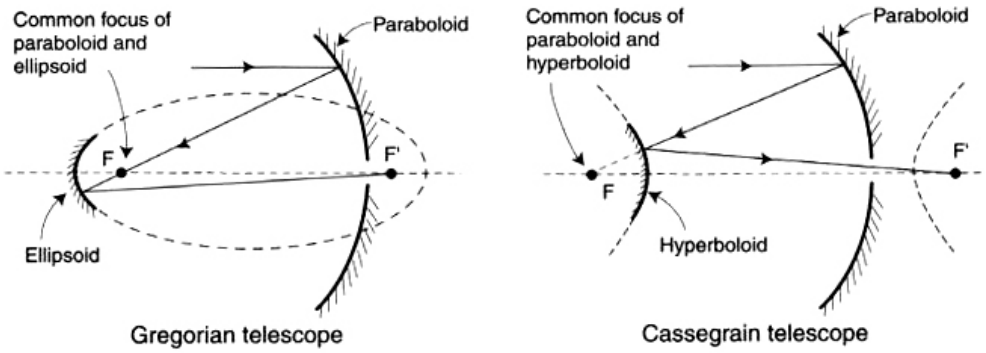

Figure 3.1: On-axis Gregorian and Cassegrain telescope designs. Figure from [10].

infinity (where the astronomical object is) and a closer one on the parabola axis of symmetry. Light from a distant source is formed into an image at the close focal point of the parabolic reflector. The image may be observed at this focus, or the parabola focus can coincide with a focus of another conic section, thus forming a two mirror telescope (see Figure 3.1). By aligning foci, conic sections can be chained to form a multi-mirror system. The reflecting optical elements are referred to, in order of appearance in the optical chain from the sky side, as the primary, secondary, tertiary, and so on. Multiple mirror systems are used to control and correct imperfections in the image including spherical aberration, coma, astigmatism, field curvature, distortion, and, in the case of refracting optics, chromatic aberration. In general, the number of image aberrations that can be corrected is equal to the number of optical elements in the system. [10]

3.1.2 The Huan Tran Telescope

The Huan Tran Telescope (HTT) is a dedicated instrument and was custom designed by its namesake for the POLARBEAR-I experiment. [3] HTT, shown in Figure 3.2, is an off-axis Gregorian Dragone, a design which is used by many of the contemporary CMB polarization experiments, e.g. see Table 3.1 for a list of CMB experiments organized by telescope type. As further described below, the branch points in the design decision for a two mirror telescope were on-axis vs. off-axis, Gregorian vs. Cassegrain, standard vs. crossed Gregorian (the latter dichotomy applicable only to off-axis designs). For polarization properties, the Mizuguchi-Dragone condition was employed. Baffling and a ground screen may be employed in addition to the refracting design for further sidelobe suppression.

Sidelobes are the major concern in the choice between on-axis and off-axis designs. On-axis telescopes have large sidelobes due to the secondary mirror occluding the main beam. Diffraction occurs at the edges of both the secondary and the secondary support structure, changing the spatial distribution of the beam to include

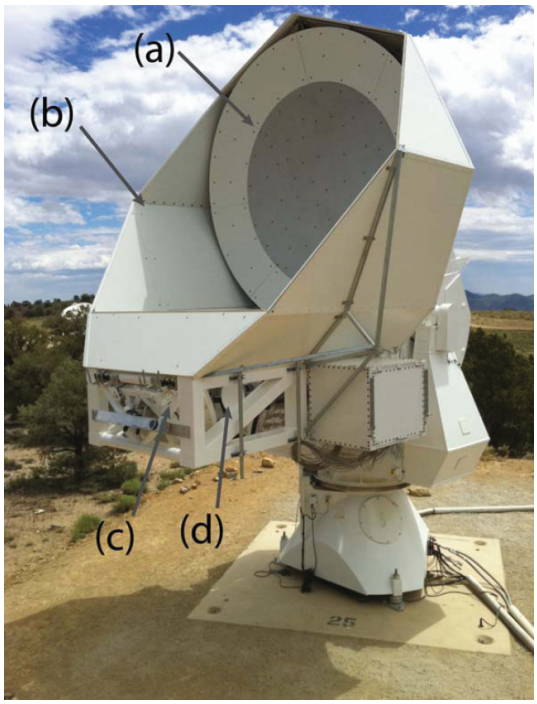

Figure 3.2: The Huan Tran Telescope with the POLARBEAR-I receiver. The monolithic 2.5 m primary mirror is surrounded by a paneled guard ring to prevent spillover (a). The inner ground shield (b) reduces sidelobes. The secondary reflector (c) re-images the primary focus inside the cryogenic receiver (d) which houses re-imaging lenses and the detector focal plane.

Table 3.1: Telescope designs for CMB polarization experiments

Telescope Style	**Experiment**
On-axis Cassegrain	QUEST COMPASS POLATRON
Off-axis Cassegrain	CAPMAP
Cross-Dragone	POLAR QUIET CLOVER
Off-axis Gregorian Dragone	PLANCK-LFI and -HFI POLARBEAR SPT-POL EBEX
Refracting optics in receiver	BICEP

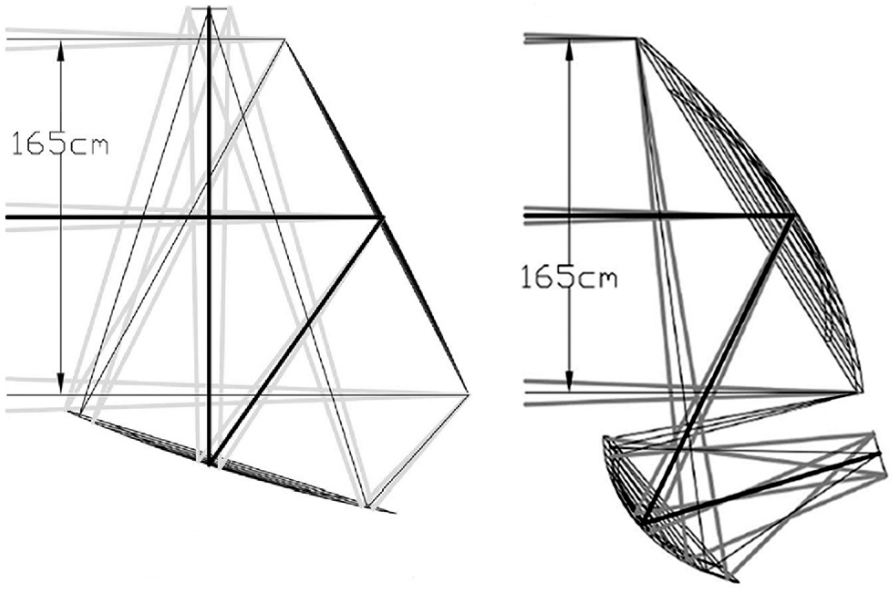

Figure 3.3: The crossed Gregorian and Gregorian geometries, from [90].

wider angles. These sidelobes can hit undesired parts of the sky or, worse, the ground. Ground pickup is a significant issue due to the relative temperature of the ground compared to the cold CMB; in extreme cases it could cause excess loading on the cryostat and detectors, and it commonly creates a scan synchronous signal (which is difficult to remove). Although the difficulty of diffracted sidelobes is present, experiments including QUEST, COMPASS, POLATRON, and CAPMAP have all used two mirror on-axis Cassegrain designs.

The choice of a Gregorian vs. Cassegrain system was also made to improve sidelobe properties. In a two mirror system, the parabolic primary focus coincides with the focus of another conic, i.e. a hyperbola (Cassegrain design) or an ellipse (Gregorian design), see Figure 3.1. In the Gregorian design, the secondary foci are real, causing the beams to converge at that focus. The constriction of the beams in the Gregorian design allows more aggressive baffling between the primary and secondary than the Cassegrain design (with its imaginary foci) would allow. Though not present in the POLARBEAR-I engineering run, baffling around this focal point is planned for use in the Chilean science deployment to reduce sidelobes.

Another configuration for a two mirror off axis telescope is the crossed, or side-fed, design as shown in figure 3.3. A comparison [90] of the Gregorian and crossed designs shows that for equivalent primary aperture area and optimal mirror positioning, i.e. the Mizuguchi-Dragone condition, the crossed design has a larger diffraction limited field of view and approximately 10dB better cross polarization. However, both designs

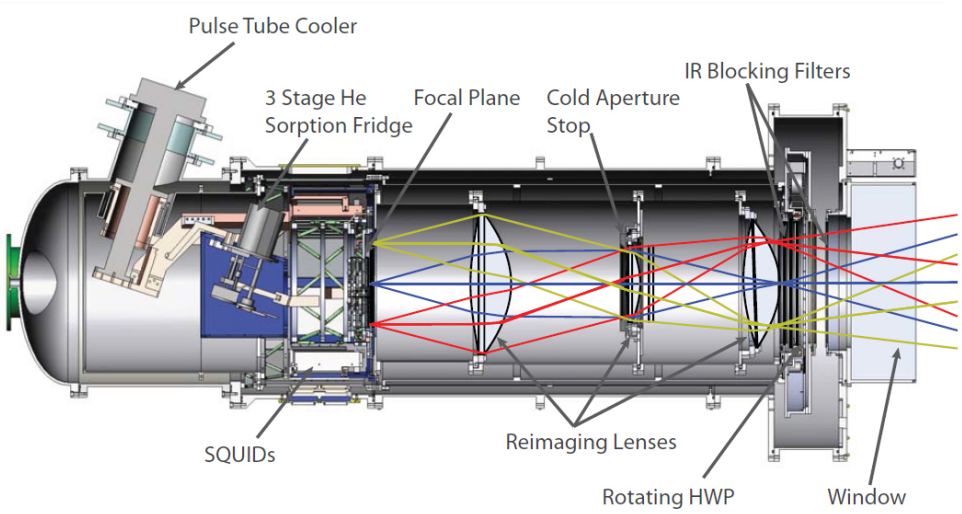

Figure 3.4: The POLARBEAR-I receiver in cross section.

have good cross-polarization levels and equivalent instrumental polarization. The larger focal planes allowed by the crossed design come at the cost of having a secondary mirror nearly as big as the primary. For a 3.5 m primary mirror such as that on HTT, the size, weight, and cost of the Gregorian design is much more feasible.

For any choice of telescope designs, the Mizuguchi-Dragone condition is applied to minimize cross polarization. Simply stated, this condition selects the angle between the primary and secondary axes of revolution so that there is zero cross-polarization at the center of the focal plane. This condition minimizes the net cross-pol over the focal plane. [64] [23]

3.2 The POLARBEAR-I Receiver

The POLARBEAR-I receiver was designed to have the appropriate re-imaging optics and to provide the detectors with the low temperature environment necessary.

3.2.1 Receiver Optics

In addition to the telescope optics, the receiver holds three cryogenic re-imaging lenses. Thus, there are in total five optical elements which, as mentioned earlier, is the number needed to correct for the five types of achromatic aberrations. In particular, a unique aspect of POLARBEAR is its planar, lithographed focal plane. Lithography of detectors on flat wafers is motivated by its ease of scalability to larger focal planes. However, re-imaging optics are necessary to achieve a flat, telecentric focal plane and couple to the detector arrays. These re-imaging optics are shown in Figure 3.4. [3]

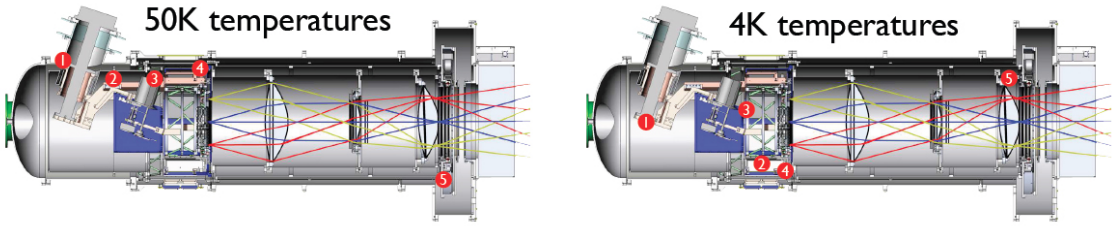

Figure 3.5: The POLARBEAR-I receiver in cross section temperatures. 50K stages (left) include: (1) 50K fridge coldhead, (2) 50K tower strap cold, (3) 50K tower strap warm, (4) 50K wire harness, (5) Half-wave-plate baseplate. 4K stages (right) include: (1) 4K coldhead, (2) SQUID card, (3) 4K mainplate, (4) Midsection, (5) Lens flange

The re-imaging optics also provide the important function of creating an aperture plane within the cryostat. This allows a cold Lyot stop in the system, which is blackened and absorbs hot, stray radiation caused by diffraction and thermal emission of warm elements in the instrument. The Lyot is sized to illuminate the high precision surface of the primary mirror. The combination of the cold Lyot, the primary guard ring, and telescope shielding results in low sidelobes. [59]

3.2.2 Receiver Cryogenic Design

Ground-based CMB experiments are automatically limited by thermal signal from the Earth's atmosphere. To be as sensitive as possible, all sources of noise should be subdominant to the photon noise introduced by the comparatively hot atmosphere. In addition to the atmosphere, other sources of noise include thermal carrier noise in the detectors and photon noise from warm elements inside the receiver. Thus the focal plane, re-imaging optics, and interior of the receiver are kept cold. Additionally, signal out of the observation band may be filtered out to reduce loading on the detectors. Graduate student Zigmund Kermish worked extensively on the structural and cryogenic design of the POLARBEAR-I cryostat, and details of this work are described in his thesis. [46]

Refrigeration Mechanisms

With a focal plane below 0.25 Kelvin, thermal noise in the detectors is subdominant to the photon noise of the atmosphere at the Chilean observation site. Cooling to sub-Kelvin temperatures from the 300K ambient is typically accomplished at multiple stages using different cryogens or cooling systems. In the POLARBEAR-I cryostat, we use a pulse tube refrigerator for 50K and 4K stages and a Helium sorption fridge to supply the 0.25K stage. Both systems are closed cycle, so cryogens do not need to be replenished.

The pulse tube cooler employed by POLARBEAR , a Cryomech PT415 [1], provides cooling power by compressing Helium gas and using its expansion to remove heat from the coldhead. The compression stage occurs at room temperature, thus there are no cold moving parts. The 50K and 4K thermal stages supplied by the PT415 are diagrammed in Figure 3.5.

To get to sub-Kelvin temperatures, POLARBEAR-I utilizes a Simon Chase Research ^{4}He-^{3}He-^{3}He evaporation cooler [2]. This cooler is daisy chained off of the pulse tube cooler as it relies on a 4 K (or colder) mainplate. During the refrigeration cycle, liquid helium is condensed on carbon getters. This condensation acts as a pump lowering the temperature on the intermediate-cold head (IC) and the ultra-cold head (UC). [15]

In the POLARBEAR-I observation cryostat, the IC head reaches 350 mK. The IC head sinks an intermediate cold stage responsible for thermal loading of wiring and structural elements. The focal plane is linked directly to the UC head which reaches 250 mK. Care was taken with the thermal loads so that the UC stage would stay cold for periods of $>$ 20 hours between cycles.

Reduction of Thermal Load

The pulse tube has limited cooling power, i.e. there is only so much energy they can absorb while keeping the stages at the design temperatures. Most importantly, the 4K stage must be cold enough to cycle the Simon-Chase fridge which supplies the focal plane with mK temperature. The stage temperature dependance on thermal load is shown by the POLARBEAR-I pulse tube load curve, Figure 3.6. The following were addressed to reduce thermal load:

- thermal conduction of structural elements supporting the cold stage
- thermal emission inside the cryostat
- thermal conduction due to electrical readout
- thermal energy of out of band radiation in the optical chain.

Structural elements in the receiver provide a thermal path from the 250 mK Ultrahead to the 300K ambient surroundings. To reduce this, low conductivity supports were used, such as G10 fiberglass rods.

Radiation by warm elements in the cryostat can be absorbed by the focal plane. Radiative loading inside the cryostat was reduced by nesting a cylindrical 50K radiation shield inside the cryostat. Radiative transfer between the 300K and 50K shells was reduced with multilayer insulation (MLI). MLI has conductive layers separated

[1] http://www.cryomech.com

[2] http://www.chasecryogenics.com

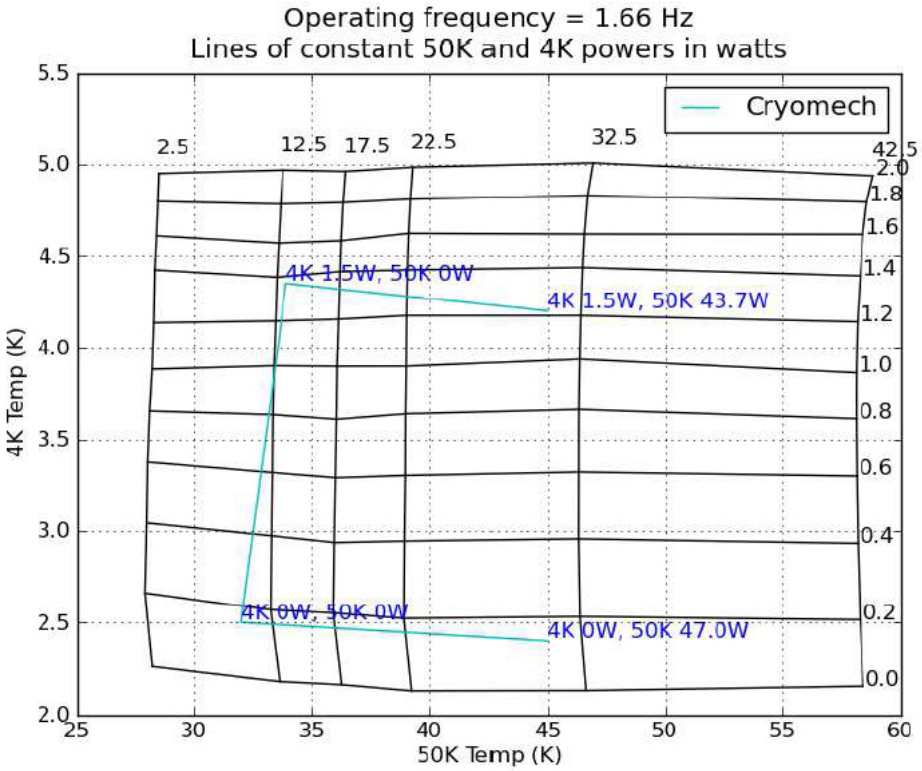

Figure 3.6: The POLARBEAR-I PT415 pulse tube load curve. Note the curve provided by Cryomech at the factory default operating frequency (1.4Hz) is shown along with the measured load curve at 1.66Hz, where POLARBEAR-I operates for increased efficiency. [46]

by a small distance with bridal veil or similar non-conductive, vacuum susceptible material.

Another thermal load is presented by wires carrying signal in and out of the cryostat. This problem increases with the number of detectors in an experiment. The Wiedemann-Franz law describes the electronic contribution to thermal conduction; thus electrical and thermal conductivity are related. [5] Heat sinks are used along the readout path to minimize this. In particular, highly conductive copper was needed to make a direct, high efficiency heat strap between the SQUID readout and the 4K Simon Chase condensation stage. These elements can be seen in right hand panel of Figure 3.5 where the Squid card is element (2) and the 4K coldhead is element (1). High conductivity was achieved by annealing the copper at $\sim 900\ ^{\circ}\mathrm{C}$, reducing lattice defects and improving electrical and thermal conductivity.

Improvements in the conductivity are measured by the residual-resistivity ratio, RRR, defined as the ratio of room temperature resistivity to the resistivity at zero

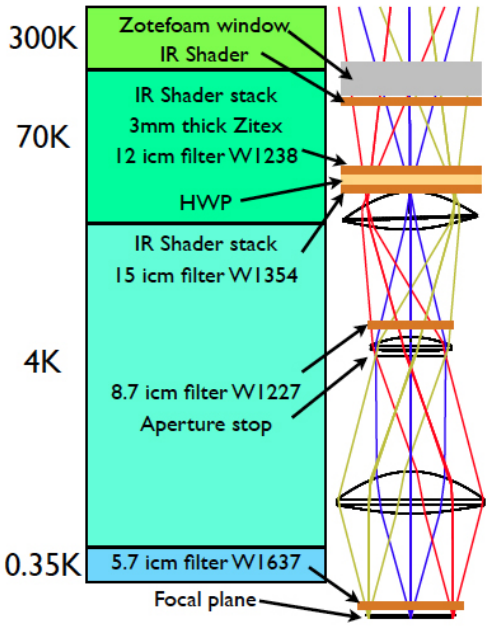

Figure 3.7: The POLARBEAR-I Optical Stack. The temperature changes vertically along the optical stack are shown along with location of optical filters. [46]

temperature:

$$RRR = \frac{\rho_{300K}}{\rho_{0K}} \tag{3.1}$$

For this annealing process, the RRR was ~ 300 vs. RRR ~ 100 for un-annealed bulk OFHC copper.

On the final parts, the annealing was done commercially, but prototypes of the process were done by the author and other students in a vacuum oven with a small Nitrogen leak following the procedure described in Reference [77]. The vacuum oven was set to 10^{-5} Torr base pressure, then when the oven reached a ~ 700 °C, dry air leak to 10^{-4} Torr was introduced. We used thick wires for the prototypes as opposed to bulk copper, and we achieved high RRR values, up to 1000. Lower bounds on the RRR values were measured by taking the ratio of the total resistance of a sample at 300K and 4K. This was accomplished with a 4 point measurement of a sample dunked in liquid helium.

Finally, out of band radiation adds undesirable thermal energy. Radiation that is not filtered out can be seen at the focal plane, and radiation that is filtered out can still warm components in the optical chain, which emit thermal radiation of their own. Thus, multiple stages of optical filtering were supplied by large aperture metal mesh filters and absorbers, see Figure 3.7. As is common in this field, low and high pass optical filters were made by Peter Ade's group at Cardiff [1]. The filters are

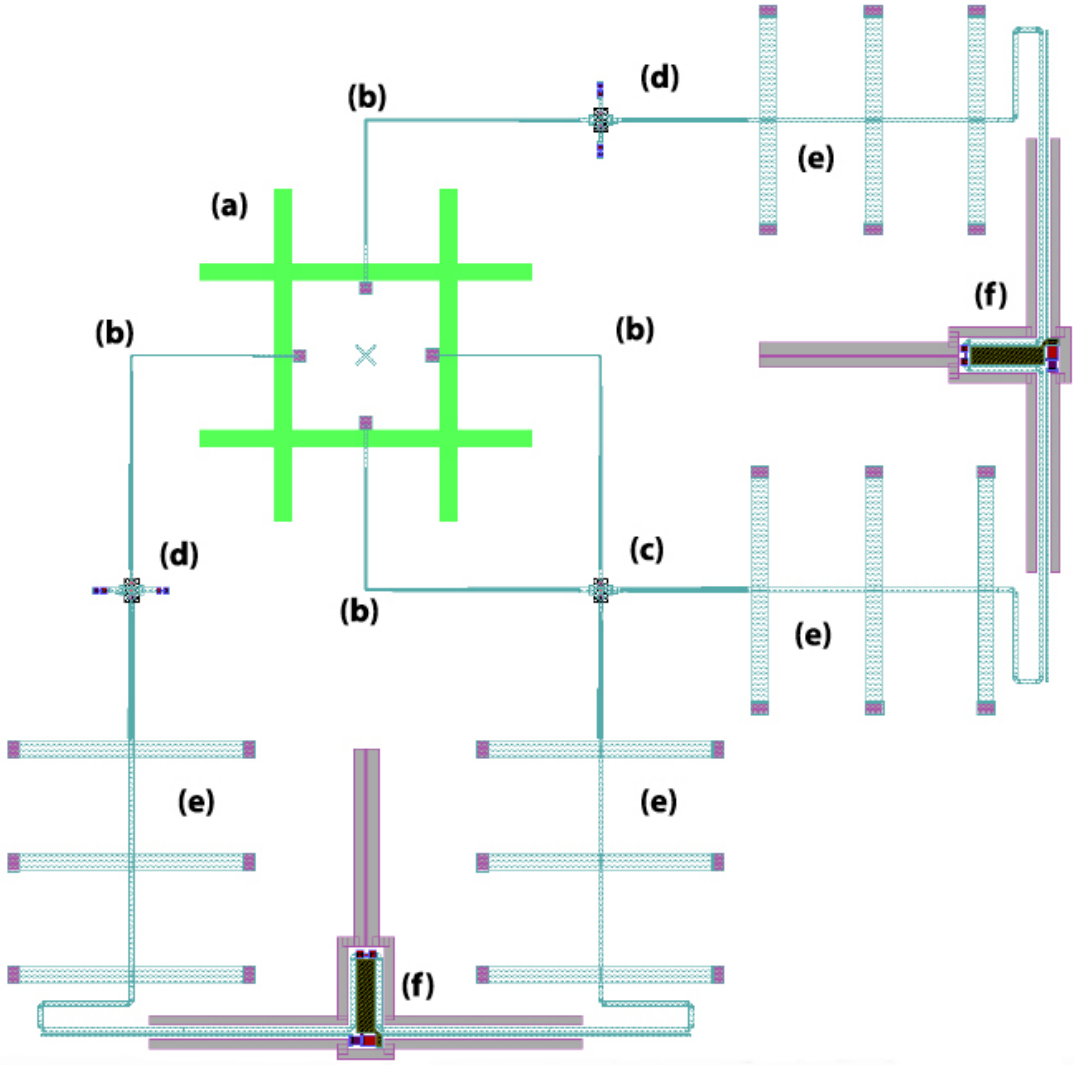

Figure 3.8: The POLARBEAR-I Pixel. The structures are labelled in the order that the CMB photon energy travels through them: (a) Crossed double-slot dipole, (b) Dolph-Chebychev microstrip transformer (c) microstrip cross-under, (d) cross-under balancing structures, (e) microstrip filters, and (f) bolometers. Courtesy Kam Arnold.

composed of polypropylene hot pressed together with layers of deposited metal. The geometry of the metal layer deposition is selected to reject out of band radiation.

3.3 Antenna Coupled TES Detector Arrays

POLARBEAR-I is pioneering a new radiation coupling mechanism: antenna coupled TES bolometers. In this scheme, the horn array which has historically been

used to focus radiation onto the detectors is replaced by an antenna. The antenna is lithographed onto the same substrate as the detectors, so this design is naturally scalable. Additionally, a broadband antenna can be used, yielding multichroic pixels. A broadband antenna will be used in future versions of POLARBEAR , but POLARBEAR-I is a single frequency instrument.

The whole pixel, including the antenna and bolometer detectors is shown in Figure 3.8. This diagram lists, in order, the elements that the optical power travels through. The double slot antenna, 3.8 (a), receives two polarizations, each of which are read out by a TES bolometer detector (f). Between the antenna and detectors, the current generated in the antenna travels on microstrip lines, (b). These lines have a tapered profile for impedance matching to the antenna. The spectral response of the antenna is further limited by on-chip band defining filters (e). Note that the balanced feed lines from the two antennas cross at feature (c). In order to isolate these electrical signals, a cross-under feature is used with a dielectric layer between the conducting microstrips. To ensure the antenna receives a balanced load, an identical cross under is placed at (d).

3.3.1 TES Bolometer Detectors

Most CMB measurements to date have used bolometers. Bolometers absorb incident radiation and have an electrical resistance which changes with temperature, so the amount of absorbed radiation can be measured by the resistance of the detector. Bolometers may thus have two parts which are in thermal contact with each other: an absorber which captures incident radiation and a thermistor whose electrical resistance changes with temperature. Figure 3.9 shows a generic bolometer schematic.

The sensitivity of the bolometer depends on how quickly the resistance changes with temperature. A very sensitive bolometer has a large change in resistance for a small change in temperature. For example, the charge carriers of a Neutron Transmutation Doped (NTD) bolometer are frozen out as the temperature decreases. An increase in optical power (warming the detectors) thus translates to a decreased electrical resistance. NTD-Germanium bolometers (NTD-Ge) were used in CMB observations such as ACBAR, MAXIMA, and BOOMERanG.

Transition-Edge Sensor (TES) bolometers exploit the rapid change in resistance at the superconducting transition of a metal. The extreme dependence of resistance on temperature through this transition gives the TES its high sensitivity. The slope of the temperature dependence of any bolometer is characterized by

$$\alpha \equiv \frac{d(logR)}{d(logT)} = \frac{T}{R}\frac{dR}{dT} \tag{3.2}$$

a dimensionless parameter. [75] TES bolometers have a positive value of $50 \leq \alpha \leq 500$, whereas NTD-Ge bolometers have $\alpha \sim 1$.

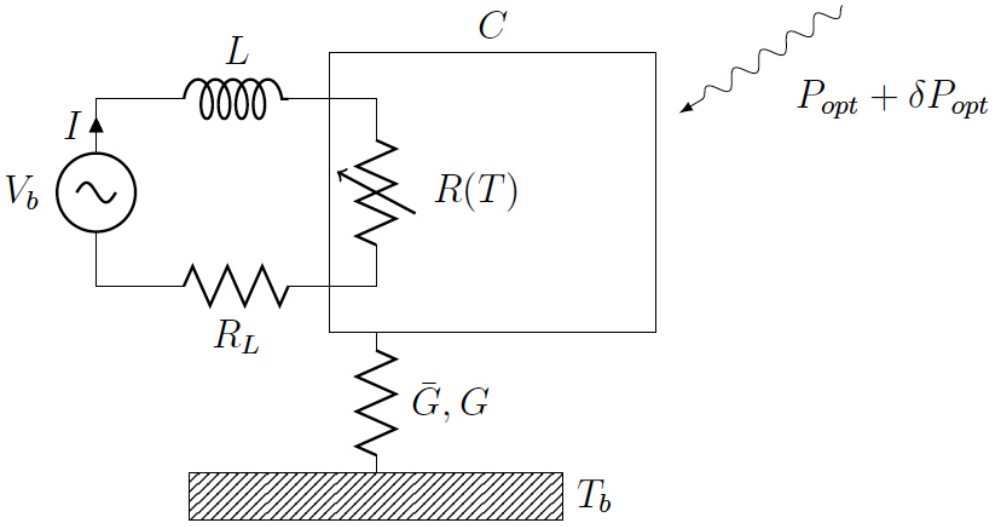

Figure 3.9: Bolometer schematic. The thermistor is represented by R(T) and the absorber heat capacity is labeled C. The thermistor/absorber is heat linked to a thermal bath T_b. The thermistor is voltage biased, V_b, and optical power P_{opt} represents incident radiation.

One may worry that the superconducting transition will be an unstable place to operate detectors. The temperature of the TES is influenced by:

- optical power incident on the absorber
- the thermal link (often called "G") of the bolometer to its heat bath
- the electrical power bias being run through the thermistor

The detector will stay in its transition if the sum of these powers remains constant. Luckily, electrothermal feedback allows the TES to remain in its transition. [58] To visualize this, imagine applying a constant voltage bias so the detector is the middle of the superconducting transition. Then, add optical power. This increases the temperature of the thermistor. Due to the large, positive response α, the thermistor resistance increases. The electrical bias power,

$$P_{bias} = \frac{V^2}{R(T)} \tag{3.3}$$

drops due to the increase in resistance. Thus, the increase in optical power naturally reduces the electrical bias power (and vice versa), allowing the bias point to be stable. The electrical bias point does effect the time response, or time constant

τ of the bolometer. For signals varying slower than the time constant (at frequency $\omega << 1/\tau$) at the proper bias point on the IV curve, the detector experiences strong-electrothermal feedback and the detector response is linear over a wide range of incident optical signals. [69]

The POLARBEAR-I TES bolometer contains the elements shown in the bolometer schematic. The TES is lithographed on a silicon wafer substrate, as shown in Figure 3.10. The substrate is etched away under suspended islands which contain the absorber and thermistor. The absorber island is supported by a silicon nitride suspension. The incoming optical power is received by the coupled antenna (not shown in the figure). Currents generated in the antenna arm are driven through a load resistor which is in thermal contact with the absorber. The absorber is heated by this current, and its temperature is read out by the TES thermistor. The absorber is plated with gold to yield the desired heat capacity. This heat capacity and the thermal link to the device wafer together dictate the time constant of the detector.

The dual-TES thermistor functions at two superconducting transitions, and is composed of two components in series: an Aluminum thermistor and and aluminum-titanium bilayer thermistor. The aluminum part of the TES has a high temperature transition, at $T_{c,aluminum} = 1.4K$. This transition allows a high noise mode with large dynamic range and was useful for laboratory testing. At temperatures below 1.4K, the aluminum side is superconducting and acts as part of the electrical leads to the bilayer. The bilayer is composed of aluminum and titanium with a transition temperature $T_{c,bilayer} \sim 0.5K$.

The POLARBEAR-I arrays were fabricated in the UC Berkeley Nanolab by Kam Arnold and were the subject of his dissertation, [4].

3.3.2 Antenna Coupled Detectors

TES bolometers have been used in other CMB experiments, e.g. MUSTANG, APEX-SZ, SPT, SCUBA-2, SPDER and EBEX, but fielded experiments have commonly used a horn array to focus radiation onto the detector. Notable exceptions include bare absorber pixels in ACT [65] and a phased antenna array in BICEP [50] [88]. For horn coupled polarization measurements, a polarized element such as an ortho-mode transducer, OMT, is used to extract a polarized signal. POLARBEAR-I uses an antenna lithographed on the detector wafer to receive incident radiation, as shown in Figure 3.8. Currents generated in the antenna are driven through the bolometer detectors.

POLARBEAR-I uses a pair of double-slot dipole antennas. Each set of double slots produces (in the time reversed sense) a polarized, circular, gaussian beam. The pair of double slots is crossed at 90 degrees so that the pixel is sensitive to polarization in two directions. Subtracting the signal of the two detectors thus yields the net polarization at that pixel, in absence of systematic errors. The POLARBEAR-I antenna is shown in Figure 3.8. Directivity and size of the antenna beam is controlled by a

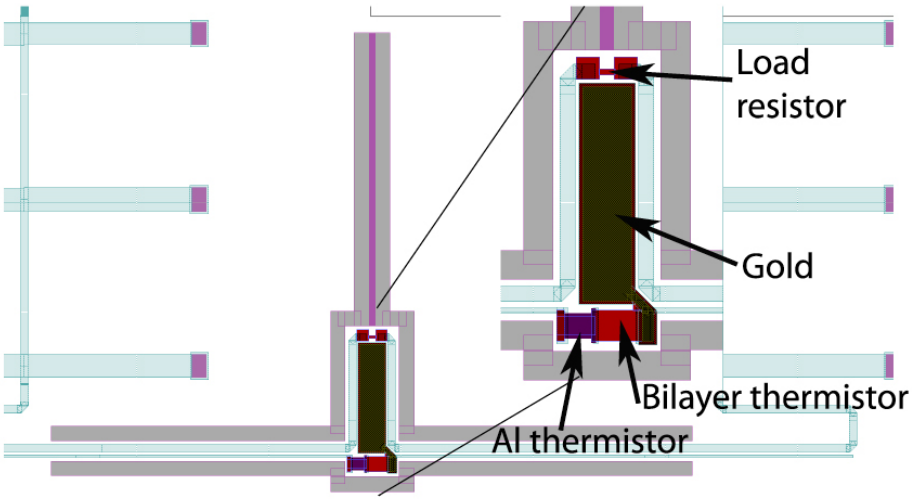

Figure 3.10: The POLARBEAR-I Bolometer. The physical components of the bolometer include the load resistor which delivers the optical signal, the gold plated absorber, and the dual thermistors. These elements are all thermally isolated from the silicon device wafer by a silicon nitride suspension.

small contacting lenslet. The contacting lenslet array is discussed in Chapter 4, and specifically the optics of this element are described in Section 4.1.

3.4 POLARBEAR-I Detector Readout

3.4.1 Frequency Multiplexing and LC Filters

We used a multiplexing scheme to read out the 1274 optical bolometers on the focal plane. This technology, developed at Berkeley, has been used in previous experiments such as APEX, SPT, and EBEX. [52] The frequency multiplexing scheme, fMux, allows eight bolometer channels to be read out by a single SQUID amplifier. This reduces the wire count into the cryostat, simplifying circuitry and reducing the electrical thermal load. In order to do this, a comb of bias frequencies is delivered on a single wire. The signal then passes through a set of inductor-capacitor (LC) filters, each of which is attached in series with a bolometer, so that each bolometer in the comb sees a unique bias frequency. The return signals from the detectors are summed before leaving the cryostat and their signals are demodulated and separated outside of the cryostat, Figure 3.11. The bias frequencies and demodulation are accomplished via external electronics fabricated by collaborators at McGill university.[3]

[3]M. A. Dobbs, et. al.

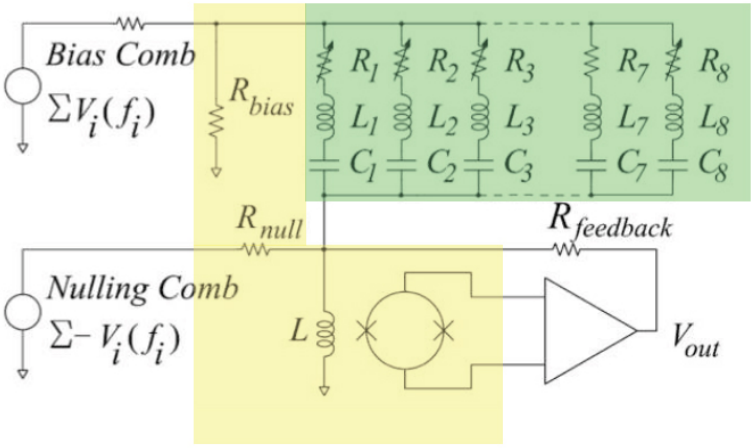

Figure 3.11: Frequency Multiplexing Schematic. The green shaded region shows the bolometers each in series with an LC filter. Eight of the filter/detector pairs are wired in parallel and receive a comb of bias frequencies, shown on the upper left. The components shown here in green all reside on a single LC circuit board, except for the bolometers labeled R1 through R8 which reside on the detector wafer. The eight bolometers are read out with a single SQUID amplifier, shaded yellow in this figure (where eight SQUIDs reside on a single SQUID board).

The LC filter circuit boards were designed at Berkeley by the author, based on previous boards used, e.g. for APEX, and with input from the collaboration.[4] The LC board must function at 250 mK and interface well with both the detector wafer and the other cold readout electronics. The boards were designed to have minimal cross-talk between detectors, particularly within a comb.

POLARBEAR-I specific constraints

APEX and SPT used similar LC boards in their readout electronics. New challenges are presented by POLARBEAR-I . The wedge shaped focal planes of previous experiments allowed the LC boards to attach at the wafer perimeter without extreme spatial constraints. In contrast, the modular POLARBEAR-I focal plane has a center detector wafer, whose perimeter is flush with other detector wafers. This modularity scheme requires that the each LC board mount beneath the device wafer it is bonded to and the circuit board footprint must be smaller than the device wafer as shown in Figure 3.12. To solve these issues, the LC board is attached to the detector wafer with flexible circuit traces (on Kapton substrate) so that it can fold beneath the de-

[4]Notably including Matt Dobbs (Post-Doc UC Berkeley, currently at McGill University), Trevor Lanting (UC Berkeley Graduate Student), and Helmuth Spieler (Lawrence Berkeley Laboratory Scientist)

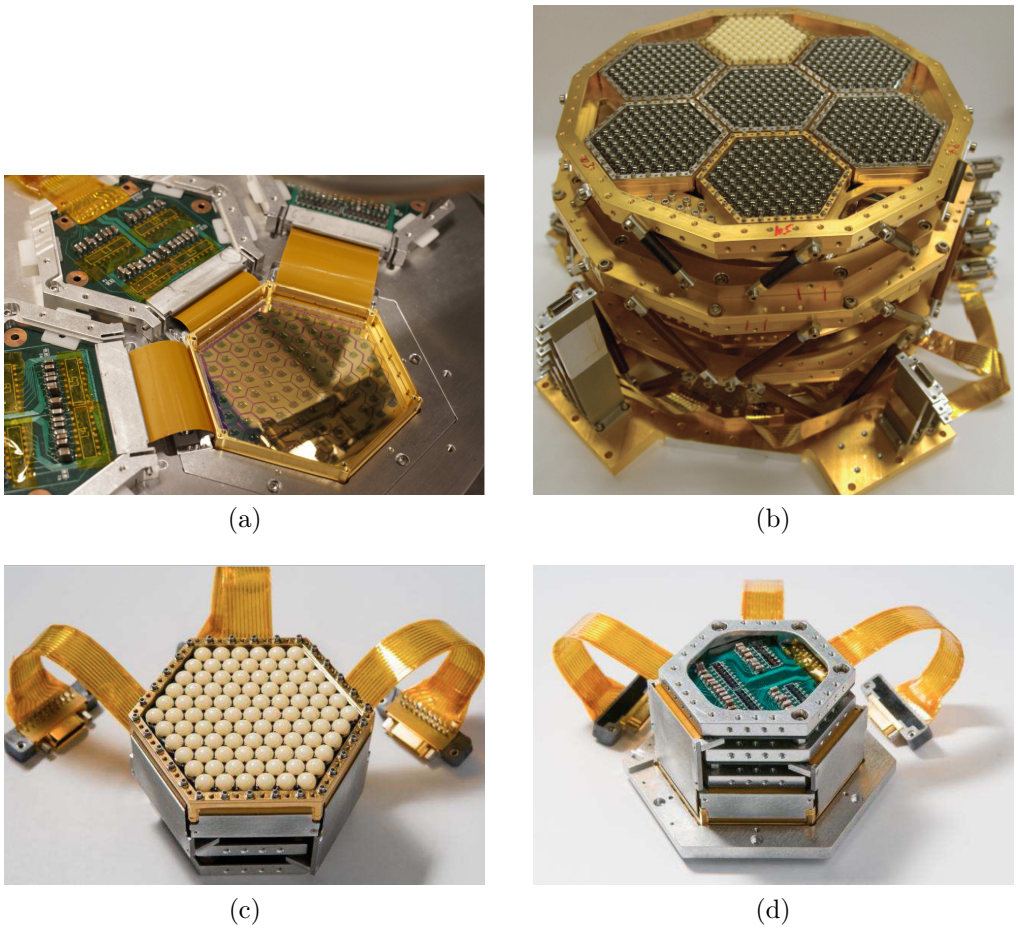

(a) (b)

(c) (d)

Figure 3.12: LC Board Mounting. The LC board footprint fits beneath the detector wafer, accommodating the center and edge elements of the modular focal plane. (a) Three LC boards are attached to each detector wafer. Here the unfolded LC boards reveal the shiny detector wafer. (b) The modular focal plane, with 7 modules, includes a center module. (c) The modular array from the sky side, showing prototype alumina lenslets. (d) The detector side of the module. Here the green circuit board is the last LC board to be folded into the module.

vice wafer, and the trace width and spacing are designed to accommodate the smaller circuit board.

Further, to retain modularity for installation purposes, it was most elegant to position the micro-Dsub connectors (leading to the SQUID card) just outside the perimeter of the focal plane. The summing point for the LC filters remains on the LC board, Figure 3.13 and the signal is carried to the edge of the focal plane mount via flexible microstrip (not shown).

LC Circuit Board Design and Fabrication

Measures were taken to reduce crosstalk between channels (see Crosstalk discussion below), including:

- Trace width and spacing set to adequately confine fields. Comparatively wide traces with small distance to ground plane were used. (see Layout Parameters below)

- Reduce chip to chip inductor coupling by staggering of inductors front to back. Since both sides of the circuit boards were used, inductors on the two sides were not placed vertically on top of each other, avoiding broadside coupling between inductor chips. The two sides of the circuit board are shown in Figure 3.13.

- Return lines directly mirror incoming lines. This reduces the cross sectional area of the loop formed by one bias channel. Thus, the inductive coupling of the bias loop is reduced.

- Ground planes between conductive layers. Specifically, we used tinned ground planes so these layers would superconduct at low temperature. Tinning was done with a "white tin immersion" layer. Unfortunately, this tinned layer was more difficult to adhere to than typical metal layers, and there was fabrication trouble with the boards cleaving along the ground plane layers. This difficulty was mitigated by pulling the ground plane back from the edges of the circuit board, so that there was an internal border of dielectric layers, which were strongly bonded together. The ground plane also serves as a thermal sink for the board. Figure 3.13 shows holes at the edges of the board with a large exposed copper area. This copper area was the interface for thermal sinking, and it was left un-tinned for good thermal contact with the detector module.

- Staggering of the frequency schedule across the inductor chip. The inductors come lithographed on chips and are diced in rows of 8. Each chip resides in one of the labeled inductor spots, e.g. "L1" in Figure 3.13. Physically adjacent inductors have the highest coupling fraction, so physically adjacent inductors did not use spectrally adjacent bias channels, i.e. if the channels are numbered 1 through 8 in order of increasing bias frequency, the order of channels across the chip is **low**-high-**low**-high: **1** 5 **2** 6 **3** 7 **4** 8

Practical constraints include:

- LC board fits under detector wafer to allow a modular focal plane with center module. This is accomplished with the flexible Kapton section shown in Figure 3.13.

- Superconductivity of traces. This was achieved with a white tin immersion layer.

Table 3.2: Circuit board parameters

Trace width	0.003”
Trace pitch	0.0107”
Dielectric thickness to ground plane	0.001”
Dielectric material	Kapton

- Ability to bond to detector wafer. Exposed copper was left on the LC board at bond pads for wire-bonding to the detector wafer.
- Thermal cycling. The LC boards operate at mK temperatures.
- Mechanical robustness. The LC boards, and flexible sections in particular, withstood a a few mounting processes, though abuse of the flexible sections was minimized when possible.
- Stability of SQUID readout. Parasitics in the bias loop were minimized by summing the return signals on LC board, as opposed to on the SQUID card.

The LC circuit boards were designed at Berkeley and manufactured by Cirexx International.[5] However, due to the issues with superconducting ground place adhesion earlier described, Cirexx plans not to fulfill more of these orders. Other vendors used for this type of part include Rigiflex.[6] Superconducting inductors were supplied by NIST.

Layout parameters

For the desired trace width and spacing, the self reactance of the traces and cross talk between traces are shown to be within the acceptable range. Board parameters are listed in Table 3.2.

Self reactance of traces in the bolometer bias loop shift the resonant frequency of the LC filter. The bandwidth of the filter compared to spacing of the frequency channels makes small variations in self reactance negligible. Band widths of the LC circuit are

$$\Delta f = \frac{R_{bolo}}{2\pi L} \simeq \frac{1\Omega}{2\pi 16\mu F} = 30KHz \tag{3.4}$$

Spacing of frequency channels on one multiplexing frequency comb is approximately 80 KHz. [55] Thus, variations in parasitic reactances of distinct bias loops are

[5]Cirexx International, Inc., http://www.cirexx.com, Santa Clara, California
[6]Rigiflex, http://www.rigiflex.com, Anaheim, California

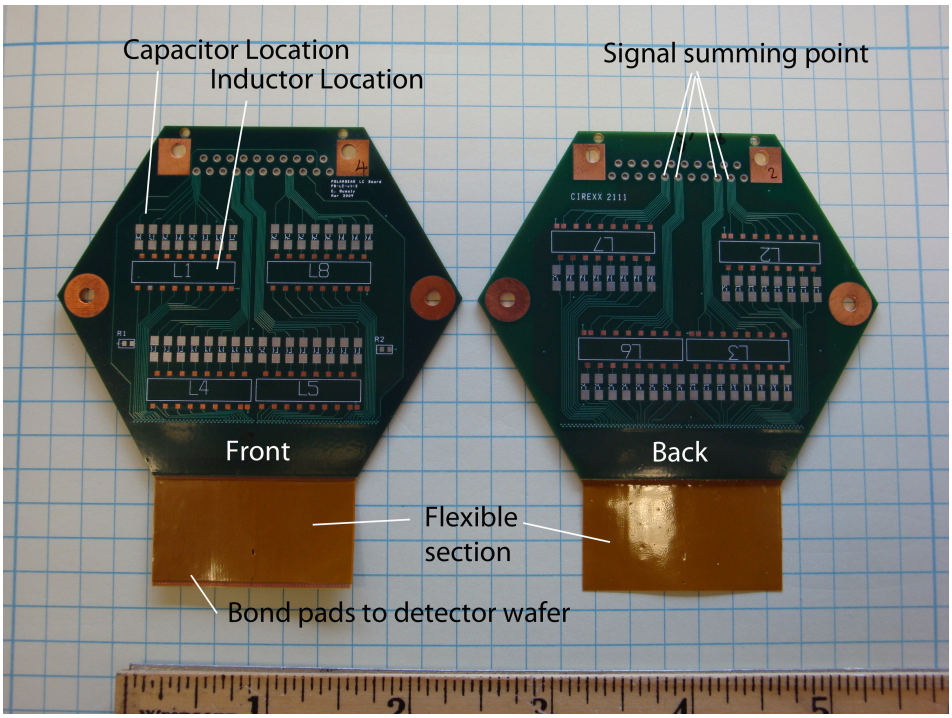

Figure 3.13: LC filter circuit board. The front and back of the LC board are shown. Note that the inductor and capacitor locations are vertically switched on the back side, to reduce inductor-inductor coupling. The flexible Kapton section is shown, with copper bond pads to the wafer on the front side only. The signals on each bias comb are associated with a single inductor chip, and the bolometer bias loops are summed at a DSub connector at the top of the board.

allowed at $\sim 1\%$ of the nominal value. Parasitic reactances that are present in every channel shift the entire comb of frequencies.

Self reactance calculations

For transmission line geometry where the width of the line is much greater than the distance to the ground plane, parallel plate formalism may be sufficient to describe the capacitance. The inductance of the line is then

$$L = \frac{\epsilon_r \epsilon_0 \mu_0}{C} \tag{3.5}$$

For the chosen trace geometry, self capacitance and inductance of the lines does not follow a simple parallel plate formalism. Instead, closed form expressions were used which include effects of fringing fields [7] and [40] (Appendix C). Results are listed in Table 3.3 and are valid to 2 % for this trace geometry. For a realistic board geometry, the total parasitic reactances in series with the bolometer will be less than

Table 3.3: Self Reactance of Traces

	Width mil	Thickness mil	Spacing (center to center) mil	Height (above ground plane) mil	Dielectric ϵ_r unitless	C pF/inch	L nH/inch
Outer Trace	3	0.7	10.7	1	3.9	2.3	9.0
Inner Trace	3	0.7	10.7	1 to lower gnd 4 to upper gnd	3.9	5.8	4.2

$C_{parasitic}$ = 25 pF and $L_{parasitic}$ = 62 nH. Within a bias comb, these parasitics are expected to vary by less then 10% based on trace length differences on the LC board. The values of the LC filter components are L = 16 μ H and C = 1.6 nF to 0.16 μ F, dependent on bias frequency. Thus, variations in the parasitic reactances within a bias comb are less than 1% of these nominal LC filter values.

Crosstalk

The bolometers are voltage biased, and the optical signal (which causes a change in bolometer resistance) is read out by measuring a change in current through the bias circuit. Thus, crosstalk may be defined as the ratio of current induced in one bias loop due to current in a neighboring loop.[52]

The parasitic coupling of lines in the bias circuits can be investigated using a simple analytic approximation to the lines, or by using an electromagnetic simulator, such as Sonnet (Sonnet Software, North Syracuse, NY). Both methods were employed here.

A simple model for mutual inductance of traces over a ground plane is [40]

$$M = \frac{L}{1 + (\frac{D}{H})^2} \tag{3.6}$$

where D is the distance between traces, H is the height of the trace above the ground plane, and L is the self inductance of the line. The voltage induced by bias loop i at frequency ω_i in bias loop $(i+1)$ is (for a sinusoidal signal)

$$V_{i+1} = i\omega_i M I_i \tag{3.7}$$

Thus, for our parameters, the current crosstalk per inch will be

$$Crosstalk = \frac{|I_{i+1}|}{|I_i|} = \frac{\omega_i M}{|Z_{i+1}|} = \frac{\omega_i M}{\sqrt{R_i^2 + (\omega_i L_i - \frac{1}{\omega_i C_{i+1}})^2}} = 3.9 \times 10^{-6} \tag{3.8}$$

where $R_i = R_{i+1} = 1Ohm$, $L_i = L_{i+1} = 16\mu H$, $\omega_i = 100$ KHz, and $C_{i+1} = 70$ nF (corresponding to $\omega_{i+1} = 150$ KHz).

The above calculation for inductive crosstalk is a simple calculation for loops sharing the same axis. On the flexible portion of the circuit, the bias loops have parallel axes and are adjacent to each other.

For this type of case, a Sonnet simulation by Mike Myers [7] it is shown that the voltage crosstalk for a similar geometry is 0.04 %. This simulation was done for slightly different board parameters then used in the POLARBEAR-I circuit board. If scaled by a factor of two, it corresponds to 3 mil trace width, 8.5 mil pitch, and 2 mil Fr4 dielectric. These parameters are similar to the POLARBEAR board parameters.

3.4.2 SQUID Amplification

Inside the cryostat, the detector signal passes through one cold amplification stage, which contributes less thermal noise than a warm amplification stage would. For the cold amplification, we used SQUID transimpedance amplifiers which produce a voltage signal from a current input, with an amplification factor. This amplifier was chosen for its bandwidth and noise properties.

The SQUID arrays are composed of 100 superconducting loops in series, each with parallel Josephson junctions. The voltage signal is generated across these junctions. The signal to amplify, a current, is driven through an input inductor in proximity to the superconducting loops. That inductor, or input coil, changes the flux through the superconducting loops. Due to quantum mechanical flux quantization, the voltage output of a the SQUID is sinusoidal with flux through the loop, and the largest response occurs at the steepest part of the sine curve (equivalent to zero or 180 degree phase on a simple sine function). [91]

Superconducting quantum interference device amplifiers, SQUIDs, were chosen for high gain over a large bandwidth spanning the entire frequency bias comb. [53] [54] This means that each of the eight multiplexed detectors uses a single SQUID amplifier. The schematic for SQUID amplification of each bias comb was shown in Figure 3.11, where the yellow shaded part represents the components on the SQUID amplification circuit boards. Similar to the detector biasing, a feed back loop is used to keep the SQUID response at a linear response point over the fMux bandwidth. The large bandwidth accessible naturally works with an fMux system and is scalable to reading out more channels than used in the POLARBEAR-I fMux system. [51]

The fabricated SQUID board is shown in 3.14. The SQUID amplifiers are also grouped in sets of eight on a circuit board, so each circuit board reads out 64 detectors. There are clearly great advantages of this for assembly complexity and thermal load. One challenge of the cryogenics, previously discussed, was keeping these circuit boards below the $\sim$ 6K superconducting transition. The SQUID circuit boards were

[7] internal memo, UC Berkeley

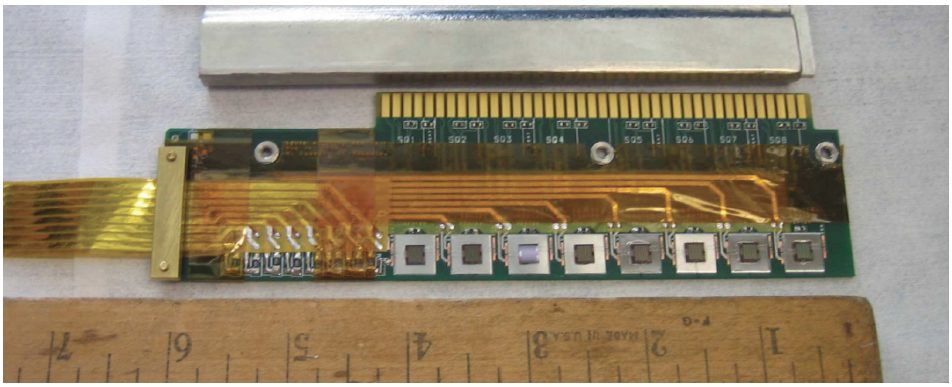

Figure 3.14: SQUID Amplification Circuit Board. The SQUID amplifier chips are sitting on the eight squares of niobium foil, at the lower edge of the board. The niobium foils superconduct and pin stray flux. The SQUID board is also contained in a cryoperm sleeve (shown at top border of the photo) for magnetic shielding from external signals. The input signals from the detectors enter on flexible microstrip (at left) and the SQUID card plugs into the rest of the read out with the pads at the top of the board.

ultimately kept at $\sim$ 4K, which yielding high gain. The SQUID voltage signal is then read out by room temperature electronics.

Chapter 4

Monochromatic Lenslet Array

POLARBEAR is pioneering a new method for coupling electromagnetic radiation onto the detector: via lenslet-antenna-coupled bolometer. The main advantages of this technology lay in broadband, or multichroic systems and are discussed Chapter 2.2. Although POLARBEAR-I is a single frequency experiment, it has been a necessary platform for testing the antenna-coupled bolometers in a kilo-detector deployment. Antenna-coupled systems also require focusing optics, i.e. the lenslet array. The POLARBEAR-I lenslet array was a main focus of my thesis work and the first such optical system deployed in a CMB measurement.

4.1 Optics Theory for Planar Antenna Beam

4.1.1 Antenna Coupling and Focusing Lenslet

Historically, most CMB experiments have used a horn to collect radiation. This horn directs electromagnetic radiation to a detector and the horn geometry shapes the beam of that detector. In contrast, the antenna-coupled bolometer system, the optical power drives a current in the antenna, and the bolometer detects that electrical current. The beam of the POLARBEAR antenna-coupled bolometer is controlled by the shape of the antenna and a contacting lenslet. (Phased arrays can be used to control the beam shape and are not discussed here.)

The contacting lenslet is needed to modify the directivity of the antenna beam. POLARBEAR antennas are planar, as they are lithographed on the device wafer. By symmetry, a planar antenna in free space will radiate equally in both half spaces adjacent to the antenna. In order to give the beam forward direction, a high dielectric is placed on the sky side of the antenna. With a high dielectric present on one half-space, the ratio of radiated powers varies between $\epsilon^{1/2}$ to $\epsilon^{3/2}$, depending on the shape of the antenna. [69] For simple slot and dipole antennas, the power ratio of the dielectric half-space to vacuum is $\epsilon^{3/2}$:1. [26] POLARBEAR uses antennas fabricated

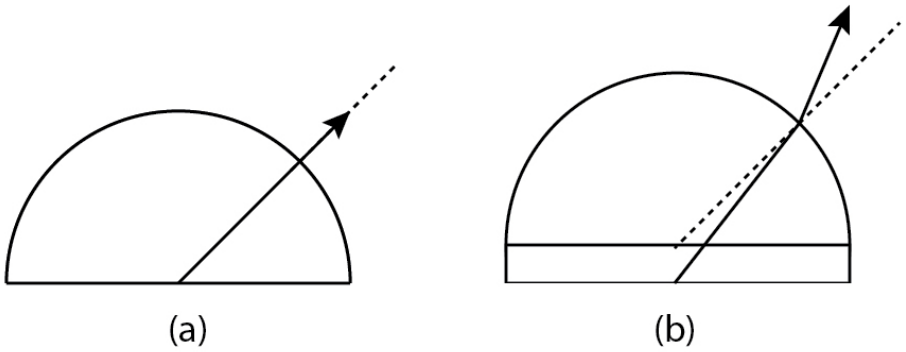

Figure 4.1: Lenslet Optics. (a) A pure hemispherical lenslet has no focusing power for an antenna at its center. (b) With a spacer thickness inserted, rays leaving the antenna position are no longer normal to the hemisphere tangent plane. Rays are bent away from normal, reshaping the antenna beam to a smaller angle. Here the lenslet and spacer are taken to be the same material with a high dielectric constant, and reflections are not shown.

on silicon wafers, so silicon is used as the half-space material. For silicon, this ratio $\epsilon^{3/2}$:1 is approximately 40:1.

For additional control of the beam shape, the high dielectric material can be shaped to act as a focusing lens. To understand this, we can first consider the ray limit. In this limit, a large hemispherical lens centered on the antenna will have no focusing power. Each ray will strike the hemisphere at normal incidence to the tangent plane. Since normal rays are not deflected by Snell's law, the hemisphere will not affect the shape of the beam. However, placement of a high dielectric pedestal between the antenna and the hemisphere changes the angle of the rays with respect to the hemisphere boundary. These non-normal rays will be bent according to Snell's law. This has the net effect of narrowing the antenna beam, as shown in Figure 4.1.

Note that the full antenna beam shape (including the anti-reflection coating) depends on diffraction effects. These effects are described in Roger O'Brient's thesis, including simulation code which calculates the beam by re-launching the electromagnetic waves from bound currents at the lenslet surface. [69]

4.1.2 Quarter-Wavelength Anti-Reflection Coatings

The increased beam directivity and focusing power of the lenslet is achieved by using a material with a high dielectric constant. However, reflections occur at the boundary of the high dielectric and vacuum. These reflections cause signal loss and create a systematic error in polarization measurement. (The pedestal or "spacer"

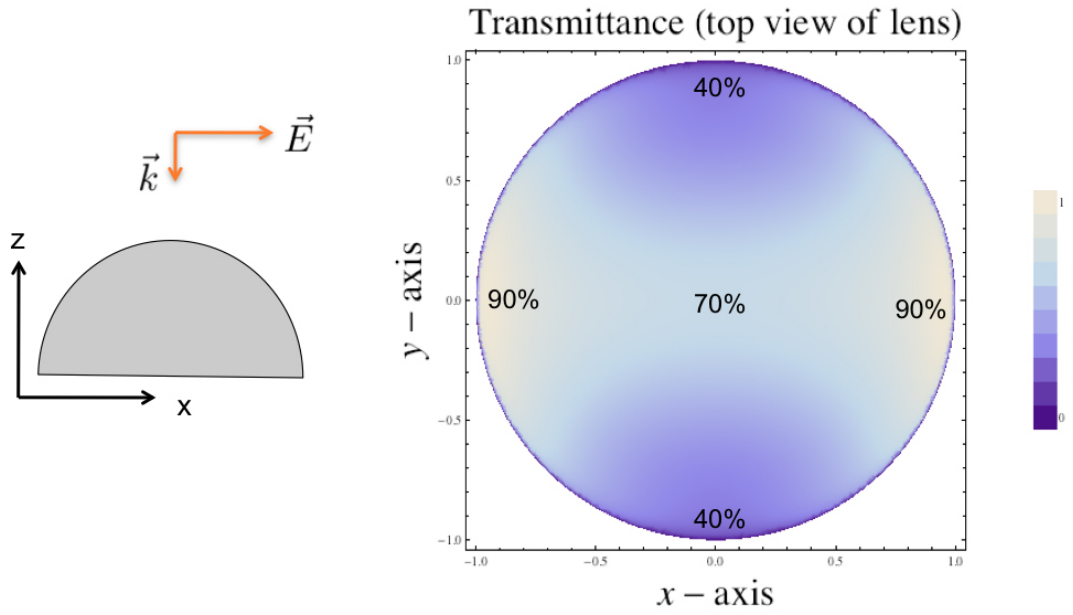

Figure 4.2: Transmittance of a linearly polarized wave. The axes relative to the incident wave are defined on the left. The transmittance percentage is shown for all positions on the hemisphere, projected as a view from the positive z-axis. Percentages in the middle and at the edge of the optically active area are shown. The POLARBEAR-I lenslet is optically active to about $0.9 * Radius$. At larger distance from the pixel center, total internal reflection occurs.

shown in Figure 4.1 should be the same material as the hemisphere to avoid reflections at the hemisphere-spacer boundary.)

The reflected power at an optical index discontinuity is given by the Fresnel equations at normal incidence. The reflection at a silicon-vacuum interface used in POLARBEAR is

$$R = (\frac{n_{silicon} - 1}{n_{silicon} + 1})^2 \simeq 30\% \tag{4.1}$$

This large loss of signal translates directly into more observing time needed for a detection, costing both time and money which might render an experiment infeasible. However, signal loss is not the worst problem caused by reflections. According to Fresnel's equations, reflections are highly polarized, and they also depend on the angle between the E-field and the tangent plane at the interface. The dependance of reflection on incident angle comes from the boundary conditions on the E-field. Thus, the amount of a linearly polarized light transmitted at the lenslet surface varies with position on the hemisphere.

The precise dependence of reflection on incident angle can be calculated from the Fresnel equations. [36] The equations depend on the optical indices on the incident

and transmitted sides of the boundary, as well as the angle of the ray with respect to normal on both sides of the interface. Where the E-field is perpendicular to the plane of incidence, the amplitude reflection coefficient is

$$r_{\perp} = \frac{n_{inc}cos\theta_{inc} - n_{trans}cos\theta_{trans}}{n_{inc}cos\theta_{inc} + n_{trans}cos\theta_{trans}} \tag{4.2}$$

Where the E-field lies in the plane of incidence,

$$r_{\parallel} = \frac{n_{trans}cos\theta_{inc} - n_{inc}cos\theta_{trans}}{n_{inc}cos\theta_{trans} + n_{trans}cos\theta_{inc}} \tag{4.3}$$

The reflected power is the square of this coefficient.

To illustrate the effects of this angular dependence of reflection, the Fresnel equations were applied to a linearly polarized plane wave signal incident on a hemispherical silicon dielectric. The result of this calculation, shown in Figure 4.2, is preferential transmission along the polarization direction. Thus, a linearly polarized circular beam will be made elliptical by reflections at a hemispherical surface.

The POLARBEAR-I focal plane consists of pairs of crossed double slot dipoles, so each pixel is sensitive to two orthogonal polarizations. Subtraction of the signals from the two paired antennas yields the net polarization seen at that pixel. Imagine, however, that each beam is elliptical with respect to the antenna. Then, subtraction of the two signals will leave a clover pattern. This quadrupole signal will present as the measured polarization signal. Thus, minimizing reflections is critical to making a sensitive polarization measurement. A quadrupole subtraction pattern is shown in 4.3.

To recover signal and avoid polarized reflections, we use an anti-reflection layer at the surface of the lenslet. For a single frequency of light incident on a flat geometry, an anti-reflection coating can be made from a quarter-wavelength coating. The coating thickness is such that, at normal incidence, the primary and secondary reflected rays cancel in phase. An example these reflections is shown in Figure 4.4, however the diagram is drawn at non-normal incidence for illustrative purposes. At normal incidence, all of the rays are in the vertical direction, and the multiple reflections cannot be clearly diagrammed.

The general solution to transmittance through a single dielectric slab can be calculated via the standard matrix treatment. [36] The E- and H-fields just outside of a dielectric with optical index n and thickness d (on sides I and II respectively) are related through the characteristic matrix as follows

$$\begin{pmatrix} E_I \\ H_I \end{pmatrix} = \begin{pmatrix} cos(k_0nd) & \frac{i}{n}sin(k_0nd) \\ insin(k_0nd) & cos(k_0nd) \end{pmatrix} \begin{pmatrix} E_{II} \\ H_{II} \end{pmatrix} \tag{4.4}$$

This expression is taken at normal incidence and is derived from the boundary conditions on each side of the dielectric. Note the the expression explicitly involves

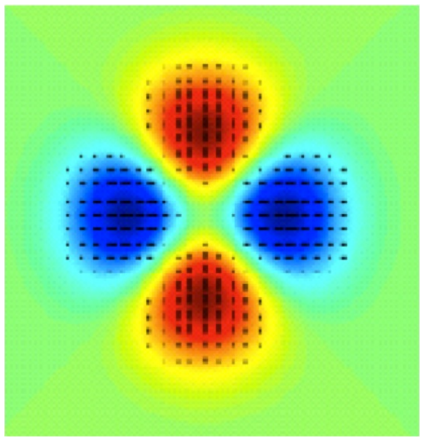

Figure 4.3: Quadrupole systematic error. Differential ellipticity, or differencing orthogonal elliptical beams, yields this quadrupole systematic error. Here, the red and blue regions correspond to an excess and deficit of power respectively, and the associated polarization is indicated with black lines. Differential ellipticity could be caused by polarization dependent reflections at the lenslet surface, as shown in Figure 4.2.

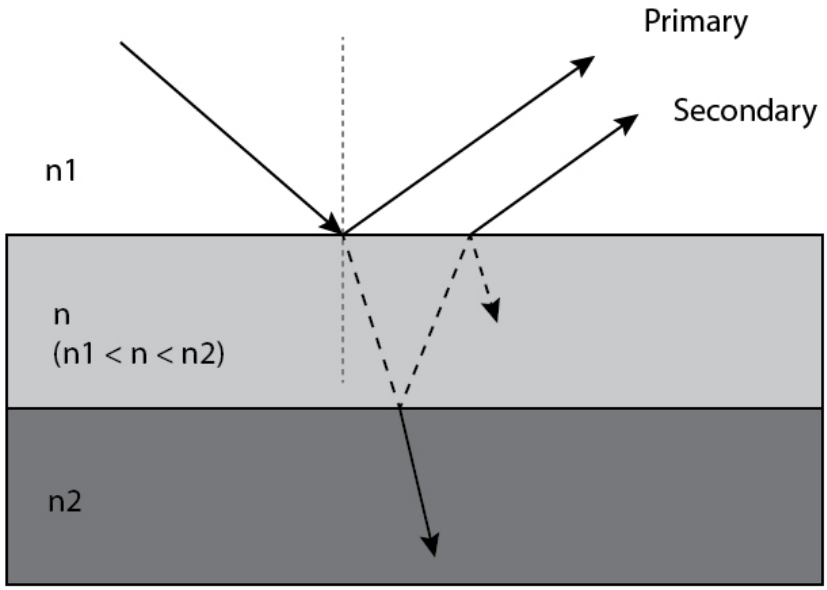

Figure 4.4: Reflections in a dielectric layer. Reflections in an intermediate matching layer are shown at non-normal incidence. The "primary" and "secondary" reflected rays are labeled, but the reflections within the sample are actually an infinite series in which power decreases with each reflection. Thus, considering the relative phase of the primary and secondary rays is sufficient to calculate first order effects.

only the dielectric index n and not the indices of the surrounding media. However, the indices of the incident and transmitted media do come into play due to the relative magnitude of the E- and H-fields. Thus, from the matrix expression, a reflection coefficient can be calculated which involves all of the indices in the optical system

$$R = \frac{n^2(n_I - n_{II})^2 cos^2(k_0 nd) + (n_I n_{II} - n^2)^2 sin^2(k_0 nd)}{n^2(n_I + n_{II})^2 cos^2(k_0 nd) + (n_I n_{II} + n^2)^2 sin^2(k_0 nd)} \tag{4.5}$$

Note that this expression simplifies when the phase through the dielectric is set to zero, e.g. $cos(k_0 nd) = 0$ and $d = \frac{\pi}{2nk_0} = \frac{\lambda}{4n}$. In that case,

$$R = \frac{(n_I n_{II} - n^2)^2}{(n_I n_{II} + n^2)^2} \tag{4.6}$$

Thus, the reflected power is zero when

$$n = \sqrt{n_I n_{II}} \tag{4.7}$$

Note this is perfect cancellation for zero reflected power only works for a flat geometry at normal incidence. Applied to a curved surface, the full solution is more complicated as it involves a range of angles and diffraction effects of bound currents at the interfaces. Nonetheless, this flat geometry approximation is the starting nominal point for development of coatings. Additionally, a flat geometry is a good approximation at the center of the lenslet, where the bulk of the antenna power is directed and where the tangent plane to the lenslet surface is parallel to the antenna conduction plane.

One effect of the hemispherical geometry is that the optical path length (vertically through the material) changes as a function of angle on the hemisphere. Thus, we considered optimizing the coating by changing the coating thickness as a function of angle on the hemisphere. As in the planar geometry, this calculation involves phase cancellation of the primary and secondary reflected rays, and the details were shown in Roger O'Brient's thesis. [69] The deviation from the nominal quarter-wavelength thickness was shown to be less than realistic machining tolerances, i.e. corrections to the thickness were less than 0.001". Therefore, it is not an effect we attempted to control in fabrication.

4.2 Fabrication of the POLARBEAR-I Lenslet Array

4.2.1 Array Geometry

POLARBEAR-I is pioneering the antenna coupled detector technology, for which a focusing lenslet is necessary as discussed in section 4.1.1. The precise shape and size of this lens is a choice with many factors such as coupling well to the rest of the optics, beam width, and observing time efficiency.

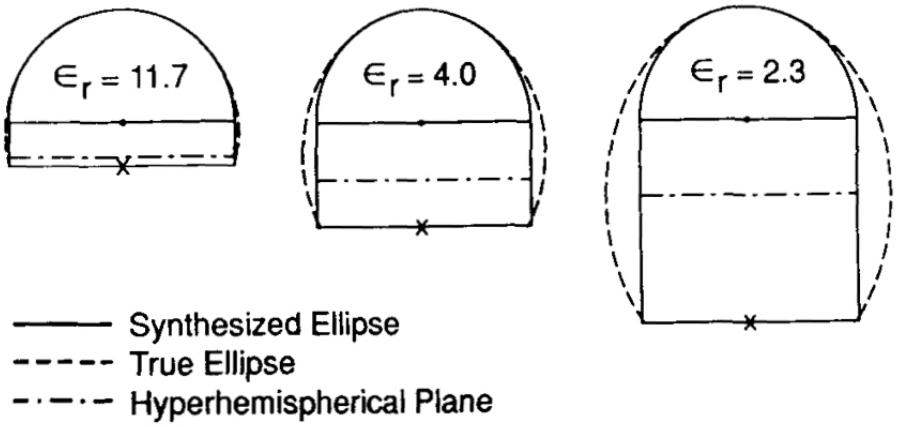

Figure 4.5: Simulated ellipse. An elliptical lens shape can be approximated by a hemispherical lens on a flat extending spacer. Shown here is the geometry of the approximation for lenses of different dielectric constants. The simulated ellipse on the left, which has a dielectric constant representing silicon, is a very close match to a true elliptical lens shape. Figure from [27].

One consideration is maintaining a Gaussian beam. At each aperture or lens, the far field pattern of incident radiation is a Fourier transform of the aperture distribution. Because the Fourier transform of a Gaussian profile remains Gaussian, this beam will retain its shape through the optical chain. Gaussian beams are thus used to minimize sidelobes. [29]

Elliptical lenses have been shown to couple well to Gaussian beams with a planar equiphase beam waist just above the surface of the lens. [27] The equiphase beam waists are naturally suited for the flat POLARBEAR-I focal plane. A true elliptical lens shape would be difficult to machine, but luckily the shape can be sufficiently approximated by the hemisphere and spacer combination discussed earlier, e.g. Figure 4.1. Figure 4.5 shows the geometry of this approximation.

For ease of fabrication, we used a simulated ellipse geometry. The simulated ellipse consists of a hemisphere on a spacer, as shown in Figure 4.1. In fact, from a fabrication standpoint, the simulated ellipse is a more attractive option than the true ellipse. Unlike ellipses, spheres can easily be ground in bulk, see section 4.2.2. Due to widespread commercial availability of high precision spheres and ball end mills, the prototyping and anti-reflection coating process was much easier than it would have otherwise been. Having the lenslet diameter be a standard size, $\frac{1}{4}$ inch, was an unforeseen boon which also expedited the process.

The diameter of the POLARBEAR-I pixel was chosen to be $R = 1.6\lambda$, with λ being the wavelength at the center of our observing band in free space. [4] This size is a compromise with trade offs in pixel sensitivity and mapping speed. Having set the

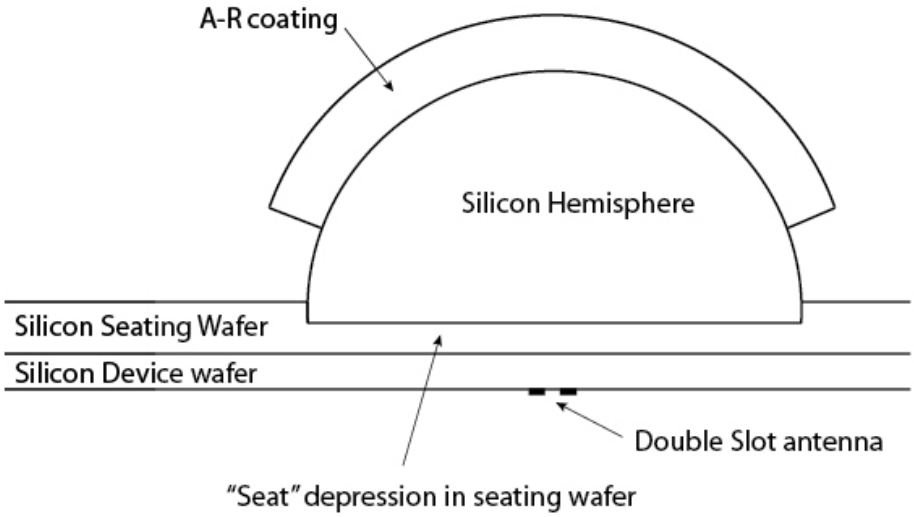

Figure 4.6: Lenslet cross section. The lenslet is seated in a "seating wafer" which holds all of the lenslets in the lenslet array. The seating wafer sits on top of the device wafer. The ground plane for the slot antennas lies on the far side of the device wafer, so the combination of the seating wafer and device wafer serves as the extension length for the simulated ellipse lens. This schematic is not to scale.

pixel radius, the extension length matches the lens to a corresponding ellipse. Beams with $0.36 < \frac{L_{ext}}{R} < 0.39$ have sufficient directivity and Gaussisity, thus these were chosen as our bounds for physical tolerance of the extension heights. [4] [27]

4.2.2 High Dielectric Focal Plane Elements

The POLARBEAR-I focal plane is composed of a detector wafer and a contacting lenslet array. The lenslet array consists of a high dielectric extension, composed of the device wafer and seating wafer, and anti-reflection coated hemispheres which form an array of simulated elliptical lenses. Location of the hemispheres on the array is achieved by etched cylindrical depressions in the spacer wafer. Figure 4.6 shows a cross section schematic of the design.

The POLARBEAR-I detectors, Transition-Edge-Sensor bolometers, were fabricated on silicon wafers, a common substrate for semiconductor devices. The silicon part of the detector wafer is on the sky side of the antenna ground plane. Thus, for continuity of optical index in the spacer and hemisphere, silicon was used for the spacer wafer and the hemisphere. The bulk thickness of silicon traversed is 7.51 mm, or 12.7 $\lambda_{silicon}$, so low loss through the silicon is important. Amorphous alumina (i.e. aluminum oxide, Al_2O_3) is also a low loss, high transmittance dielectric, it's optical properties are discussed in Appendix A.2.

Silicon Transmittance

Transmittance of silicon for all of the focal plane constituents has been measured. Purity, lack of dopants, and continuity of crystal structure yield high optical transmittance through silicon at millimeter wavelengths.

High quality silicon is particularly important in the hemisphere component of the lenslet, as this is the thickest section of silicon the photons traverse. To ensure high optical transmittance, high purity, high resistivity silicon is used. The silicon hemispheres were manufactured to specification by Rayotek Scientific[1]. Rayotek secured an ingot of silicon, and we optically tested a sample before the machining commenced. Testing was done on a Michaelson Fourier transform spectrometer at 4 Kelvin from 100-900 GHz, to ensure low loss. See Appendix A.3 for the measurements.

Hemisphere Fabrication

Machining of hemispheres is accomplished by grinding whole balls first and then bisecting them into hemispheres. The bisection was done via grinding, so that for each sphere produced, we received one hemisphere. Ball machining is a well known process, and is extensively used in industrial manufacture of ball bearings. The rough cut pieces begin as silicon cubes with rounded corners. Large numbers of these cubes are ground between parallel plates (typically spinning parallel plates) until the balls are round and have uniform diameter. During this step there is an economy of scale as of the pieces are all ground in one batch. The bill for 700 hemispheres plus a sample for optical testing was approximately $14k in 2008. Rayotek verbally confirmed that they use this standard method, and they were able to supply hemispheres with the following specifications:

Radius = 0.125" +/- 0.0005"
Surface finish: 60/40 scratch/dig
Flatness (on the bottom of the hemisphere): 0.0002"

The worst contributor to the hemisphere tolerance was variation in the sphere bisection height. The lenslets need not have used hemispheres, as the balls may theoretically be ground to a partial section at an arbitrary height.

Spacer Wafer Fabrication

The seating wafer contacts the device wafer and sets both the extension length on the simulated ellipse and controls alignment of the lenslet relative to the antenna. The seating wafer is 800 +/- 25 μm thick with an average seat height of 660 μm, see

[1]Rayotek Scientific, San Diego, CA http://www.rayotek.com

Wafer	Center	Flat	Right	Opposite Flat	Left	Average
S9.9	681	669	657	662	657	665.2
S10.1	687	663	653	656	653	662.4
S10.4	688	663	653	660	643	661.4
S11.2	677	652	641	650	637	651.4
Average of wafers						660.1

Table 4.1: Seating Wafer Etched Thickness in μm. The thickness through the etched part of the lenslet seat was measured with a micrometer at the center of the wafer, the flat edge of the wafer, the right side, the side opposite of the flat, and the left side of the wafer. The wafer was oriented with the flat of the wafer at the top and the etched seats facing the viewer. Averages across the wafer and averages of these four wafers are shown.

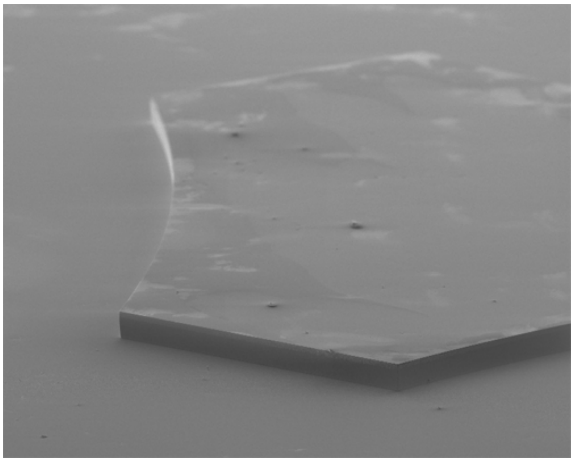

Figure 4.7: Scanning electron micrograph of a Bosch etch. This picture shows a pillar made by the same process which is used to make the POLARBEAR-I lenslet seats. Photo credit: Kam Arnold

Table 4.1, so that the depth of the etched seat is on average 140 μm. The device wafer thickness is 500 μm, so the total extension length of the simulated ellipse is 1160 μm.

The seats are radially oversized by 20 μm to allow for size variation of the lenslet radii. This tolerance aligns the lenslet on top of the antenna to 20 μm, which is $\lambda/100$ in free space or $\lambda/30$ in silicon. The seating wafer as a whole is aligned to the device wafer through alignment marks and transmission infrared microscopy with an error subdominant to the positioning of the lenslets on the seating wafer. The AR coated hemispheres are located in the seat and adhered with epoxy as described in 4.2.4.

The seating wafers are etched in the UC Berkeley Nanolab by Kam Arnold and Aritoki Suzuki with a Bosch trench etch (anisotropic) process[2]. The Bosch process uses a reactive ion etch (RIE) where an RF source accelerates ions directionally to the etch surface. In the RIE process, the physical etch due to the directionality of the ions dominates over the isotropic chemical etch. The RIE process is alternated with a gas that creates a protective polymer layer isotropically on all surfaces. The polymer is etched away on the broadside of the wafer, but it protects the side walls of the seat from the chemical etch, allowing crisp sidewalls of the lenslet seats, see Figure 4.7. The resultant seat profile is 90 $\pm$ 1 degrees according to the Berkeley Marvell Nanofabrication Laboratory manual [3].

4.2.3 Anti-Reflection Coating Materials

Several fabrication schemes were considered for manufacturing the quarter wavelength AR coatings. A perfect matching layer for silicon is, at 150 GHz, n = 1.84 and thickness 0.0107". This length scale is quite thick for deposition methods used in thin film AR coatings for visible light. However, it is small by machining standards; a typical machining tolerance, 0.001", is 10% of the coating thickness. The prospect of individually machining the surface profile of each coating, for of order kilo-pixels, seems unfeasible. We searched for methods which were more naturally scalable.

We put the most exploratory effort into two fabrication schemes: molding and thermoforming. The molding process consists of making a mold which would cast an epoxy shell onto a hemisphere. This process is described in further detail in Chapter 6. Fellow graduate student Roger O'Brient tried some of the early mold tests. These tests were hampered by his attempt to cast the entire lenslet array antireflection coatings as a single piece. Since that time, we have discovered that it is easier to achieve good tolerances and to release the molded part if the mold is for only a single pixel's AR coating. Precision to < 0.001" can be achieved by making the mold pieces cylindrically symmetric and using slip fitting parts. Many of these molds could be used in parallel for high volume production.

By contrast, the process of thermoforming is easily suited to producing many coatings at once, at least in their rough form. Thermoforming uses vacuum and heat to mold a sheet of plastic over a form. The process begins with a sheet of material held in a vacuum tight frame. The material is heated past its glass transition temperature (where it is malleable but viscous) but below the melting point. A vacuum is then applied in the frame, and the material is vacuum-adhered to whatever shape or mold is inside the frame and allowed to cool. For us, making hemispheres, the vacuum form was high precision ceramic hemispheres (alumina) half embedded in a porous metal

[2]F. Lärmer, A. Schlip, A Method of Anisotropically Etching Silicon, Licensed from Robert Bosch GmbH: US Patent No. 5,501,893 (1996)

[3]STS2 instrument: Surface Technology Systems (STS) Advanced Silicon Etch (ASE), http://nanolab.berkeley.edu/labmanual/chap7/7.22sts2.pdf

substrate through which vacuum is applied. We chose to develop thermoforming for POLARBEAR-I because early tests yielded better tolerances than molding and thermoforming naturally lent itself to batch production. The POLARBEAR-I coatings were commercially thermoformed by Welch Fluorocarbon[4]. Welch was very easy to work with and helped iterate to improve the product.

Many polymers can be used for thermoforming, as they easily exhibit a glass transition. We tested a selection of thermoformable materials for index and loss below 4K. Transmittance of these materials in the millimeter range is shown in Appendix A.1 along with the optical indices and measured loss tangents.

From these materials, we selected polyetherimide (PEI) for the POLARBEAR-I AR coatings. PEI is a thermoformable plastic and goes by the trade name Ultem-1000. PEI has an optical index of n=1.7, measured at 1.2 kelvin and 100 to 900 GHz. The optimal quarter wavelength coating would then be 0.0115". Of the available gauges, 0.012" and 0.015", we used the 0.012" thickness for thermoforming. The thermoforming process stretches and thins the sheet, and the 0.012" gauge yielded a closer match to the ideal thickness. The resultant thickness was between 0.010" and 0.011" for the POLARBEAR -I coatings. To account for PEI shrinkage upon cooling, the ceramic balls used in the thermoforming mold were increased from diameter 0.25" to 0.253". This adjustment ensured continuous contact area between the cooled PEI coating and the silicon lenslet. The rest of the recipe (including temperature, vacuum setting, and process rates such as cooling time) was proprietary to Welch Flurocarbon. The thermoforming company had to be careful to minimize two possible defects with the recipe: pull-by and bubbling.

Pull-by is the industry term for a thickness defect at the first point of contact between the thermoforming material and the form. This first contact can cool and contract more than the rest of the sheet, causing increased thickness at that point. In our application, the first point of contact is the north pole of the hemispheres. Pull-by can be seen when looking through the optically transparent PEI hemisphere, as the thickness variations will deform the background image. Looking at the straight tubes of florescent lights through the material is a good way to spot pull-by.

Inclusions of bubbles can be a problem as well. PEI is a hydrophilic material, and it requires baking to shed moisture accumulated by exposure to atmosphere. If incorrectly processed, the final part will have bubbles formed from the vaporization of residual water in the bulk of the material.

The thermoforming area must be kept as clean as possible in order to avoid contaminants of stray particles and fibers which are often found embedded in the PEI. Embedded particulates are found in the source material before thermoforming as well, so there is a limit to the purity that Welch can deliver. We sourced PEI through Ajedium[5] and are currently investigating sources of higher purity PEI. The thermo-

[4]Welch Flurocarbon, Dover, NH, http://www.welchfluorocarbon.com . Primary contact Scott Behner

[5]Ajedium Films, Newark, DE, USA, http://www.ajedium.com

forming at Welch is not done in a clean room, but the PEI is kept in a protective carrier between steps. The sheets are cleaned with a high pressure air gun before thermoforming. The thermoformed part is shown in Figure 4.8(a).

4.2.4 Fabrication process

AR Coating Preparation and Adhesion

The fabrication process for adhering the AR coatings is shown in Figure 4.8, beginning with the thermoformed sheet and illustrating the process through the finished AR coated silicon hemisphere.

Figure 4.8: AR Coating Fabrication

Steps (a) through (m) illustrate the procedure of adhering PEI to the lenslet.

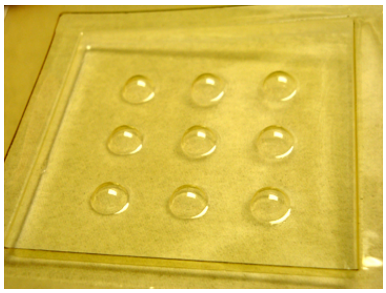

(a) The PEI domes come in this thermoformed sheet. The impression of the thermoforming frame can be seen as a square enclosing the nine hemispherical protuberances.

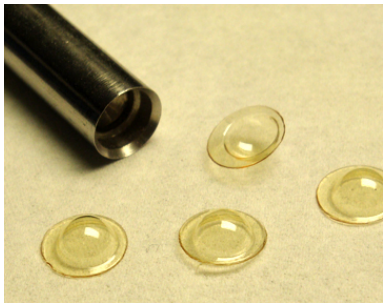

(b) The thermoformed sheet is rough inspected under the microscope for easy to spot defects. Possible defects were described in section 4.2.3. Once inspected, good coatings are punched out of the sheet. The punched out coatings can be cleaned in a beaker of methanol, agitated, and removed for another round of inspection. Free of the sheet, the clean coatings are now easier to inspect under the microscope. Small bubbles and particulates less than 1 mil were deemed acceptable, particularly if not near the north pole of the hemisphere (where the most optical power from the antenna beam passes through the coating). Coatings with metallic particulates are never allowed.

(c) The punched coatings are mounted in a lathe and sandwiched between these custom parts: a female cavity and a ball bearing with a small hole. A tailstock fits into the end of the ball bearing. The PEI (which looks like a little hat at this point) is mounted in the lathe under light pressure.

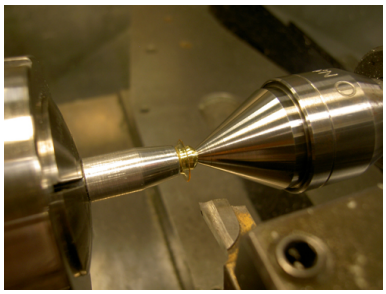

(d) The lathe spins on a slow speed, and the piece is nudged such the the "brim of the hat" lies in plane perpendicular to the lathe axis. This is done to ensure cylindrical symmetry of the coating, as the coating thickness varies with latitude across the hemisphere (due to stretching during thermoforming). Once aligned, the lathe is fully tightened and the piece is trimmed. First a cut goes inward on the lathe to remove the brim of the hat, and then the tool does a cutting pass outward so that no burr is left on the inner surface of the hemisphere. The outside edge of the cut is touched with a file to remove the exterior burr.

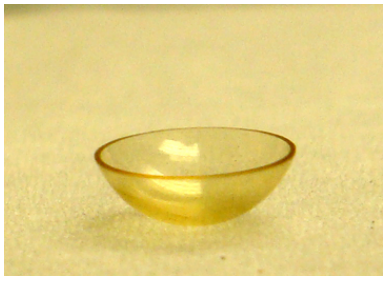

(e) The trimmed part should be 0.090" high. On the silicon lens, the bottom of the coating is high enough so that the coatings to not intersect with each other when seated adjacently in the POLARBEAR-I lenslet array, but the level is low enough to cover the optically active area of the lenslet (e.g.. beyond the angle of total internal reflection). The AR coatings are inspected one last time under the microscope to check for damage incurred during machining.

(f) Backing molds with a hemispherical cavity were made for adhering the AR coating onto the lens. To install the coating in the backing mold, a drop of rubber cement is applied. Then a clean, degreased AR coating is carefully placed into the mold.

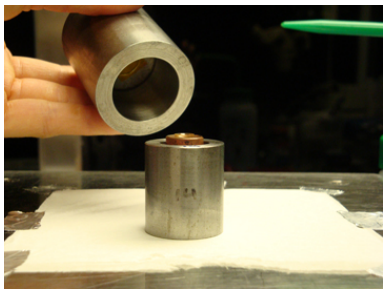

(g) For precise alignment, a paralleling weight is applied to the AR coating while the rubber cement dries and affixes the coating to the mold.

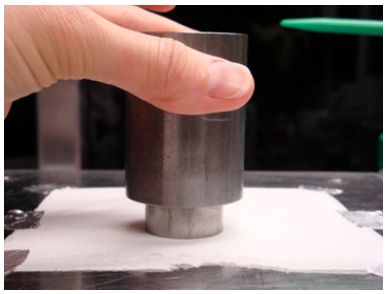

(h) The paralleling weight is lowered gently onto the AR coating. The trimmed edge of the AR coating now lies in a plane which is parallel to the lab bench.

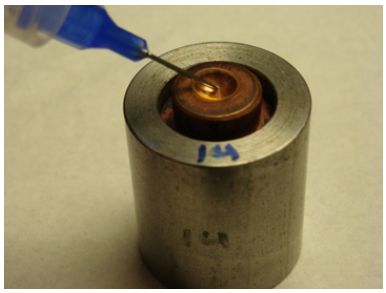

(i) Once rubber cement is dry, the edges of the AR coating are visually inspected. If excess rubber cement is found, it is removed with tweezers. Next, Stycast 1266 is deposited into the coating with a foot pedal actuated epoxy dispensing machine. The dispensed volume fills the space between the AR coating and the silicon hemisphere with enough excess that a generous fillet is formed around the coating edge.

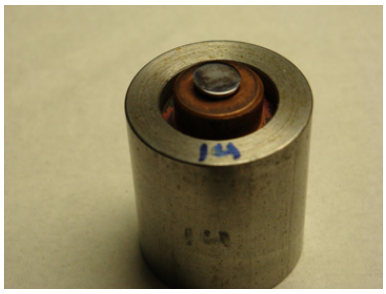

(j) A silicon hemisphere of measured and recorded height is degreased and placed into the AR coating and Stycast. To degrease the silicon, methanol on a kimwipe is used.

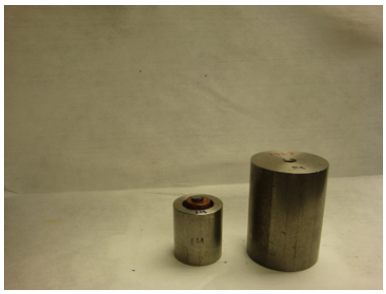

(k) The paralleling weight is used again to make the flat edge of the silicon hemisphere parallel to the lab bench surface and the trimmed PEI edge.

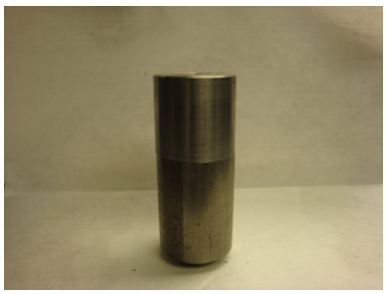

(l) The parallel weight and an extra weight are placed on top of the assembly. The total weight was selected so that the Stycast is squeezed out from between the AR coating and the hemisphere without leaving bubbles. The weight is light enough not to damage or deform the coating.

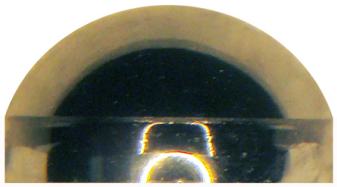

(m) After the epoxy has cured, the finished lenslet is removed from the mold.

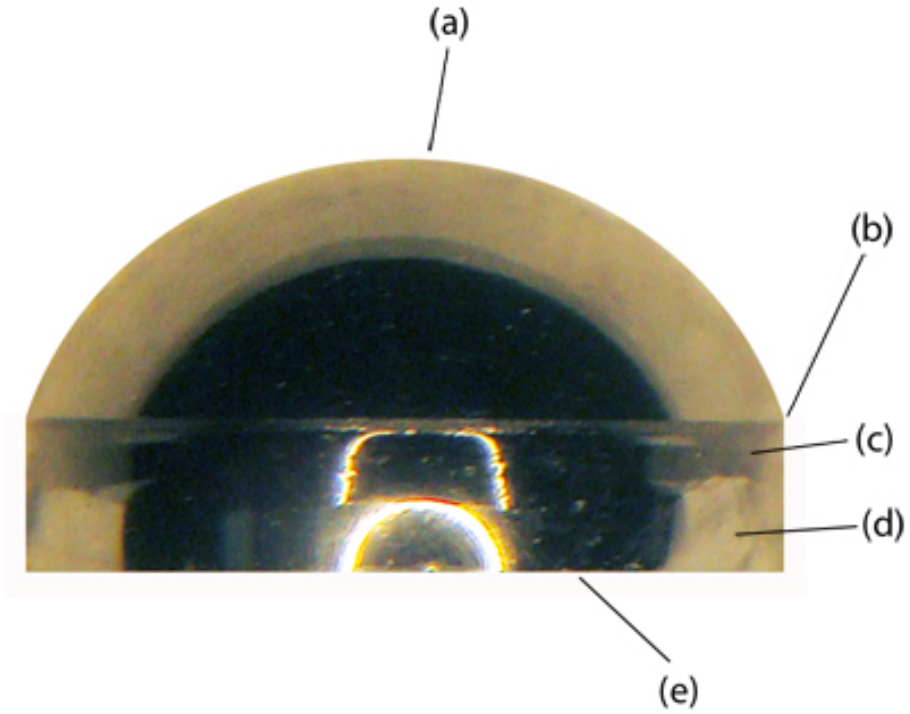

Figure 4.9: Lenslet with AR coating. Inspection points include (a) inspection of bubbles or particulates between the AR coating and the silicon surface, (b) the trimmed edge of the AR coating is in a plane parallel to (e) the bottom of the hemisphere, (c) the Stycast 1266 fillet is continuous around the hemisphere, and (d) the fillet stops so that bare silicon is exposed at the equator of the lens, enabling the correct fit into the silicon seating wafer.

Inspection Process

The finished lenslet is then inspected under a microscope. Figure 4.9 shows the lenslet as viewed edge on through the microscope, along with the landmark features to inspect. In the fabrication log, the height of the hemisphere is recorded before and after the AR coating is applied, and the key inspection points (as described in Figure 4.9) are checked:

- Aligned. The coating edge Figure 4.9(b) should be parallel to the bottom of the lenslet Figure 4.9(e).
- Fillet. The Stycast epoxy fillet Figure 4.9(c) should be continuous around the coating edge.

- Equator. The equator should be free of Stycast, so that bare silicon is exposed. This ensures that the lenslet will fit well into the lens seat. Figure 4.9(d)

The fabrication log lists defects associated with any lens. These defects can include items that disqualify a lenslet from being used in the focal plane array, e.g.. a dimple in the silicon, chipped silicon, scratches in the AR coating, or particulates glued between the AR coating and the silicon. Defects which do not disqualify a lenslet are mostly limited to discontinuous patches in the adhesion layer. A discontinuous patch is hard to see and may have a rainbow appearance due to reflections in a small cavity between the AR coating and the silicon. This discontinuity is of thickness $\ll \lambda$, usually at the north pole of the hemisphere, and less than 0.030" in diameter. These defects are allowed into the array as they are negligible thickness compared to a wavelength and do not compromise the adhesion under thermal cycling of the hemisphere, as evidenced by liquid nitrogen dunk tests, cryostat tests at 4 K, and thermal cycles to less than 1 K in the POLARBEAR-I cryostat.

Two aspects of the current process have largely rid us of the north pole discontinuity defect. The first was selecting an appropriate weight to put on the hemisphere during the epoxy cure. The second modification was accounting for shrinkage of the PEI by sizing the thermoforming mold a few thousandths of an inch larger.

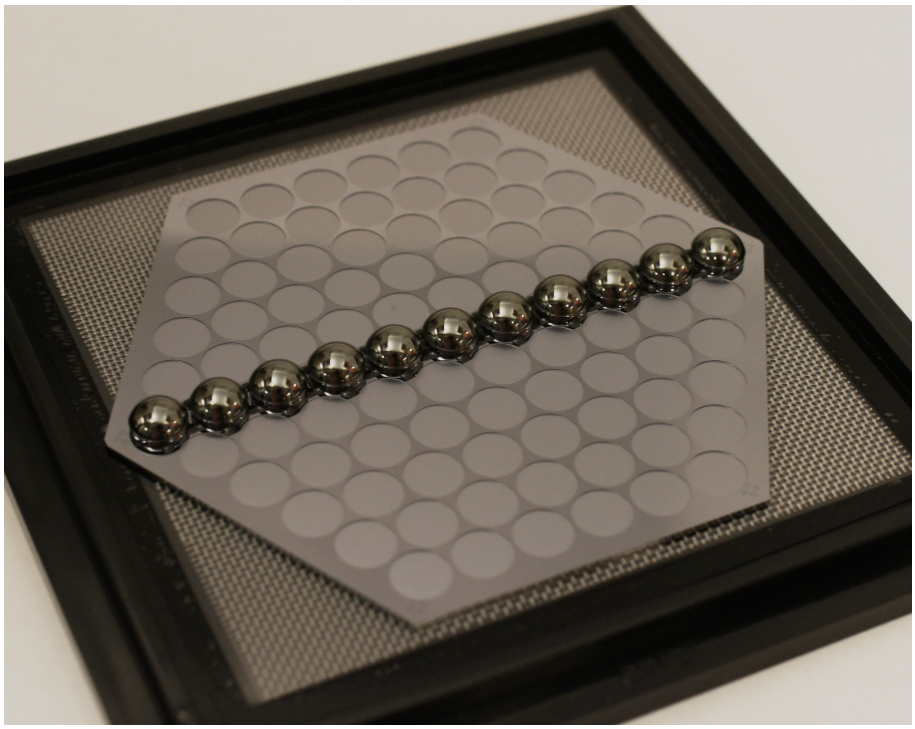

Figure 4.10: Lenslet Seating.

4.2.5 Seating Process

The AR coated lenslets are inserted in a seating wafer which locates them relative to each other. The lenslet is held in place with drops of Stycast 2850 on the edges, and degreasing is needed for adhesion at the edges. The bottom surface of the lenslet contacts the seating wafer and should also be clean of particulates. A methanol rinse with a kimwipe rub was used for this cleaning and degreasing.

The lenslets can be placed on the seating wafer with or without gloves, taking care to mostly touch the AR coating itself, not the silicon part of the lenslet. Upon seating, the lenslets will more or less click into place, but before glueing you should check the seating by pushing the lenslets side to side in the seat from a few directions. This is done by hand without gloves, as a rubber glove has too much friction and unseats the lenslet. One could also make a tool to accomplish this.

The array is populated in rows, as shown in Figure 4.10. One row is placed in the seats, the pixel number (Figure 4.11) of each lenslet is recorded in the fabrication log, and the seating wafer is taken to the microscope for deposition of Stycast 2850 dots around the perimeter of the lens. The epoxy drops are applied with a syringe and the epoxy dispensing machine. In order to not disturb the lenslet position while the epoxy cures, one row at a time is seated as shown in 4.12. After seating each row, the array is complete and ready for installation on the device wafer.

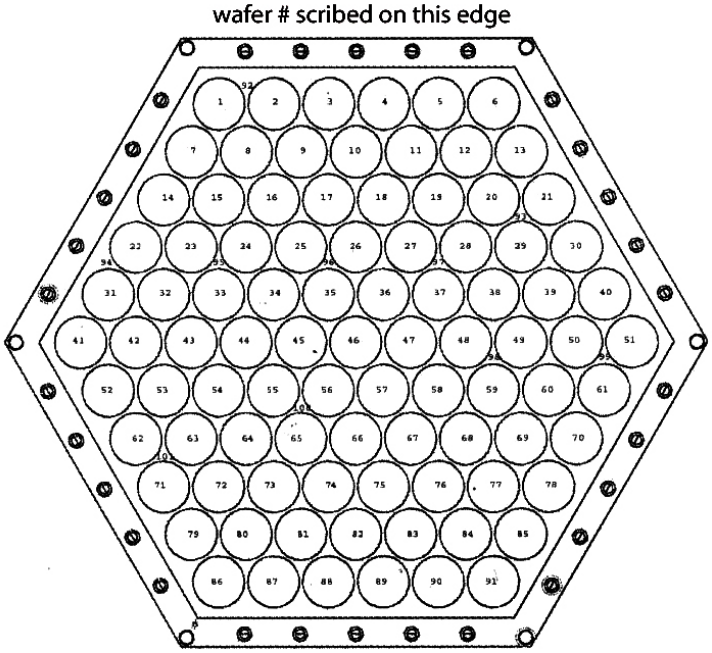

Figure 4.11: Pixel Numbering Diagram.

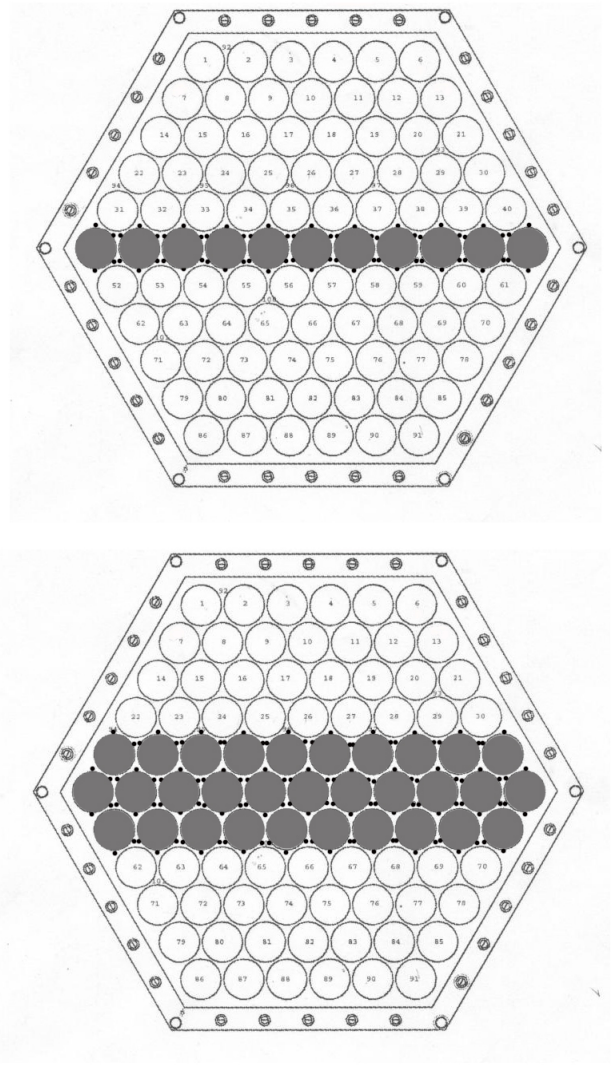

Figure 4.12: Lenslet Seating Diagram. Drops of Stycast 2850FT (represented by black dots) are deposited around each seated lenslet (grey circles). Rows are seated and cured individually to avoid accidentally unseating lenslets and disturbing uncured Stycast. The center row (top panel) is seated first, the rows are seated progressively outward (bottom panel). After the drops in the bottom panel cure, more rows can be populated. Once all of the lenslets are tacked down on one side by cured epoxy, difficult to reach positions between hemispheres can be filled in.

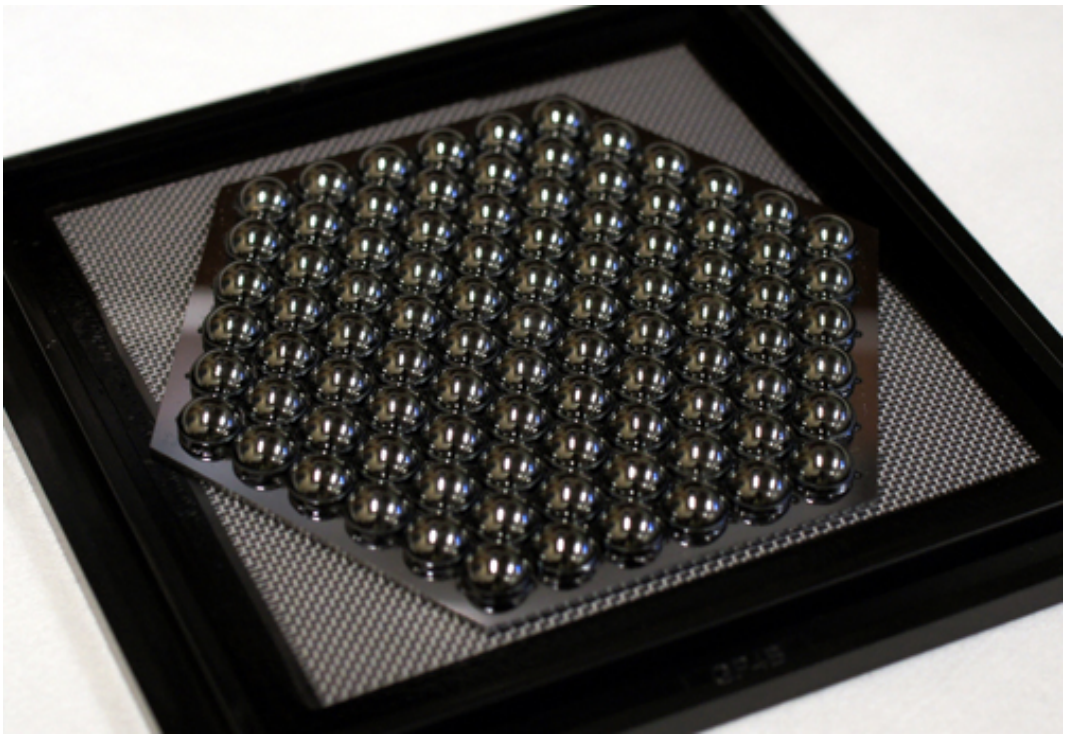

Figure 4.13: Completed Array.

4.3 Performance

To determine the efficiency of an AR coating, many techniques can be employed, including both simulation and measurement. A flat geometry is easier to study and the performance indicates the approximate effectiveness of the coating on curved surfaces. Curved geometry coatings can be simulated and optically tested as well.

4.3.1 Flat Anti-Reflection Coating

In addition to measuring transmittance properties of the individual materials used for the POLARBEAR-I focal plane, the AR coating used was tested on a flat geometry. A flat geometry was easily tested in our open air Michaelson Fourier Transform Spectrometer. The spectrometer has a flat beam front, so the transmittance was calculated as a sample-in sample-out ratio; the transmitted power with the alumina sample in was divided by the power with an open aperture (no sample in), yielding the fractional transmittance across the frequency range.

The fabricated test coating and transmittance results are shown in Figure 4.14, where the pass band is centered at 135 GHz. Using the thickness of this coating, the optical index of PEI can be calculated (see Appendix A.1). As previously discussed, the POLARBEAR-I AR coatings are thermoformed, and the thermoforming process stretches the coating to a thinner gauge. Thus, the measured flat geometry transmittance has a thicker AR coating than the POLARBEAR-I band, shifting the band to larger wavelengths (lower frequency). Adjusted for thickness, the equivalent pass band used on the POLARBEAR-I focal plane is 155 GHz.

4.3.2 Anti-Reflection Coating on a Lenslet

The AR coating in its final application, on the lenslet surface, is clearly of primary importance. Validation of the AR coating on the curved lenslet is more difficult than on the flat geometry. On a curved surface, there is additional complication due to geometry of the rays and diffraction at the coating surface.

When the diffraction is a factor, simulation can be done with a full-wave EM simulator such as Ansoft HFSS. When this project began, attempts to simulate the antenna beam were hampered by RAM constraints of our analysis computers. It was a milestone when a quarter of a lens could be simulated, and only then with a lenslet size smaller than the POLARBEAR-I lenslet compared to the wavelength. We were not able to simulate AR coatings or variations in AR coating from the ideal case due to the meshing requirements at the interface. Thus, our initial design principle was thus to make the coating "as well as possible". Fortunately, the intervening years in computing have allowed us to simulate the lenslet, so analysis of the finished product can be accomplished retroactively. This analysis is currently in progress.

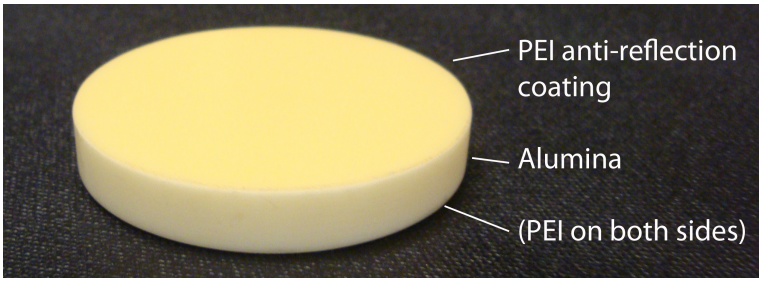

(a) Anti-reflection coating sample

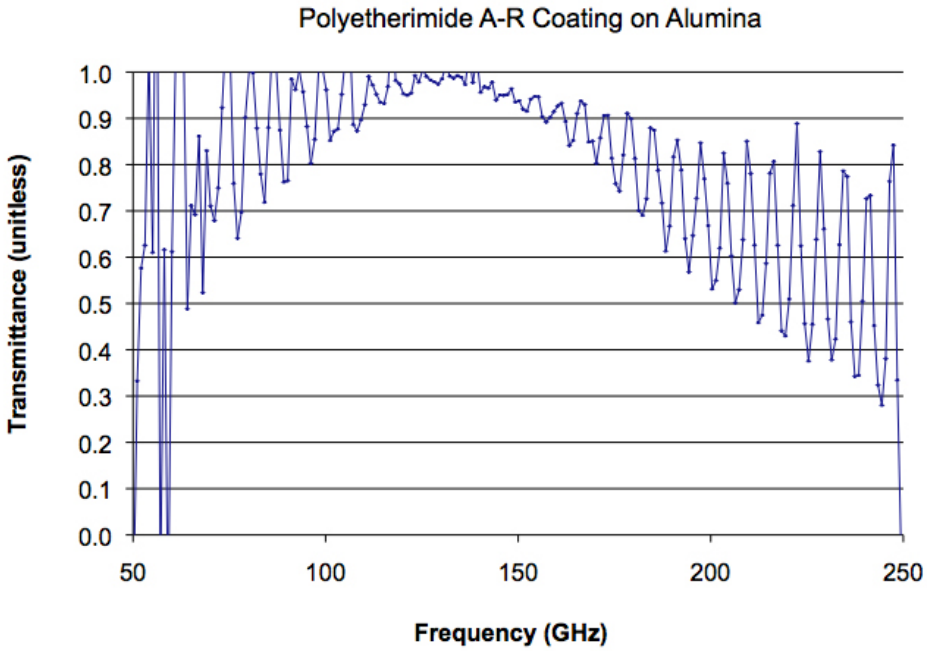

(b) Spectroscopy

Figure 4.14: Quarter Wavelength PEI Coating. (a) Polyetherimide was adhered to both sides of an alumina slab with Stycast 1266 using pressure. This method is the flat geometry equivalent to the POLARBEAR-I AR coatings. (b) The transmittance through the alumina shows oscillations due to interference of internal reflections. These reflections disappear at 135 GHz, where the AR coating functions. The AR coating functions here at a lower frequency than the POLARBEAR-I pass band due to differences in the thickness of the AR coating material.

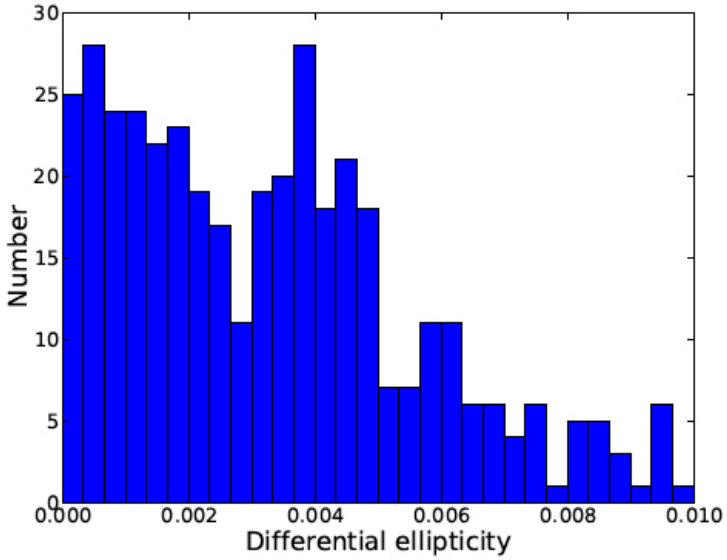

Figure 4.15: Differential Ellipticity Statistics. Taken on the sky in Chile, this is a histogram of differential ellipticity at each pixel.

Optical characterization of the AR coating in situ on the lenslet is also no small feat. To test this AR coating for use with the POLARBEAR-I beams, the POLARBEAR-I antenna coupled bolometer, readout, a suitable cryostat, beam mapping source, and understanding of the test system optical efficiencies were required. A combination of lab measurements and beam maps through the telescope indicate good performance of the coatings. Statistics of differential ellipticity taken on the sky in Chile are shown in Figure 4.15. Note that ellipticity in general can involve the rest of the optical chain, including reflection off of the telescope mirrors (a main source of ellipticity). The relevant metric for AR coatings functioning is thus differential ellipticity, the difference in ellipticity at the pixel level.

The level of differential ellipticity determines what level of tensor to scalar ratio one can observe. For POLARBEAR-I to reach T/S ~ 0.025 at 2σ, the differential ellipticity should be $e < 3\%$, so our AR coatings are functioning well below that limit. This systematic error analysis, by Meir Shimon at UC San Diego, was based on [83] and assumes Gaussian beams with a perfect scanning strategy. The combined effects of differential ellipticity and differential pointing were also considered. The contribution to B-mode signal by differential ellipticity is shown for a 5 arcminute beam in Figure 4.16.

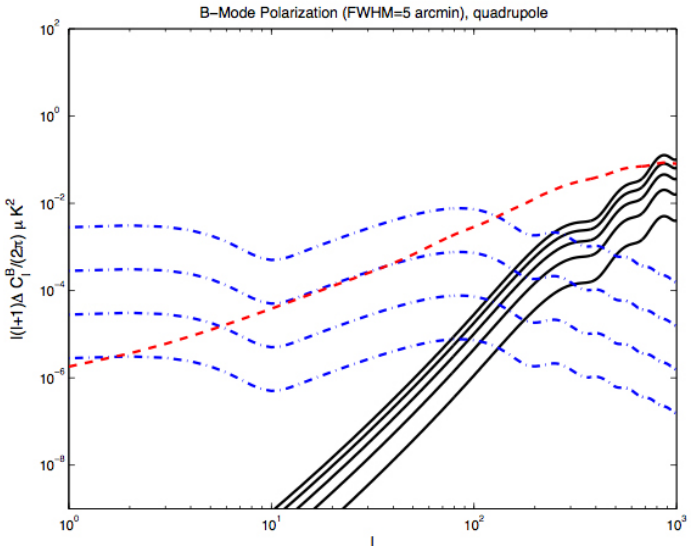

Figure 4.16: The contribution of the differential beam ellipticity ("quadrupole" effect) to the B-mode power spectrum (5 arcminute average beamwidth). The values shown should be multiplied by $s^2{}_\psi$ (see Table III of [83]). Shown are the effects for e = 0.01, 0.02, 0.03, 0.04 and 0.05. For comparison, the dot-dashed curves refer to the contribution from primordial gravitational waves with tensor to scalar ratios T/S = 10^{-1}, 10^{-2}, 10^{-3} and 10^{-4}. The dashed curve is the B-mode polarization produced by gravitational lensing by the large scale structure. Caption and figure from [83].

Figure 5.1: POLARBEAR-I on the Huan Tran Telescope at the Cedar Flat engineering site. The telescope was seated on a foundation pad borrowed from the CARMA array, which can be seen in the background. Photo credit: Huan Tran

Chapter 5

POLARBEAR-I Results and Status

POLARBEAR-I completed its engineering in Cedar Flat, California, and has moved to its science observation site on in the Atacama desert on the Chajnantor Plateau. The results and status are discussed below. Absent from this discussion is the significant receiver testing that was done in the laboratory before both of these field campaigns. The laboratory tests are included in the dissertations of Kam Arnold [4] and Zigmund Kermish [46]. The latter also includes a detailed account of the field work until the summer of 2012.

Figure 5.2: POLARBEAR-I on the Chajnantor Plateau, Chile.

5.1 Cedar Flat Engineering Run

The engineering run was in the spring of 2010. By summer of that year, the engineering run goals were accomplished and POLARBEAR-I received funding to commence the science observations.

The Cedar Flat site was selected due to its proximity to UC Berkeley, relatively favorable observing conditions, and collaborative potential with the CARMA group. The site at Cedar Flat had infrastructure and a history of millimeter wave research by the CARMA team. [16] CARMA is an interferometer, and the telescope positions are changed periodically to adjust the interferometer resolution for various measurements. POLARBEAR-I was hosted at the CARMA site on one of the telescope pads which was not in use by the configuration at the time.

The requirements met for the engineering run performance review included:

- Telescope operation: scans with azimuthal speed of $4^\circ/s$ and azimuthal acceleration of $2^\circ/s^2$
- Pointing reconstruction to an accuracy 1/3 of the $4'$ beam size
- Diffraction-limited beam performance across the array
- Stepped half-wave plate operation with >90% polarization efficiency
- Operation of two focal plane modules (each with 182 optical bolometers)
- Noise Equivalent Temperature for a pixel of $NET_{\mathrm{CMB}} \sim 1mK$
- Intensity and polarization maps of unpolarized and polarized sources (for which planet maps and Tau-A were used respectively)

5.2 Chilean Deployment

After the engineering run, the telescope was dismantled and shipped to Chile. Meanwhile, the receiver returned to Berkeley for upgrades including installation of a complete set of seven focal plane modules. At the Chilean site, the telescope was rebuilt and debugged.

The receiver was installed on the telescope in late 2011, and the first few months of 2012 were spent troubleshooting the integrated system. Science data has been collected regularly since April of 2012. The results shown here have been presented in [46] and [45].

Major accomplishments of the recent months in Chile include:

- Optical detector yield of $\sim 70\%$ at a given time. This efficiency is approaching the possible yield of 85%, based on cold laboratory measurements. The maximum yield is dictated defects in detector fabrication. Our current lower yield is mostly attributed to individual bolometers becoming fixed in a superconducting state. When one bolometer latches superconducting, the SQUID biasing is effected and the whole multiplexed comb is taken down. See 5.3(a) for a representation of the live pixel beam maps.

- Acceptable levels of beam ellipticity, differential ellipticity, and differential pointing. Figure 5.4 shows the statistics of these quantities for the live pixels in Chile.

- Maps of astronomical sources. The beams maps in 5.3 were taken using Saturn. The polarized source Tau-A has also been measured along with preliminary scans of the galaxy and preliminary scans of the target observation patches. Figures 5.5 and Figure 5.6 show Tau-A and a section of the Milky Way Galaxy. Both of these observations are in agreement with measurements already in the literature.

- Observation patch scans. We've begun making maps of CMB temperature fluctuations which can be detected in several hours of observation.

POLARBEAR-I will continue observations of the target science patches, reaching the integration depth discussed in Section 2.1.7 in 2014.

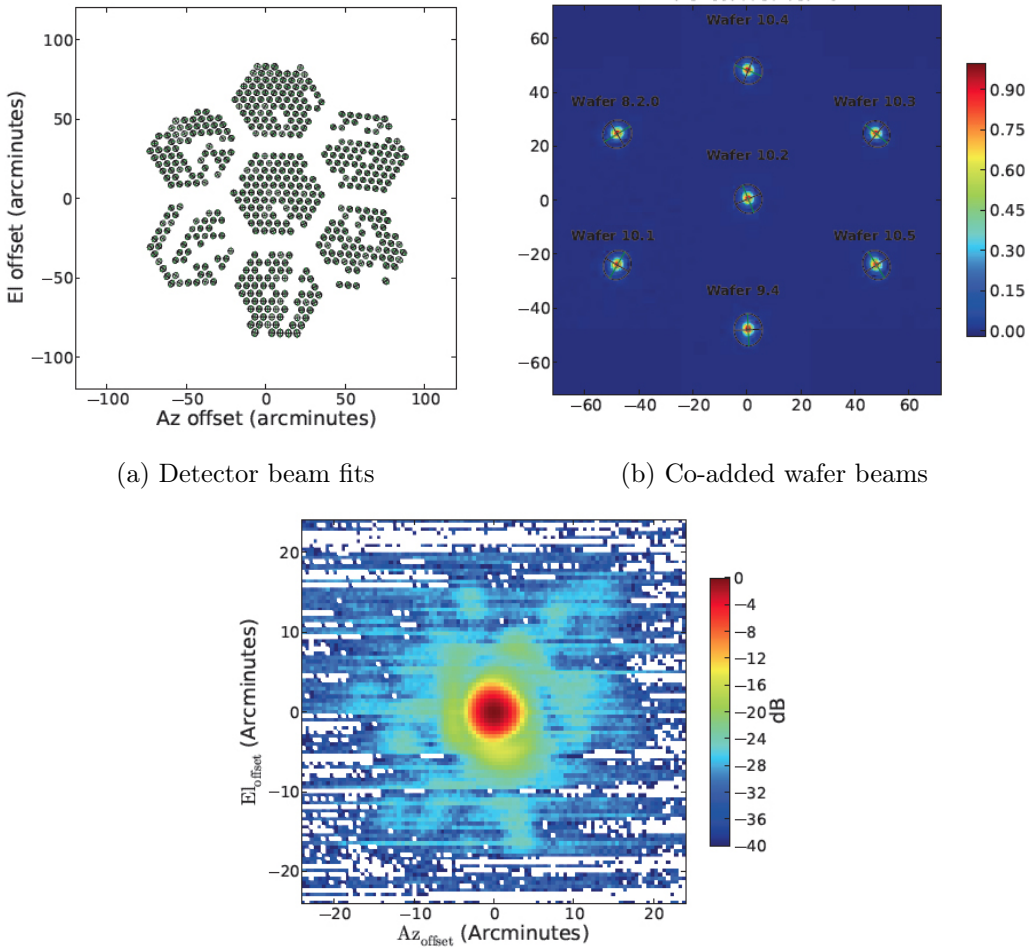

(a) Detector beam fits

(b) Co-added wafer beams

(c) Co-added focal plane beam

Figure 5.3: POLARBEAR-I beam maps from the Chajnantor Plateau. Beam maps were generated with observations of Saturn, which is $\sim 15''$ in diameter and much smaller than the $4'$ POLARBEAR-I beams. (a) Shows gaussian fits to the individual detector beam maps. The relative sky position of the pixels is illustrated here. There are obvious voids in the pattern of each hexagonal focal plane module, representing non-functional detectors. The space between focal plane modules accurately reflects the space needed for mounting hardware at the edge of each module. (b) Each module can be co-added to create an effective beam pattern for the module and its associated detector wafer. Here, the best fit Gaussian is exaggerated by a factor of four and over-plotted as crosshairs on each beam. This illustrates the changes in ellipticity orientation across the focal plane. (c) Finally, the detector beams may all be co-added for a whole instrument beam pattern. A logarithmic scale is used to display the sidelobe pattern.

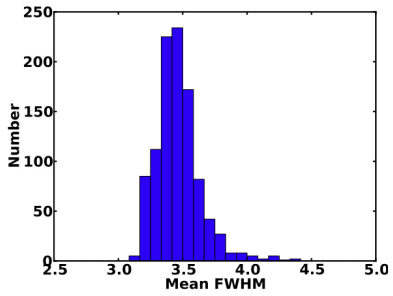

(a) Beam size histogram

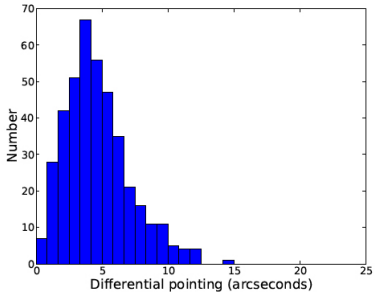

(b) Differential pointing histogram

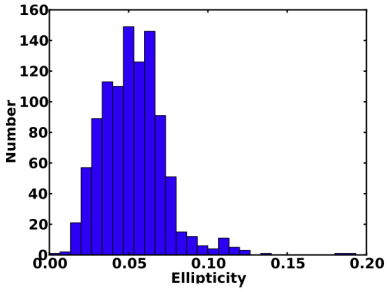

(c) Ellipticity histogram

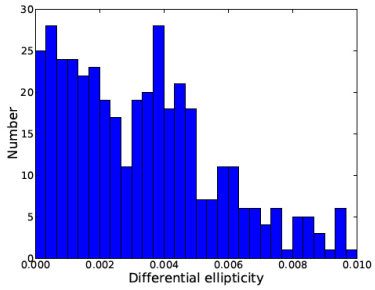

(d) Differential ellipticity histogram

Figure 5.4: POLARBEAR-I Beam Statistics. The beam statistics collected in Chile show levels of systematic error within the specifications for our target sensitivity.

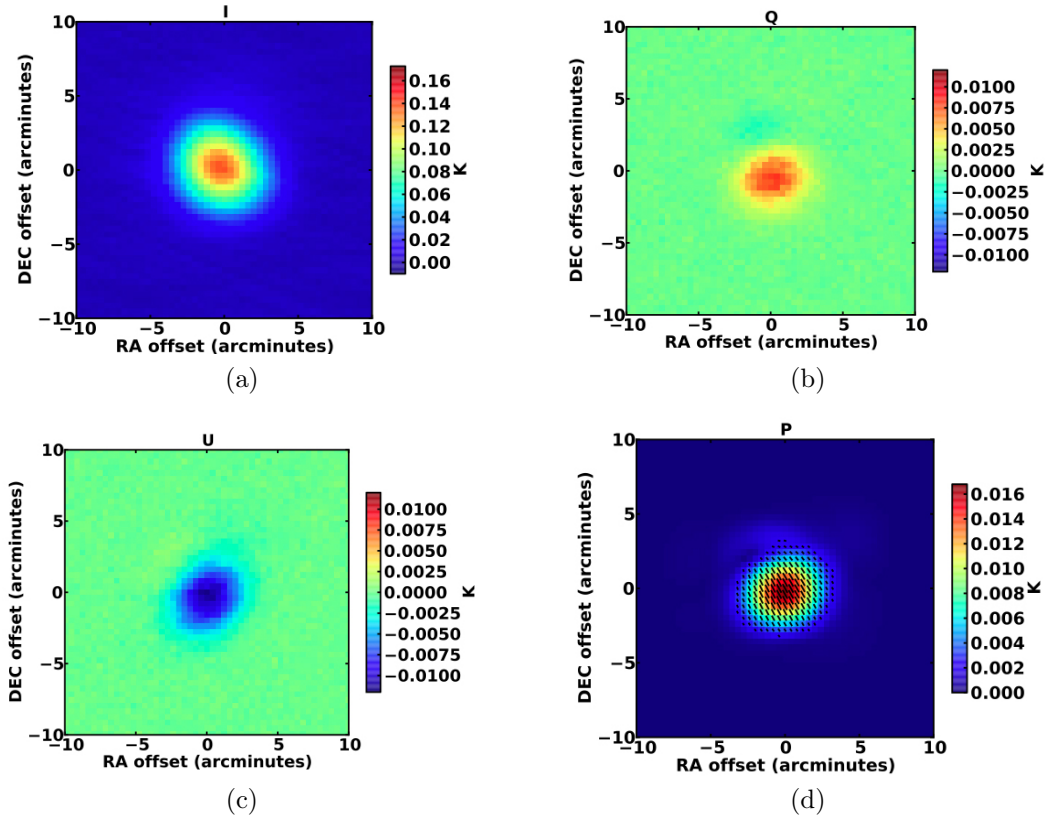

Figure 5.5: POLARBEAR-I Tau A maps. The Stokes parameters (a) Intensity, (b) Q, and (c) U are plotted. (d) The Stokes parameter maps are combined to find a polarization $P = \sqrt{Q + U}$ and polarization angle. The measured polarization is in agreement with the polarization measured by XPOL on the IRAM telescope at 90 GHz. (Characterization of Tau A, the Crab Nebula, is presented in [6])

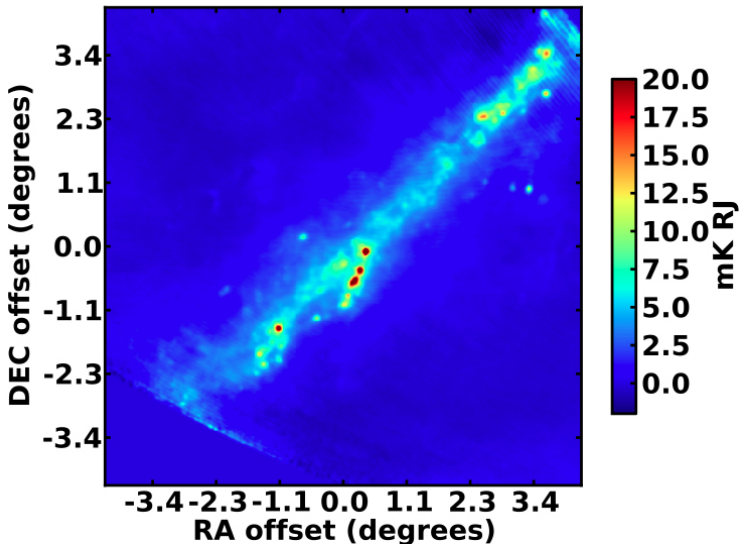

Figure 5.6: POLARBEAR-I preliminary galaxy scan. This scan, using approximately an hour of data, shows a section of data through the middle of the galaxy. Bright features within the galactic plane are in rough agreement with features recorded by WMAP.

Chapter 6

Broadband Detector Technology

The future application of broadband antenna coupled detectors for CMB measurement was discussed in Section 2.2. This chapter gives details about the technology used for these detectors. The broadband antenna is briefly discussed, and the bulk of the chapter concerns development and current status of anti-reflection coatings. These coatings enable broadband measurements with high signal and low instrumental polarization.

6.1 Coupling to a Broadband Antenna

The POLARBEAR-I antenna has dimensions tuned to a wavelength at the center of its band reception. For multichroic pixels, we need an antenna with a wider bandwidth. A dual-polarization sinuous antenna is being developed for this use by a UC Berkeley/UC San Diego collaboration. The antenna shows good beam properties over two octaves in bandwidth. [66] [68] [86] The POLARBEAR-I -style antenna and sinuous antenna are shown in Figure 6.1. The figure allows visual comparison of the antenna and filter scheme for single and multi-channel measurements.

The sinuous antenna can be thought of as a series of dipole antennas. The electrically active arms of the antenna are related to the incoming frequency, so the active region of the antenna moves with frequency. The active area of the antenna should be sufficiently far from the large and small end of the antenna arms in order to avoid resonances. Roger O'Brient's thesis discusses details of the development of this antenna along with the band defining microstrip filter parameters. [69]

The sinuous antenna with a diplexer circuit with 150 and 220 GHz channels is currently planned for use in POLARBEAR-II .

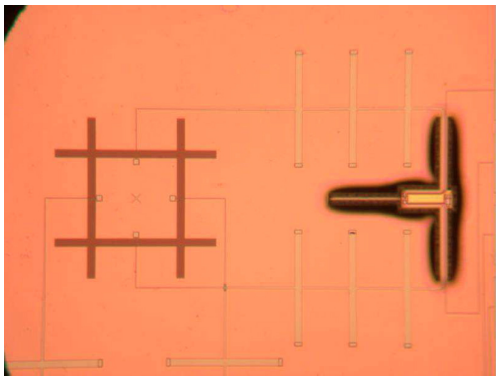

(a) Single Band Antenna

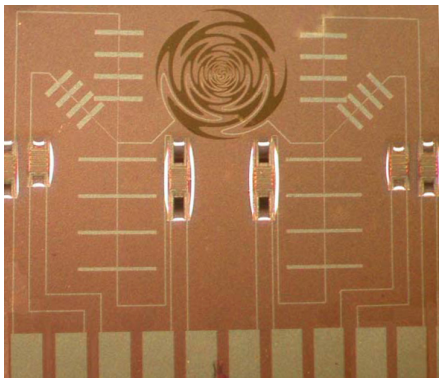

(b) Broadband Antenna

Figure 6.1: Antenna Geometries. (a) The POLARBEAR-I double slot dipole antenna is at left of the image. To the right of the antenna the golden vertical segments are band-defining microstrip filters. To the right of the filter is the released TES bolometer, where the release can be seen in black. Each parallel pair of antenna arms couples to one linear polarization. The detector from one polarization is visible in the image. (b) A broadband sinuous antenna is in the upper center of the image. The antenna is attached to triplexer filters, which read out three bands from each of the polarizations of the antenna. The filters of this antenna are three sizes of microstrip stubs, to scale with wavelength. Each filter is attached to a TES detector. The TES release structure is white in this image, and six bolometers can be seen. Each bolometer is attached to a set of read out pads at the bottom of the picture. Images courtesy of Roger O'Brient[69].

6.2 Broadband Anti-Reflection Coating Principles

Elements in the optical chain will require anti-reflection coatings over the observation bandwidth. The author's work has been primarily concerned with the development of these coatings for the antenna's contacting lenslet. Thermal contraction is an issue as the lenslet is part of the milliKelvin focal plane. The high curvature surface of the lenslet surface is a consideration for the fabrication process. The AR coatings developed for a high curvature surface will also work on flat or low curvature surfaces of optical elements such as re-imaging lenses and half-wave plates.

6.2.1 AR Coating Geometry Overview

A broadband AR coating will provide a less abrupt transition between vacuum and the high dielectric optical element. Two methods can be used to achieve this change in index, referred to here as the *geometrical* and *gradient* methods. Shown in Figure 6.2(a), the geometrical method uses a high dielectric constant with a profile cut into it. The percentage of high dielectric material in a horizontal cross section is a function of

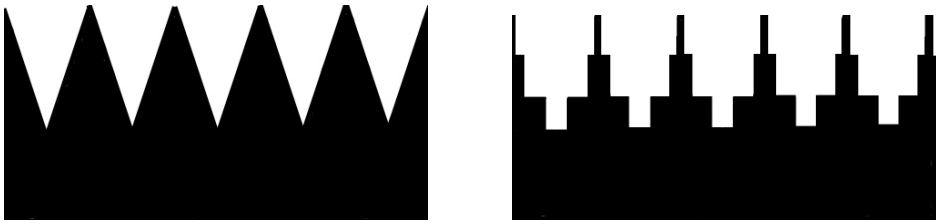

(a) Geometrical AR coating

(b) Discrete geometrical AR coating

(c) Gradient AR coating

(d) Discrete gradient AR coating

Figure 6.2: Anti-Reflection Coating Geometries. The (a) geometrical method and (c) gradient method of making an AR coating are shown here. The dark areas correspond to high dielectric constant, whereas the light areas represent low dielectric constant. Both methods of AR coating can be made in discrete steps, and three steps are shown in (b) and (d) respectively. The index profiles shown are for illustrative purposes, and do not directly represent an idealized function of index vs. thickness through the coating. For an ideal coating, the higher index layers will be thinner than the low index layers, as seen in (d).

height in the coating. The effective index, which is roughly a volume-weighted average of the high dielectric and vacuum, changes monotonically with distance through the coating. The gradient method, Figure 6.2(b), is a solid coating, also with the property that the index increases monotonically from low to high.

An approximation to both methods uses steps in index to achieve the gradient. In the case of the geometrical coating, the profile of the removed material might be discrete instead of continuous, Figure 6.2(b). In the case of the gradient method, discrete layers (each with a constant optical index) are applied, see Figure 6.2(d). Both figures show three discrete steps, but any number of steps can be used. If more steps are used, the index change is more gradual, and the resultant AR coating has a higher frequency bandwidth.

The impedance matching between the vacuum and high dielectric optical element is similar to electrical impedance matching. The ideal impedance vs. distance profile for impedance matching has been studied for microstrip transmission lines. The same impedance profiles can be used for an optical index match. Transmission line theory is presented in textbooks, for example Pozar's textbook [73].

Control over the profile will not be perfect due to fabrication defects, including both thickness and index control. Further, in the discrete step cases, the index will

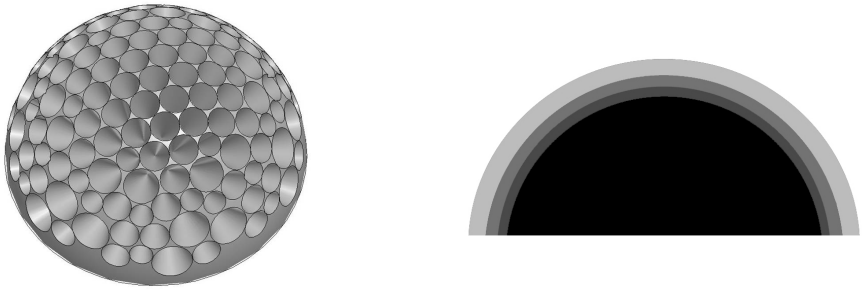

(a) Geometrical: Conical Holes (b) Gradient: Layers

Figure 6.3: Anti-reflection coating types on a hemisphere. (a) The geometrical method can be made, for example, by conical holes. (b) The gradient method can be made by nested layers.

not have the smooth impedance profile of a lithographed transmission line. In the discrete step AR coatings, a series of quarter-wavelength coatings can be used. Recall that a quarter-wavelength AR coating, between indices n_i and n_f has index

$$n_{AR} = \sqrt{n_i n_f} \tag{6.1}$$

and a thickness

$$t = \frac{\lambda_{center}}{4 n_{AR}} \tag{6.2}$$

If each step is the geometrical mean of the surrounding steps, and the thickness is a quarter of the effective central wavelength, the AR coating will function well.

The goal is to apply the broadband coating to the hemispherical lenslet surface. Figure 6.3 shows example schematics of the geometrical and gradient type coatings on a hemispherical surface.

6.2.2 AR Coating: Geometrical Method

In the geometrical method, the aspect ratio of surface features is set by the bandwidth of the desired AR coating. For a gradual index transition, the coating thickness should be comparable or larger than the longest wavelength in the pass band. To avoid diffraction, the shortest wavelength in the pass band determines the maximum spacing of features. Separation between grooves or pyramids should be at most a fraction of the shortest wavelength to avoid diffraction at the surface of the AR coating. [21] [36] Together these criterion require high aspect ratio pyramids for a wide bandwidth coating.

High aspect ratio features are problematic from a fabrication standpoint, as tall thin features are delicate and difficult to produce. For a coating spanning 90-220 GHz, the transition thickness is ~ 3 mm. At Berkeley, we attempted machining high

aspect ratio (1:4 spacing:depth) features using both a tapered cutting wheel and a conical reamer. The attempted profiles were continuous, similar to Figure 6.2(a). This machining was attempted in Rexolite, TMM, and UHMWPE. We found that for tapered cutting tools, the amount of force generated perpendicular to the material is too much. Pyramidal grooves (or the pillar left between conical holes) would break off for brittle materials, such as TMM and Rexolite. For soft materials, such as UHMWPE, as the remaining material got thin, pressure from the cutting tool would cause the material to deflect and a clean cut could not be made.

These trails lead us to believe that a stepped profile, as shown in Figure 6.2(b), will be the feasible way to machine high aspect ratio AR coatings. Lateral stress on thin, fragile features can be avoided by making wide shallow cuts first (corresponding to the top layer of Figure 6.2(b)) and then progressing to the deeper cuts. In fact, a two step geometrical AR coating has been demonstrated on silicon with an abrasive cutting wheel[1]. The physics machine shop UC Berkeley is currently investigating this method.

Laser cutting, electrical discharge machining (EDM), and ultrasonic drilling have also been briefly investigated by the Berkeley team. Laser was deemed too expensive and time consuming, circa 2005.

EDM was also investigated in the mid 2000s. EDM relies on a conductive material for oblation. Unfortunately, the materials we use for optical transmittance should not be conductive. It is possible to use a material, such as silicon, which is doped at the correct level to have some conductivity at room temperature and little to no conductivity at cold temperatures. Given the market for silicon ordered to specification, this seems prohibitively expensive for the material cost alone. The cost and total machining time could also be prohibitive. We did communicate with Professor Eberhard Bamberg, University of Utah, whose group is developing technology to EDM low conductivity materials.

Ultrasonic drilling has the ability to make high aspect ratio features on a brittle material such as silicon. We had samples made on a flat geometry by Sonic-Mill[2]. Results were good, however ultrasonic drilling (where particles are bombarded in a single direction at the machining surface) was deemed infeasible on a curved geometry.

6.2.3 AR Coating: Gradient Method

The gradient method of Figure 6.2(d) relies on having a range of various dielectric constants deposited in layers. On a hemispherical surface, this can be accomplished by machining or molding.

The coating will be simpler to fabricate if fewer layers are used. However, the bandwidth of the coating increases with the layer count. The matrix formalism shown

[1]Jeff McMahon, University of Michigan, private communication

[2]Sonic-Mill, Albuquerque, NM, http://www.sonicmill.com/

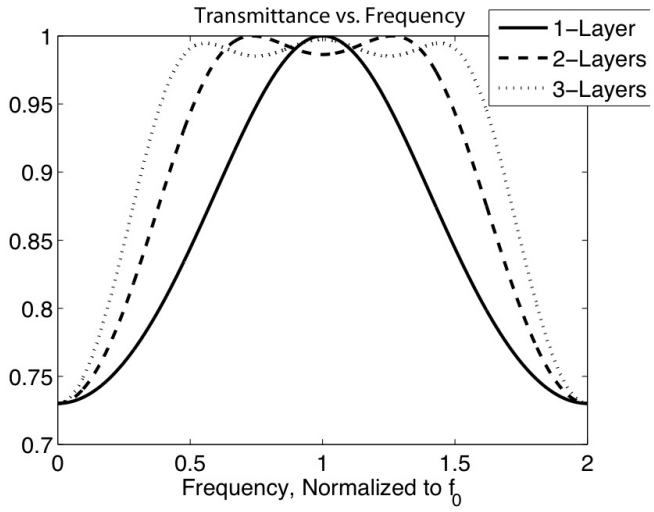

Figure 6.4: Multi-layer Anti-Reflection Coating Transmittance. Transmittance on a high dielectric AR coating is shown for 1, 2, and 3 layer coatings. The coatings are simulated between vacuum and high dielectric of $\epsilon = 10$. All layers have a thickness $t = \frac{\lambda}{4n_{layer}}$. The coating dielectrics are: Single layer $\epsilon = \sqrt{10}$, two-layer $\epsilon = 2, 5$, and three-layer $\epsilon = 2, 4, 7$. The bandwidth increases with the number of layers. Figure credit: Aritoki Suzuki

in Equation 4.4 can be used to compute the transmittance through a multi-layer coating. Figure 6.4 shows a two- and three-layer coating compared to a single quarter-wavelength coating. As shown, more layers result in a wider bandwidth.

Compared to the geometrical method, the gradient method is attractive as it lacks fragile features. Molding or machining can be used to fabricate the AR coating layers. Molded layers are particularly attractive as that scheme allows us to fabricate the AR coatings in-house once the molds are made. Keeping the job in-house allows a high level of control over quality, timeline, ease of communication, and low cost. In the author's opinion, these benefits outweigh the drawback of the associated manual labor.

We have made multi-layer AR coatings out of commercially available materials. We are also working on developing tunable dielectrics by mixing our own dopants into epoxy. Coatings using commercially available TMM and epoxy coatings are discussed below.

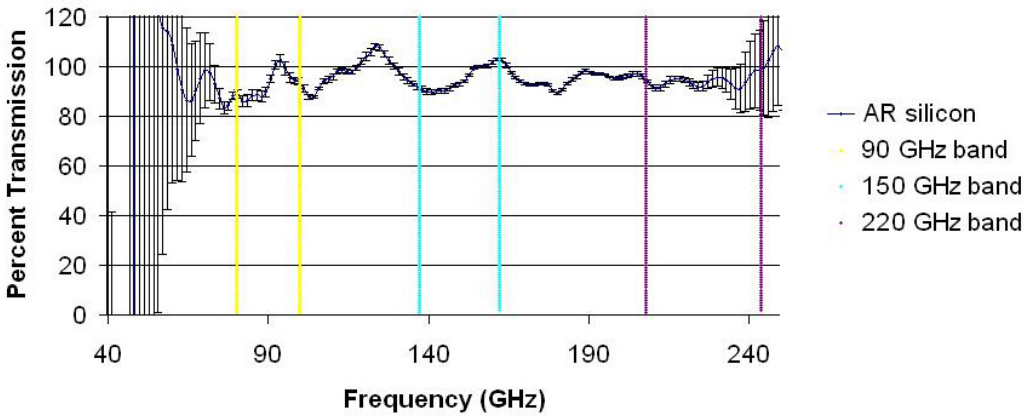

Figure 6.5: AR Coating on Silicon. Three layers of TMM and one layer of expanded teflon were used for this coating. The coating was applied to two sides of silicon, and the resultant transmittance has a band averaged reflection of 3% per side, as opposed to 30% per side for bare silicon. Statistical error bars are over-plotted on the data. Systematic errors are attributed to couplings in the lightpipe optical path, accounting for spurious signal in excess of 100% transmittance.

6.3 Fabricated Broadband AR Coatings

6.3.1 Rogers TMM

TMM is a circuit board dielectric manufactured by Rogers Corp[3]. The material is a thermoset polymer with ceramic dopants to tune the indices.[76] The manufactured materials are TMM3, TMM4, TMM6, TMM10, TMM10i, where the series number corresponds to the approximate dielectric constant. The 10 series has two dopant options; TMM10 is birefringent (due to asymmetric dopant grains), whereas TMM10i is isotropic.

Off the shelf, TMM comes in rigid sheets and lends itself to use for flat AR coatings. The composition of TMM renders it a unique material to deal with from a machining standpoint, as it has characteristics of both a polymer and a ceramic. We found that thermoset TMM could generally be ground and cut as a ceramic.

An AR coating for silicon on a flat geometry was made with TMM, as seen in Figure 6.5. This coating used TMM3, 6, and 10i with a low index layer of Zitex (expanded teflon). Layers were hand ground using a custom sanding jig to ensure parallel faces to a fraction of a thousandth of an inch.

Due to commercial availability and the promising results of the flat AR coating, we investigated the use of TMM for application to curved surfaces. To do this, we received a proprietary, non-commercially available form of un-thermoset TMM

[3]Rogers Corp., Rogers, CT, http://www.rogerscorp.com

from the R&D department. The material had the texture of a crumbly rubber. We tried dissolving the polymer in a solvent, and then dipping or applying a paste which was later machined into an AR coating of appropriate thickness. We also tried molding. In both cases, the material was thermoset after application. Although we had some success, see for example [69], the material seems difficult to work with in the production setting.

In order to scale the multichroic array to thousands of pixels, we need a robust AR coating with high fabrication yield. This led us to using off the shelf epoxies and exploring custom doping these epoxies for a tunable index.

6.3.2 Epoxy-based AR Coatings

To manufacture a stepped gradient AR coating, one must find (or create) materials with acceptable dielectric constant and be able to adhere them repeatably to the lenslet. Epoxy naturally lends itself to this task. We have produced a two-layer coating, and wider bandwidth coatings are in development.

Molding layers of epoxy onto a lens has advantages over other methods we tried, including:

- Moldable: We only have to machine and validate the mold shape once, then we can use the mold many times.
- Epoxy is a natural binding agent for added dopants. By adding dopants to epoxy, we can in principle create a full range of selectable index values. High dielectrics can be added for increased index, and evacuated glass spheres can be added to reduce the index.
- Mechanical and thermal cycling robustness. Epoxies are designed for adhesion, so no intermediate adhesion layers are needed between layers. Two-layer epoxy coatings have been thermal cycled successfully to 77 Kelvin.
- In-house fabrication. The ability to create a range of indices and mold them allows us to fabricate in-house. This removes uncertainty about timelines and quality control and reduces cost.

Molding/Fabrication

To fabricate an epoxy-based coating on a hemisphere, we designed molds to hold the hemisphere at the center of a larger hemispherical cavity. Figure 6.6 shows a design sketch and fabricated mold. To form a layer of thickness t_{layer}, the hemispherical cavity has a radius $R = R_{hemisphere} + t_{layer}$. The hemisphere is positioned by a seat which mates to the rest of the mold via a slip fit sleeve. The mold was made in the UC Berkeley Physics machine shop.

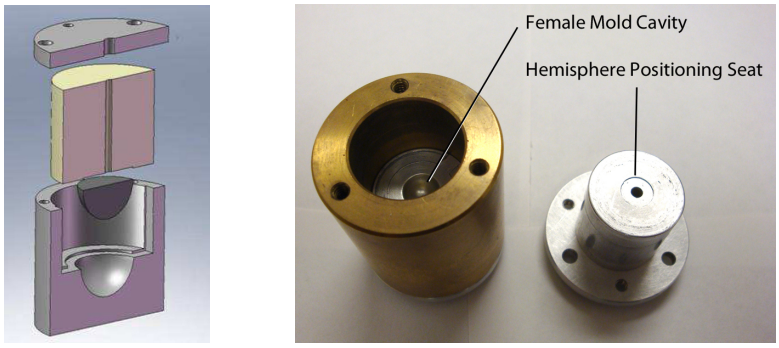

(a) Bisected Mold (b) Machined Mold

Figure 6.6: Multi-layer Coating Mold. (a) The mold for one layer of coating is shown in an expanded bisection sketch. The hemisphere is also shown in this sketch. (b) The two part finished mold. The hemisphere mounting piece slip fits into the brass sleeve which holds the molding cavity. This slip fit aligns the hemisphere to the molding cavity. Also pictured, a small hole traverses the length of the hemisphere mounting sleeve. A dowel pin can be inserted into the hole to remove the hemisphere if needed.

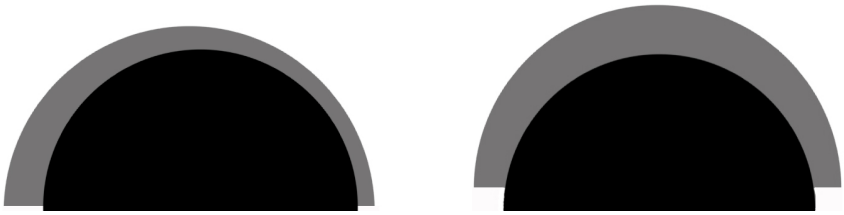

(a) Horizontal mold offset (b) Vertical mold offset

Figure 6.7: Molding defects. Misalignment of the hemisphere and mold cavity in (a) the horizontal direction and (b) the vertical direction cause errors in the layer thickness.

The layer is formed by depositing a measured amount of epoxy in the hemispherical cavity. Basic hobby supply mold release is used to ensure the epoxy layer does not adhere to the mold. A thin layer of mold release is also applied to the hemisphere seat before the hemisphere is mounted in the mold. The thin layer of mold release has enough tension to support the weight of the hemisphere. The hemisphere mounting sleeve is inserted into the mold, and the epoxy cures in contact with the hemisphere.

Error in the coating thickness could occur due to incorrect cavity radius or misalignments of the hemisphere to the mold cavity. Misalignments can happen in two directions, parallel or perpendicular to the hemisphere mounting sleeve. Figure 6.7 illustrates extreme examples of these misalignments and their effect on the layer thickness.

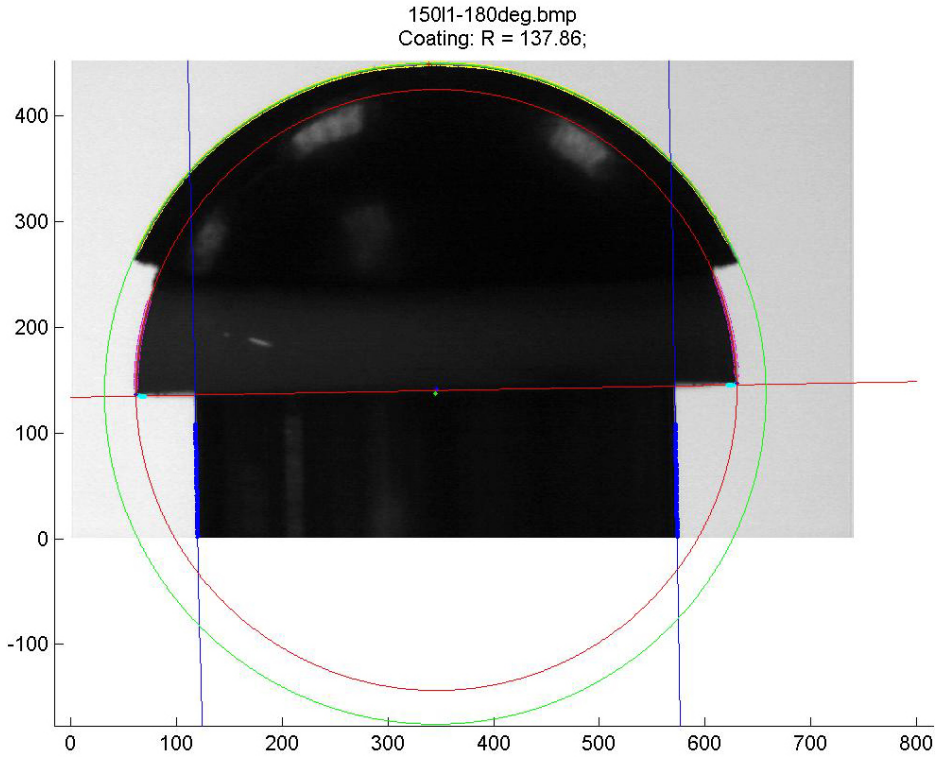

Figure 6.8: Molded layer inspection. The tolerances of the molded part are measured from fits to this optical comparator image. The edge contours of the hemisphere (pink) and coating surface (yellow) are fit with circles. The center of the layer circle (green) is visible, whereas the center of the hemisphere circle is obscured in the plot. The radii-fit and circle centers put bounds on coating layer thickness errors. Finally, the image dimension scaling is checked by the width of a precision machined pedestal (blue contour points).

To inspect a molded part, we use optical comparator images and fit the AR coating contours. Figure 6.8 shows an example image with the inspection results over plotted. As seen in the image, the hemisphere and coating edge contours are fit with circles. Deviation of the edge contour from the fit circle determines the roundness and radius variation. The centers of the fit circles are also shown. For the ideal coatings, the circles would be concentric. The vertical and horizontal offset of the circle centers determines the magnitude of misalignment errors of Figure 6.7. As the direction of the horizontal misalignment is not known, these two-dimensional shadow images are taken at a range of angles.

Inspection indicates that we can hit a tolerance of $0.001''$ or better in the vertical and horizontal alignment. The sphericity of the mold cavity is also quite good, as seen in Figure 6.9. The molded part is just as round as the thermoformed PEI

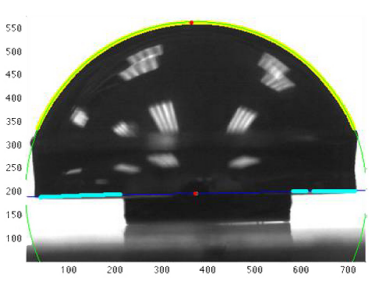

(a) PEI Coating Image

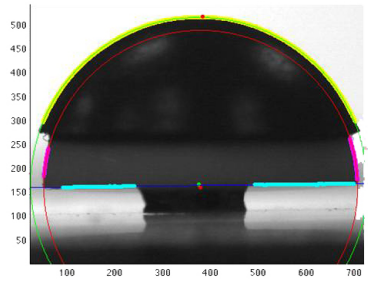

(b) Molded Coating Image

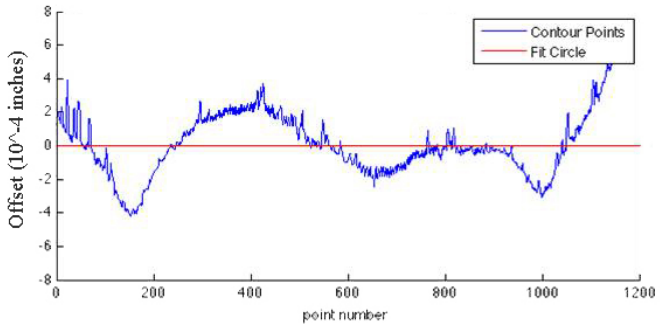

(c) PEI Radius Variation

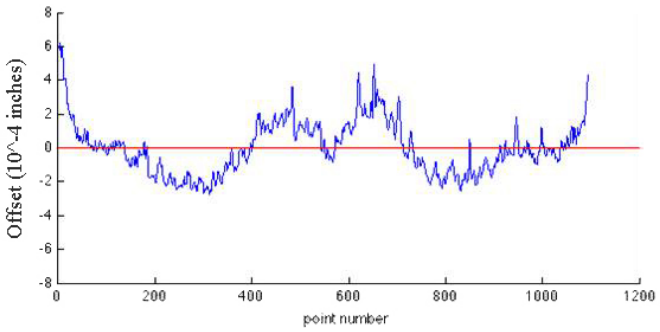

(d) Molded Stycast Radius Variation

Figure 6.9: Roundness inspection. The roundness of the (a) PEI POLARBEAR-I coating is compared to the roundness of (b) a molded epoxy coating. The edge contours in (a) and (b) are fit by a circles. The difference in radial distance between the best fit circle and the edge contour is plotted for each image in (c) and (d). The radial variation for both types of coatings is less than 0.0004″, except at the edges where it is as large as 0.0006″. This type of analysis was done for both coatings using images at several azimuthal angles. Only one angle for each coating is shown here.

POLARBEAR-I coatings, both of which have a radial variation of order of less than 0.0005″. We are currently studying the effect of AR coating tolerances on beam properties using the electromagnetic simulator HFSS.

Surprisingly, we found the most difficult part of the molding scheme to be getting an accurate cavity radius. The cavity is currently being made with a ball end mill. Ball end mills are typically used for their shaft diameter, not the curvature of the cutting edge at the tip. To achieve the correct end mill radius, we are having suites of end mills manufactured[4]. A suite of several end mills are ground in one session with 0.0005″ radius increments between end mills. The initial radius setting may be off target by up to 0.002″, but with this incremented set one of the end mills will be within 0.0005″ of the design value. To select the best end mill of the suite, we measure molded parts made from each end mill before making the final hemisphere mold. Collaborators at UCSD are also attempting mold fabrication on a CNC lathe, but at this time they have not matched the accuracy of our end mill method.

Two-layer coating: Stycast 2850/Stycast 1090

The index values for Stycast 2850 and Stycast 1090 are nearly ideal for a two-layer AR coating on silicon or alumina. The combination is a viable candidate for two-layer AR coatings and is planned for use on the lenslets of POLARBEAR-II , a two band instrument.

The expected reflectance of a flat two-layer Stycast 2850/1090 coating is shown in Figure 6.10. It is plotted along with the reflectance of a quarter wavelength coating for reference. A flat two-layer AR coating of 2850/1090 was fabricated and tested on a flat alumina surface by Aritoki Suzuki and Darin Rosen at UC Berkeley. Spectroscopy showed excellent agreement with the expected passband. These results are in preparation for publication.

The coating has also been molded onto a alumina hemisphere and it was thermally cycled successfully. Thermal cycling is a concern because high dielectric materials typically used in millimeter wave optics, such as silicon and alumina, have low coefficients of thermal contraction. In contrast, plastics and epoxies used for AR coatings typically have high values of thermal contraction. There is mechanical stress at the adhesion interface of the optics and the AR coating. Stycast 2850 is a good choice for a first coating layer contacting the lenslet, as it is doped with alumina particulates to reduce the bulk thermal contraction. Stycast 2950 is used as a low temperature epoxy designed to match the thermal contraction of metals.

The two-layer coating prototypes survived upwards of 18 nitrogen dunk tests. Eleven AR coated alumina hemispheres were tested, and only one failed on the 18th test. The other ten samples lasted ten more cycles without failure. A fabricated two-layer coating is seen in Figure 6.11.

[4]Pacific Reamer, Oakland, CA

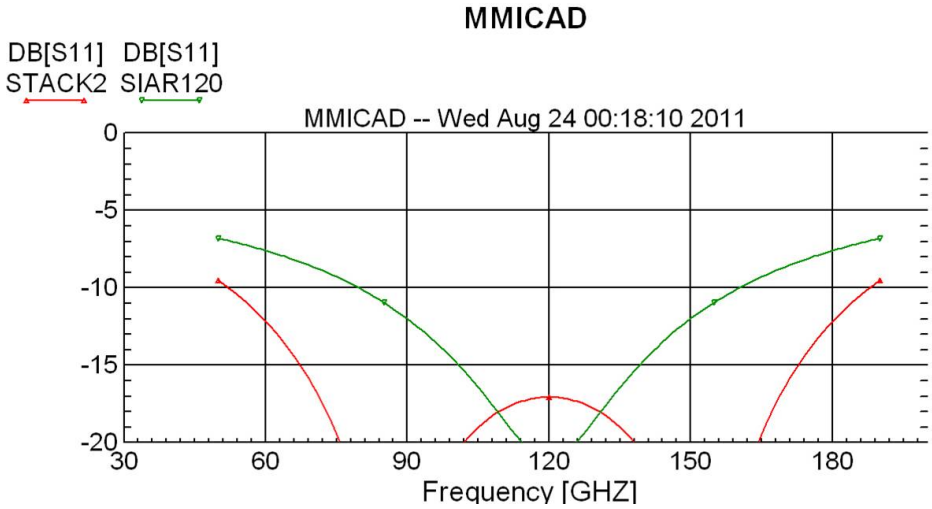

Figure 6.10: Reflectance curves. The two-layer Stycast 2850/1090 reflectance (red) is plotted for comparison with an ideal quarter wavelength coating at the band center (green) on a flat silicon interface. For the two-layer coating, index values $n_{2850} = 2.2$ and $n_{1090} = 1.4$ were used. Each layer was a quarter wavelength in the medium. The single layer coating had index $n_{ideal} = 1.68$.

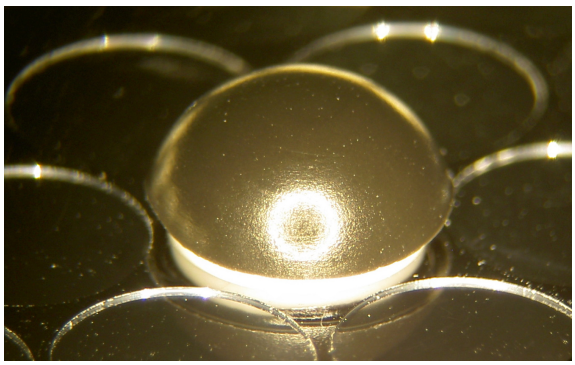

Figure 6.11: Two-layer molded coating. The Stycast 2850 / Stycast 1090 two-layer coating is shown here applied to a hemispherical surface. The low index layer, 1090, is visible here. The 2850 layer is concealed. The layers were applied in series to an alumina lens, seen in white, and the lens is seated in a silicon seating wafer for display purposes.

Tunable Epoxy Index

The nearly ideal index values of Stycast 1090 and 2850 were a lucky coincidence for use with our two-layer coating. To move to wider bandwidth AR coatings, more dielectric layers can be used. For this, we will need to have control over the layer indices.

Epoxy can be used as a base ingredient and binding agent to which we can add fillers for a tunable index. Aritoki Suzuki and Darin Rosen are currently working on high dielectric tuning. Low index tuning has been achieved with the addition of hollow microspheres.

For the low index doping test, hobby-grade microspheres were used with the assumption that the volume of the microsphere was vacuum or nitrogen, and that the glass wall of the microsphere was thin enough to be negligible. That assumption held up well for index tests of loaded epoxy. The microspheres were examined by microscope, and the size was typically less than 150 μm with occaisonal 300 μm outliers. Based on scattering theory and measurements [2] [80], we estimate a requirement of at least $\lambda/d = 10$, corresponding to a 200 μm sphere diameter. If used as part of a fielding instrument, high grade microspheres can be obtained. High grade microspheres would have some promised specification for maximum wall thickness and maximum sphere size.

The mixing ratio used a simple volume averaged index value. A more complicated treatment can be done using effective medium theory, but this simple weighted average was in good agreement with the observed index. The sample measured used 100 parts of Stycast 1266 to 75 parts microspheres by volume. The volume measurement was made in a graduated beaker, where the 1266 was added first (to 100) and the microspheres were mixed in until a level of 175 was reached. The high mixing ratio created a thick substance, so degassing of the final product was not done. Based on the index of Stycast 1266, $n_{1266} = 1.68$ [57], the expected index value based on a simple volume average would be:

$$n_{eff} = n_{vacuum}\frac{75}{100+75} + n_{1266}\frac{100}{100+75} = 1.39 \tag{6.3}$$

The resultant optical index reached was $n = 1.38$, measured warm from 75 to 175 GHz. Reduction of the optical index via microsphere doping seems viable based on this test.

Additionally, a two-layer coating with Stycast 2850 and microsphere-doped 1266 was fabricated. This coating survived thermal cycling without damage to the microsphere layer. Figure 6.12 shows this two-layer coating on an alumina hemisphere.

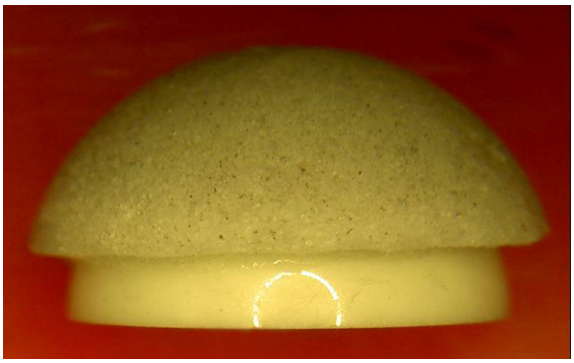

Figure 6.12: Two-layer molded coating. The Stycast 2850 / microsphere-doped Stycast 1266 two-layer coating is shown here applied to a hemispherical surface.

6.4 Concluding remarks

The epoxy molding method shows great promise to be a scalable and robust broadband AR coating technology. It can be used for high curvature focal plane lenslets as well as other reimaging optics. The ability to tune the epoxy index with dopants will allow broadband coatings with an arbitrary number of layers. Broadband AR coating technology will reduce polarized reflections and aid future precision measurements of CMB polarization.

Bibliography

[1] P. A. R. Ade, G. Pisano, C. Tucker, and S. Weaver. A review of metal mesh filters. In *Society of Photo-Optical Instrumentation Engineers (SPIE) Conference Series*, volume 6275 of *Society of Photo-Optical Instrumentation Engineers (SPIE) Conference Series*, July 2006.

[2] K. R. Armstrong and F. J. Low. Far-infrared filters utilizing small particle scattering and antireflection coatings. *Applied Optics*, 13:425–430, 1974.

[3] K. Arnold, P. A. R. Ade, A. E. Anthony, F. Aubin, D. Boettger, J. Borrill, C. Cantalupo, M. A. Dobbs, J. Errard, D. Flanigan, A. Ghribi, N. Halverson, M. Hazumi, W. L. Holzapfel, J. Howard, P. Hyland, A. Jaffe, B. Keating, T. Kisner, Z. Kermish, A. T. Lee, E. Linder, M. Lungu, T. Matsumura, N. Miller, X. Meng, M. Myers, H. Nishino, R. O'Brient, D. O'Dea, C. Reichardt, I. Schanning, A. Shimizu, C. Shimmin, M. Shimon, H. Spieler, B. Steinbach, R. Stompor, A. Suzuki, T. Tomaru, H. T. Tran, C. Tucker, E. Quealy, P. L. Richards, and O. Zahn. The POLARBEAR CMB polarization experiment. In *Society of Photo-Optical Instrumentation Engineers (SPIE) Conference Series*, volume 7741 of *Society of Photo-Optical Instrumentation Engineers (SPIE) Conference Series*, July 2010.

[4] K.S. Arnold. Design and Deployment of the POLARBEAR Cosmic Microwave Background Polarization Experiment. University of California Berkeley Doctoral Dissertation, Fall 2010.

[5] N.W. Ashcroft and N.D. Mermin. *Solid State Physics*. Saunders College, Philadelphia, 1976.

[6] J. Aumont, L. Conversi, C. Thum, H. Wiesemeyer, E. Falgarone, J. F. Macías-Pérez, F. Piacentini, E. Pointecouteau, N. Ponthieu, J. L. Puget, C. Rosset, J. A. Tauber, and M. Tristram. Measurement of the Crab nebula polarization at 90 GHz as a calibrator for CMB experiments. *Astronomy and Astrophysics*, 514:A70, May 2010.

[7] IJ Bahl and R. Garg. Simple and accurate formulas for a microstrip with finite strip thickness. *Proceedings of the IEEE*, 65(11):1611–1612, 1977.

[8] D. Baumann, A. Cooray, S. Dodelson, J. Dunkley, A. A. Fraisse, M. G. Jackson, A. Kogut, L. M. Krauss, K. M. Smith, and M. Zaldarriaga. A Mission to Map our Origins. In S. Dodelson, D. Baumann, A. Cooray, J. Dunkley, A. Fraisse, M. G. Jackson, A. Kogut, L. Krauss, M. Zaldarriaga, and K. Smith, editors, *American Institute of Physics Conference Series*, volume 1141 of *American Institute of Physics Conference Series*, pages 3–9, June 2009.

[9] D. Baumann, M. G. Jackson, P. Adshead, A. Amblard, A. Ashoorioon, N. Bartolo, R. Bean, M. Beltrán, F. de Bernardis, S. Bird, X. Chen, D. J. H. Chung, L. Colombo, A. Cooray, P. Creminelli, S. Dodelson, J. Dunkley, C. Dvorkin, R. Easther, F. Finelli, R. Flauger, M. P. Hertzberg, K. Jones-Smith, S. Kachru, K. Kadota, J. Khoury, W. H. Kinney, E. Komatsu, L. M. Krauss, J. Lesgourgues, A. Liddle, M. Liguori, E. Lim, A. Linde, S. Matarrese, H. Mathur, L. McAllister, A. Melchiorri, A. Nicolis, L. Pagano, H. V. Peiris, M. Peloso, L. Pogosian, E. Pierpaoli, A. Riotto, U. Seljak, L. Senatore, S. Shandera, E. Silverstein, T. Smith, P. Vaudrevange, L. Verde, B. Wandelt, D. Wands, S. Watson, M. Wyman, A. Yadav, W. Valkenburg, and M. Zaldarriaga. Probing Inflation with CMB Polarization. In S. Dodelson, D. Baumann, A. Cooray, J. Dunkley, A. Fraisse, M. G. Jackson, A. Kogut, L. Krauss, M. Zaldarriaga, and K. Smith, editors, *American Institute of Physics Conference Series*, volume 1141 of *American Institute of Physics Conference Series*, pages 10–120, June 2009.

[10] P. Y. Bely. *The Design and Construction of Large Optical Telescopes*. Springer, 2003.

[11] C. L. Bennett, A. J. Banday, K. M. Gorski, G. Hinshaw, P. Jackson, P. Keegstra, A. Kogut, G. F. Smoot, D. T. Wilkinson, and E. L. Wright. Four-Year COBE DMR Cosmic Microwave Background Observations: Maps and Basic Results. *The Astrophysical Journal*, 464:L1, June 1996.

[12] C. L. Bennett, R. S. Hill, G. Hinshaw, M. R. Nolta, N. Odegard, L. Page, D. N. Spergel, J. L. Weiland, E. L. Wright, M. Halpern, N. Jarosik, A. Kogut, M. Limon, S. S. Meyer, G. S. Tucker, and E. Wollack. First-Year Wilkinson Microwave Anisotropy Probe (WMAP) Observations: Foreground Emission. *The Astrophysical Journal Supplement Series*, 148:97–117, September 2003.

[13] B. A. Benson, S. E. Church, P. A. R. Ade, J. J. Bock, K. M. Ganga, J. R. Hinderks, P. D. Mauskopf, B. Philhour, M. C. Runyan, and K. L. Thompson. Peculiar Velocity Limits from Measurements of the Spectrum of the Sunyaev-Zeldovich Effect in Six Clusters of Galaxies. *The Astrophysical Journal*, 592:674–691, August 2003.

[14] M. Betoule, E. Pierpaoli, J. Delabrouille, M. Le Jeune, and J.-F. Cardoso. Measuring the tensor to scalar ratio from CMB B-modes in the presence of foregrounds. *Astronomy and Astrophysics*, 503:691–706, September 2009.

[15] R.S. Bhatia and S.T. Chase. A three-stage helium sorption refrigerator for cooling of infrared detectors to 280 mK. *Cryogenics*, 40, October 2000.

[16] D. C.-J. Bock, A. D. Bolatto, D. W. Hawkins, A. J. Kemball, J. W. Lamb, R. L. Plambeck, M. W. Pound, S. L. Scott, D. P. Woody, and M. C. H. Wright. First results from CARMA: the combined array for research in millimeter-wave astronomy. In *Society of Photo-Optical Instrumentation Engineers (SPIE) Conference Series*, volume 6267 of *Society of Photo-Optical Instrumentation Engineers (SPIE) Conference Series*, July 2006.

[17] E. Calabrese, A. Slosar, A. Melchiorri, G. F. Smoot, and O. Zahn. Cosmic microwave weak lensing data as a test for the dark universe. *Phys. Rev. D.*, 77(12):123531, June 2008.

[18] CAPMAP. http://quiet.uchicago.edu/capmap/a.htm.

[19] H. C. Chiang, P. A. R. Ade, D. Barkats, J. O. Battle, E. M. Bierman, J. J. Bock, C. D. Dowell, L. Duband, E. F. Hivon, W. L. Holzapfel, V. V. Hristov, W. C. Jones, B. G. Keating, J. M. Kovac, C. L. Kuo, A. E. Lange, E. M. Leitch, P. V. Mason, T. Matsumura, H. T. Nguyen, N. Ponthieu, C. Pryke, S. Richter, G. Rocha, C. Sheehy, Y. D. Takahashi, J. E. Tolan, and K. W. Yoon. Measurement of Cosmic Microwave Background Polarization Power Spectra from Two Years of BICEP Data. *The Astrophysical Journal*, 711:1123–1140, March 2010.

[20] E. Collett. *Polarized light: fundamentals and applications*. Optical engineering. Marcel Dekker, 1993.

[21] A. Deinega, I. Valuev, B. Potapkin, and Y. Lozovik. Minimizing light reflection from dielectric textured surfaces. *Journal of the Optical Society of America A*, 28:770, May 2011.

[22] Scott Dodelson. *Modern Cosmology*. Academic Press, 2003.

[23] C. Dragone. Offset multireflector antennas with perfect pattern symmetry and polarization discrimination. *AT T Technical Journal*, 57:2663–2684, September 1978.

[24] J. Dunkley, A. Amblard, C. Baccigalupi, M. Betoule, D. Chuss, A. Cooray, J. Delabrouille, C. Dickinson, G. Dobler, J. Dotson, H. K. Eriksen, D. Finkbeiner, D. Fixsen, P. Fosalba, A. Fraisse, C. Hirata, A. Kogut, J. Kristiansen,

C. Lawrence, A. M. Magalha˜Es, M. A. Miville-Deschenes, S. Meyer, A. Miller, S. K. Naess, L. Page, H. V. Peiris, N. Phillips, E. Pierpaoli, G. Rocha, J. E. Vaillancourt, and L. Verde. Prospects for polarized foreground removal. In S. Dodelson, D. Baumann, A. Cooray, J. Dunkley, A. Fraisse, M. G. Jackson, A. Kogut, L. Krauss, M. Zaldarriaga, and K. Smith, editors, *American Institute of Physics Conference Series*, volume 1141 of *American Institute of Physics Conference Series*, pages 222–264, June 2009.

[25] J. Errard, F. Stivoli, and R. Stompor. Framework for performance forecasting and optimization of cmb *b*-mode observations in the presence of astrophysical foregrounds. *Phys. Rev. D*, 84:063005, Sep 2011.

[26] D. F. Filipovic, G. P. Gauthier, S. Raman, and G. M. Rebeiz. Off-axis properties of silicon and quartz dielectric lens antennas. *IEEE Transactions on Antennas and Propagation*, 45:760–766, May 1997.

[27] D. F. Filipovic, S. S. Gearhart, and G. M. Rebeiz. Double-slot antennas on extended hemispherical and elliptical silicon dielectric lenses. *IEEE Transactions on Microwave Theory Techniques*, 41:1738–1749, October 1993.

[28] D. P. Finkbeiner, M. Davis, and D. J. Schlegel. Extrapolation of Galactic Dust Emission at 100 Microns to Cosmic Microwave Background Radiation Frequencies Using FIRAS. *The Astrophysical Journal*, 524:867–886, October 1999.

[29] J.W. Goodman. *Introduction to Fourier Optics*. Roberts and Company, 3rd edition, 2005.

[30] M. J. Griffin, J. J. Bock, and W. K. Gear. Relative performance of filled and feedhorn-coupled focal-plane architectures. *Applied Optics*, 41:6543–6554, November 2002.

[31] M. Halpern, H. P. Gush, E. Wishnow, and V. de Cosmo. Far infrared transmission of dielectrics at cryogenic and room temperatures - Glass, Fluorogold, Eccosorb, Stycast, and various plastics. *Applied Optics*, 25:565–570, February 1986.

[32] N.W. Halverson. Aperture Efficiency and Mapping Speed. APEX-SZ Experiment Memo no. APEX-SZ-20020429a, Mar 2005.

[33] S. Hanany and P. Rosenkranz. Polarization of the atmosphere as a foreground for cosmic microwave background polarization experiments. *New Astronomy Reviews*, 47:1159–1165, December 2003.

[34] K. Hattori, S. Ariyoshi, M. Hazumi, H. Ishino, A. Kibayashi, S. Mima, C. Otani, N. Satoh, T. Tomaru, M. Yoshida, and H. Watanabe. Novel Frequency-Domain

Multiplexing MKID Readout for the LiteBIRD Satellite. *Journal of Low Temperature Physics*, 167:671–677, June 2012.

[35] M. Hazumi. Future CMB Polarization Measurements and Japanese Contributions. *Progress of Theoretical Physics Supplement*, 190:75–89, 2011.

[36] E. Hecht. *Optics*. Addison Wesley Longman, Inc., 3rd edition, 1998.

[37] W. Hu. CMB Tutorials. http://background.uchicago.edu/index.html.

[38] W. Hu and M. White. A CMB polarization primer. *online publication*, 2:323–344, October 1997.

[39] W. Hu and M. White. The Cosmic Symphony. *Scientific American*, 290(2):020000–53, February 2004.

[40] H.W. Johnson and M. Graham. *High-speed digital design: a handbook of black magic*. Prentice-Hall, Inc. Upper Saddle River, NJ, USA, 1993.

[41] S. Joudaki. Constraints on Neutrino Mass and Light Degrees of Freedom in Extended Cosmological Parameter Spaces. *ArXiv e-prints*, January 2012.

[42] M. Kamionkowski and A. Kosowsky. The Cosmic Microwave Background and Particle Physics. *Annual Review of Nuclear and Particle Science*, 49:77–123, 1999.

[43] B. Keating, P. Timbie, A. Polnarev, and J. Steinberger. Large Angular Scale Polarization of the Cosmic Microwave Background Radiation and the Feasibility of Its Detection. *Astrophysical Journal*, 495:580, March 1998.

[44] J.B. Keller. *How Dark is the Shadow of a Round-ended Screen?* Research reports of New York University Institute of Mathematical Sciences, Division of electromagnetic research. 1958.

[45] Z. Kermish and *et al.* The POLARBEAR Experiment. In *Society of Photo-Optical Instrumentation Engineers (SPIE) Conference Series*, Society of Photo-Optical Instrumentation Engineers (SPIE) Conference Series, 2012.

[46] Z.D. Kermish. The POLARBEAR experiment: Design and Characterization. University of California Berkeley Doctoral Dissertation, Spring 2012.

[47] E. Komatsu, K. M. Smith, J. Dunkley, C. L. Bennett, B. Gold, G. Hinshaw, N. Jarosik, D. Larson, M. R. Nolta, L. Page, D. N. Spergel, M. Halpern, R. S. Hill, A. Kogut, M. Limon, S. S. Meyer, N. Odegard, G. S. Tucker, J. L. Weiland, E. Wollack, and E. L. Wright. Seven-year Wilkinson Microwave Anisotropy Probe (WMAP) Observations: Cosmological Interpretation. *The Astrophysical Journal Supplement*, 192:18, February 2011.

[48] A. Kosowsky. Introduction to microwave background polarization. *New Astronomy Reviews*, 43:157–168, July 1999.

[49] J. M. Kovac. *Detection of polarization in the cosmic microwave background using DASI.* PhD thesis, THE UNIVERSITY OF CHICAGO, June 2004.

[50] C. L. Kuo, J. J. Bock, J. A. Bonetti, J. Brevik, G. Chattopadhyay, P. K. Day, S. Golwala, M. Kenyon, A. E. Lange, H. G. LeDuc, H. Nguyen, R. W. Ogburn, A. Orlando, A. Transgrud, A. Turner, G. Wang, and J. Zmuidzinas. Antenna-coupled TES bolometer arrays for CMB polarimetry. In *Society of Photo-Optical Instrumentation Engineers (SPIE) Conference Series*, volume 7020 of *Society of Photo-Optical Instrumentation Engineers (SPIE) Conference Series*, August 2008.

[51] T. Lanting, M. Dobbs, H. Spieler, A. T. Lee, and Y. Yamamoto. Linearized superconducting quantum interference device array for high bandwidth frequency-domain readout multiplexing. *Review of Scientific Instruments*, 80(9):094501, September 2009.

[52] T. M. Lanting. *Multiplexed readout of superconducting bolometers for cosmological observations.* PhD thesis, University of California, Berkeley, 2006.

[53] T. M. Lanting, H.-M. Cho, J. Clarke, M. Dobbs, A. T. Lee, M. Lueker, P. L. Richards, A. D. Smith, and H. G. Spieler. Frequency domain multiplexing for bolometer arrays. *Nuclear Instruments and Methods in Physics Research A*, 520:548–550, March 2004.

[54] T. M. Lanting, H.-M. Cho, J. Clarke, W. L. Holzapfel, A. T. Lee, M. Lueker, P. L. Richards, M. A. Dobbs, H. Spieler, and A. Smith. Frequency-domain multiplexed readout of transition-edge sensor arrays with a superconducting quantum interference device. *Applied Physics Letters*, 86(11):112511, March 2005.

[55] T.M. Lanting, H.M. Cho, J. Clarke, M. Dobbs, A.T. Lee, P.L. Richards, H. Spieler, and A. Smith. Frequency-domain multiplexing for large-scale bolometer arrays. In *Proceedings of SPIE*, volume 4855, page 172. SPIE, 2003.

[56] D. Larson, J. Dunkley, G. Hinshaw, E. Komatsu, M. R. Nolta, C. L. Bennett, B. Gold, M. Halpern, R. S. Hill, N. Jarosik, A. Kogut, M. Limon, S. S. Meyer, N. Odegard, L. Page, K. M. Smith, D. N. Spergel, G. S. Tucker, J. L. Weiland, E. Wollack, and E. L. Wright. Seven-year Wilkinson Microwave Anisotropy Probe (WMAP) Observations: Power Spectra and WMAP-derived Parameters. *The Astrophysical Journal Supplement*, 192:16, February 2011.

[57] J. Lau, J. Fowler, T. Marriage, L. Page, J. Leong, E. Wishnow, R. Henry, E. Wollack, M. Halpern, D. Marsden, and G. Marsden. Millimeter-wave antireflection coating for cryogenic silicon lenses. *Applied Optics*, 45:3746–3751, June 2006.

[58] A. T. Lee, P. L. Richards, S. W. Nam, B. Cabrera, and K. D. Irwin. A superconducting bolometer with strong electrothermal feedback. *Applied Physics Letters*, 69:1801–1803, September 1996.

[59] A.T. Lee, P. Ade, A. Anthony, K. Arnold, D. Boetger, J. Borrill, C. Cantalupo, M. A. Dobbs, J. Errard, N. Halverson, M. Hazumi, W. L. Holzapfel, J. Howard, P. Hyland, A. Jaffe, B. Keating, T. Kisner, Z. Kermish, E. Linder, N. Miller, M. Myers, H. Paar, C. Reichardt, I. , Schanning, M. Shimon, H. Spieler, B. Steinbach, R. Stompor, T. Tomaru, H. T. Tran, C. Tucker, E. Quealy, P. L. Richards, and O. Zahn. Mitigation of systematic errors in the polarbear cmb polarization experiment. presented at CMBPol Conference: Mitigating Systematic Errors in Space-Based CMB Polarization Measurements, July 2008.

[60] A. Lewis and A. Challinor. Weak gravitational lensing of the CMB. *Physics Reports*, 429:1–65, June 2006.

[61] A.R. Liddle and D.H. Lyth. *Cosmological Inflation and Large-Scale Structure*. Cambridge University Press, 2000.

[62] J. C. Mather. Broad-band flared horn with low sidelobes. *IEEE Transactions on Antennas and Propagation*, 29:967–969, November 1981.

[63] J. C. Mather, E. S. Cheng, D. A. Cottingham, R. E. Eplee, Jr., D. J. Fixsen, T. Hewagama, R. B. Isaacman, K. A. Jensen, S. S. Meyer, P. D. Noerdlinger, S. M. Read, L. P. Rosen, R. A. Shafer, E. L. Wright, C. L. Bennett, N. W. Boggess, M. G. Hauser, T. Kelsall, S. H. Moseley, Jr., R. F. Silverberg, G. F. Smoot, R. Weiss, and D. T. Wilkinson. Measurement of the cosmic microwave background spectrum by the COBE FIRAS instrument. *The Astrophysical Journal*, 420:439–444, January 1994.

[64] Y. Mizugutch, M. Akagawa, and H. Yokoi. Offset Dual Reflector Antenna. *Antennas and Propagation Society International Symposium (IEEE 1976)*, 14:2–5, October 1976.

[65] M. D. Niemack, Y. Zhao, E. Wollack, R. Thornton, E. R. Switzer, D. S. Swetz, S. T. Staggs, L. Page, O. Stryzak, H. Moseley, T. A. Marriage, M. Limon, J. M. Lau, J. Klein, M. Kaul, N. Jarosik, K. D. Irwin, A. D. Hincks, G. C. Hilton, M. Halpern, J. W. Fowler, R. P. Fisher, R. Dünner, W. B. Doriese, S. R. Dicker, M. J. Devlin, J. Chervenak, B. Burger, E. S. Battistelli, J. Appel, M. Amiri, C. Allen, and A. M. Aboobaker. A Kilopixel Array of TES Bolometers for ACT: Development, Testing, and First Light. *Journal of Low Temperature Physics*, 151:690–696, May 2008.

[66] R. O'Brient, P. Ade, K. Arnold, J. Edwards, G. Engargiola, W. Holzapfel, A. T. Lee, X. F. Meng, M. Myers, E. Quealy, G. Rebeiz, P. Richards, and A. Suzuki. A

dual-polarized multichroic antenna-coupled TES bolometer for terrestrial CMB Polarimetry. In *Society of Photo-Optical Instrumentation Engineers (SPIE) Conference Series*, volume 7741 of *Society of Photo-Optical Instrumentation Engineers (SPIE) Conference Series*, July 2010.

[67] R. O'Brient, P. Ade, K. Arnold, J. Edwards, G. Engargiola, W. Holzapfel, A. T. Lee, M. Myers, G. Rebeiz, P. Richards, and A. Suzuki. A Log-Periodic Channelizer for Multichroic Antenna-Coupled TES-Bolometers. *IEEE Transactions on Applied Superconductivity*, 21:180–183, June 2011.

[68] R. O'Brient, J. Edwards, K. Arnold, G. Engargiola, W. Holzapfel, A. T. Lee, M. Myers, E. Quealy, G. Rebeiz, P. Richards, H. Spieler, and H. Tran. Sinuous antennas for cosmic microwave background polarimetry. In *Society of Photo-Optical Instrumentation Engineers (SPIE) Conference Series*, volume 7020 of *Society of Photo-Optical Instrumentation Engineers (SPIE) Conference Series*, August 2008.

[69] R.C. O'Brient. A Log-Periodic Focal-Plane Architecture for Cosmic Microwave Background Polarimetry. University of California Berkeley Doctoral Dissertation, Fall 2010.

[70] S. Paine. The AM Atmospheric Model. SMA technical memo, no. 152, Feb 2012.

[71] J.A. Peacock. *Cosmological Physics*. World Publishing Corporation, 1999.

[72] Planck HFI Core Team, P. A. R. Ade, N. Aghanim, R. Ansari, M. Arnaud, M. Ashdown, J. Aumont, A. J. Banday, M. Bartelmann, J. G. Bartlett, E. Battaner, K. Benabed, A. Benoît, J.-P. Bernard, M. Bersanelli, R. Bhatia, J. J. Bock, J. R. Bond, J. Borrill, F. R. Bouchet, F. Boulanger, T. Bradshaw, E. Bréelle, M. Bucher, P. Camus, J.-F. Cardoso, A. Catalano, A. Challinor, A. Chamballu, J. Charra, M. Charra, R.-R. Chary, C. Chiang, S. Church, D. L. Clements, S. Colombi, F. Couchot, A. Coulais, C. Cressiot, B. P. Crill, M. Crook, P. de Bernardis, J. Delabrouille, J.-M. Delouis, F.-X. Désert, K. Dolag, H. Dole, O. Doré, M. Douspis, G. Efstathiou, P. Eng, C. Filliard, O. Forni, P. Fosalba, J.-J. Fourmond, K. Ganga, M. Giard, D. Girard, Y. Giraud-Héraud, R. Gispert, K. M. Górski, S. Gratton, M. Griffin, G. Guyot, J. Haissinski, D. Harrison, G. Helou, S. Henrot-Versillé, C. Hernández-Monteagudo, S. R. Hildebrandt, R. Hills, E. Hivon, M. Hobson, W. A. Holmes, K. M. Huffenberger, A. H. Jaffe, W. C. Jones, J. Kaplan, R. Kneissl, L. Knox, G. Lagache, J.-M. Lamarre, P. Lami, A. E. Lange, A. Lasenby, A. Lavabre, C. R. Lawrence, B. Leriche, C. Leroy, Y. Longval, J. F. Macías-Pérez, T. Maciaszek, C. J. MacTavish, B. Maffei, N. Mandolesi, R. Mann, B. Mansoux, S. Masi, T. Matsumura, P. McGehee, J.-B. Melin, C. Mercier, M.-A. Miville-Deschênes, A. Moneti, L. Montier, D. Mortlock, A. Murphy, F. Nati, C. B. Netterfield, H. U. Nørgaard-Nielsen,

C. North, F. Noviello, D. Novikov, S. Osborne, C. Paine, F. Pajot, G. Patanchon, T. Peacocke, T. J. Pearson, O. Perdereau, L. Perotto, F. Piacentini, M. Piat, S. Plaszczynski, E. Pointecouteau, R. Pons, N. Ponthieu, G. Prézeau, S. Prunet, J.-L. Puget, W. T. Reach, C. Renault, I. Ristorcelli, G. Rocha, C. Rosset, G. Roudier, M. Rowan-Robinson, B. Rusholme, D. Santos, G. Savini, B. M. Schaefer, P. Shellard, L. Spencer, J.-L. Starck, P. Stassi, V. Stolyarov, R. Stompor, R. Sudiwala, R. Sunyaev, J.-F. Sygnet, J. A. Tauber, C. Thum, J.-P. Torre, F. Touze, M. Tristram, F. van Leeuwen, L. Vibert, D. Vibert, L. A. Wade, B. D. Wandelt, S. D. M. White, H. Wiesemeyer, A. Woodcraft, V. Yurchenko, D. Yvon, and A. Zacchei. Planck early results. IV. First assessment of the High Frequency Instrument in-flight performance. *Astronomy & Astrophysics*, 536:A4, December 2011.

[73] D.M. Pozar. *Microwave Engineering*. John Wiley & Sons, 2004.

[74] S. Radford. Site Characterization for mm/submm Astronomy (Invited Speaker). In J. Vernin, Z. Benkhaldoun, and C. Muñoz-Tuñón, editors, *Astronomical Site Evaluation in the Visible and Radio Range*, volume 266 of *Astronomical Society of the Pacific Conference Series*, pages 148–163, 2002.

[75] P. L. Richards. Bolometers for infrared and millimeter waves. *Journal of Applied Physics*, 76:1–24, July 1994.

[76] Rogers Corp. TMM Thermoset Microwave Materials Data Sheet. http://www.rogerscorp.com/documents, Rogers, CT, USA.

[77] S.S. Rosenblum, W.A. Steyert, and F.R. Fickett. A Simple Method for Producing High Conductivity Copper for Low Termperature Applications. *Cryogenics*, 17, November 1977.

[78] M. C. Runyan, P. A. R. Ade, R. S. Bhatia, J. J. Bock, M. D. Daub, J. H. Goldstein, C. V. Haynes, W. L. Holzapfel, C. L. Kuo, A. E. Lange, J. Leong, M. Lueker, M. Newcomb, J. B. Peterson, C. Reichardt, J. Ruhl, G. Sirbi, E. Torbet, C. Tucker, A. D. Turner, and D. Woolsey. ACBAR: The Arcminute Cosmology Bolometer Array Receiver. *The Astrophysical Journal Supplement Series*, 149:265–287, December 2003.

[79] G.B. Rybicki and A.P. Lightman. *Radiative Processes in Astrophysics*. Wiley-Interscience publication. Wiley, 1979.

[80] S. Sato, S. Hayakawa, T. Matsumoto, H. Matsuo, H. Murakami, K. Sakai, A. E. Lange, and P. L. Richards. Submillimeter wave low pass filters made of glass beads. *Applied Optics*, 28:4478–4481, October 1989.

[81] M. V. Sazhin, G. Sironi, and O. S. Khovanskaya. Galactic Synchrotron Foreground and the CMB Polarization Measurements. *ArXiv Astrophysics e-prints*, September 2002.

[82] D. J. Schlegel, D. P. Finkbeiner, and M. Davis. Maps of Dust Infrared Emission for Use in Estimation of Reddening and Cosmic Microwave Background Radiation Foregrounds. *Astrophysical Journal*, 500:525, June 1998.

[83] M. Shimon, B. Keating, N. Ponthieu, and E. Hivon. CMB polarization systematics due to beam asymmetry: Impact on inflationary science. *Physics Review D*, 77(8):083003, April 2008.

[84] Kendrick M. Smith, Wayne Hu, and Manoj Kaplinghat. Cosmological information from lensed cmb power spectra. *Phys. Rev. D*, 74:123002, Dec 2006.

[85] N. Stebor. Probing the Inflationary Era with the POLARBEAR Experiment. In *American Astronomical Society Meeting Abstracts*, volume 220 of *American Astronomical Society Meeting Abstracts*, page 422.04, May 2012.

[86] A. Suzuki, K. Arnold, J. Edwards, G. Engargiola, A. Ghribi, W. Holzapfel, A. Lee, X. Meng, M. Myers, R. O'Brient, E. Quealy, G. Rebeiz, and P. Richards. Multi-chroic Dual-Polarization Bolometric Focal Plane for Studies of the Cosmic Microwave Background. *Journal of Low Temperature Physics*, 167:852–858, June 2012.

[87] Y. Takahashi. BICEP ground shields. http://bicep.caltech.edu/ yuki/shield/.

[88] Y. D. Takahashi, P. A. R. Ade, D. Barkats, J. O. Battle, E. M. Bierman, J. J. Bock, H. C. Chiang, C. D. Dowell, L. Duband, E. F. Hivon, W. L. Holzapfel, V. V. Hristov, W. C. Jones, B. G. Keating, J. M. Kovac, C. L. Kuo, A. E. Lange, E. M. Leitch, P. V. Mason, T. Matsumura, H. T. Nguyen, N. Ponthieu, C. Pryke, S. Richter, G. Rocha, and K. W. Yoon. Characterization of the BICEP Telescope for High-precision Cosmic Microwave Background Polarimetry. *The Astrophysical Journal*, 711:1141–1156, March 2010.

[89] The Planck Collaboration. The Scientific Programme of Planck. *ArXiv Astrophysics e-prints*, April 2006.

[90] H. Tran, A. Lee, S. Hanany, M. Milligan, and T. Renbarger. Comparison of the crossed and the Gregorian Mizuguchi-Dragone for wide-field millimeter-wave astronomy. *Applied Optics*, 47:103–109, January 2008.

[91] T. VanDuzer and C.W. Turner. *Principles of Superconductive Devices and Circuits*. Prentice-Hall, Inc. Upper Saddle River, NJ, USA, 1998.

[92] T.L. Wilson, K. Rohlfs, and S. Hüttemeister. *Tools of Radio Astronomy*. Astronomy and Astrophysics Library. Springer, 2009.

[93] M. Zaldarriaga, L. Colombo, E. Komatsu, A. Lidz, M. Mortonson, S. P. Oh, E. Pierpaoli, L. Verde, and O. Zahn. CMBPol Mission Concept Study: Reionization Science with the Cosmic Microwave Background. *ArXiv e-prints*, November 2008.

Appendix A

Material Properties

Included here is millimeter wave spectroscopy for materials of interest for use in optical systems such as lenslets, reimaging lenses, and anti-reflection coatings. Spectroscopy data presented here was taken on a Michaelson Fourier Transform Spectrometer. The sample temperature is 1.2 Kelvin unless otherwise noted.

The transmittance fraction is determined by dividing the measured spectra with a sample in the light path by the spectra with no sample inserted in the light path. This sample-in sample-out method divides out frequency dependent features in the spectra. However, there is scattering in the data at regular intervals caused by the beam splitter minima. The Michaelson interferometer uses a beam splitter to direct light to both mirror arms of the interferometer. Reflections inside the beam splitter produce an interference pattern with zero transmitted signal at periodic intervals. The division of zero by zero causes scatter in the sample-in/sample-out measurement.

Reflections are also present within dielectric samples, causing an interference pattern in the spectra. The spacing of these Fabry-perot fringes are dependent on the thickness and index of the sample [36]. The spacing of the fringes is

$$\bar{\nu} = \frac{1}{2nd} \tag{A.1}$$

where $\bar{\nu}$ is the spacing in wavenumber (cm^{-1}), n is the optical index of the sample, and d is the thickness of the sample in cm.

Loss can be calculated via a loss tangent at some frequency, or can be modeled as a frequency dependent absorption coefficient as detailed in [31]. The frequency dependent absorption coefficient α effects the transmittance as

$$T = (1 - R)e^{-\alpha d} \tag{A.2}$$

for an oscillatory reflection $R(n, \nu, d)$ (which incorporates the Fabry-perot fringes) and an absorption coefficient

$$\alpha = a\nu^b \tag{A.3}$$

A.1 Thermoformable Plastics

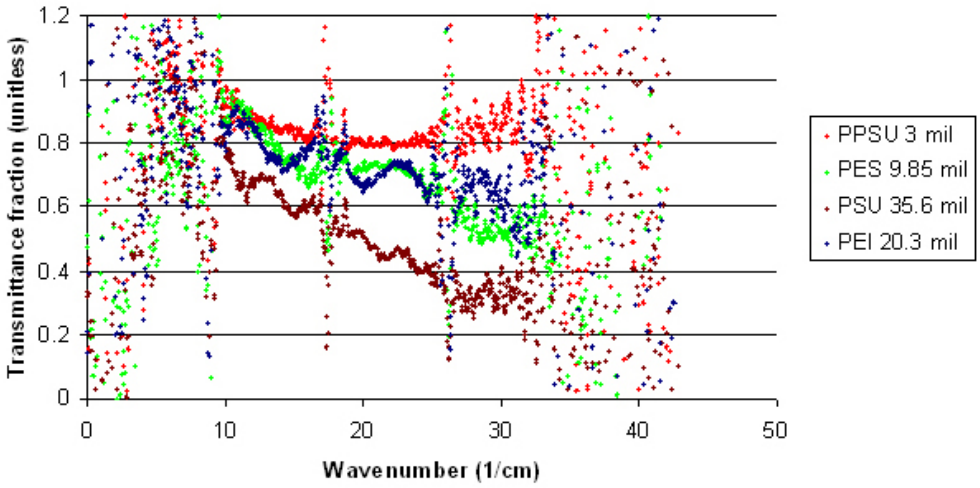

Figure A.1: Thermoformable Plastics. The dimensionless transmittance fraction is shown as a function of wavenumber, where 5 cm^{-1} corresponds to 150 GHz.

Thermoformable plastics were investigated for use in the POLARBEAR-I single frequency anti-reflection coating. Figure A.1 shows spectra of the measured samples over a range of frequencies. Of these, polyetherimide (PEI) was chosen for the POLARBEAR-I AR coating.

An AR coating of PEI on alumina was measured to determine the index close to 150 GHz, the POLARBEAR-I observation frequency. Transmittance of this coating is shown in Figure A.2. This coating was made with a flat sheet of PEI which was thicker than the POLARBEAR-I coating, so the reflection minimum was shifted to a longer wavelength (135 GHz).

The center wavelength of a quarter-wavelength coating AR coating passband is

$$\lambda = 4nd \tag{A.4}$$

where n is the index of the sample and d is the thickness. Using this relationship, the index of the PEI coating in Figure A.2 can be determined. The thickness of the coating was $0.0122''$ with a negligibly thick Stycast 1266 adhesion layer (thickness $<$ $0.0001''$). The center of the coating passband is 135 GHz. The PEI index value is thus $n = 1.8$.

Table A.1 summarizes the spectroscopy findings.

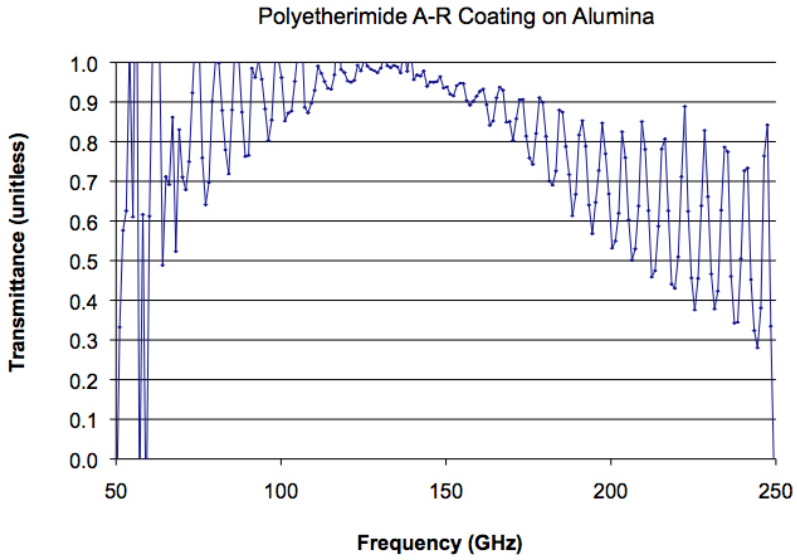

Figure A.2: PEI anti-reflection coating transmittance. Transmittance through a flat AR coated piece of alumina is shown. The AR coating is applied to both sides of the alumina. Each coating has a thickness of 0.0122″, and the alumina sample was 0.3″ thick.

Material	Index	Loss Parameters	Frequency
PPSU	–	–	10-25 1/cm
PES	–	>PEI	10-25 1/cm
PSU	1.66	∼PEI	5-25 1/cm
PEI	1.71	a=0.04, b=1.55	5-25 1/cm
PEI	1.8	–	135 GHz

Table A.1: Thermoformable Materials: Optical Properties. The first four measurements are taken from the data in Figure A.1. These measurements were taken at 1.2 K. PPSU and PES were too thin to measure fringes in the frequency range of our data. The PES sample is thinner than the PEI sample, and its level indicates more loss than PEI (assuming a comparable index). The last entry is the PEI index calculated from the AR coating in Figure A.2.

A.2 Alumina Al_2O_3

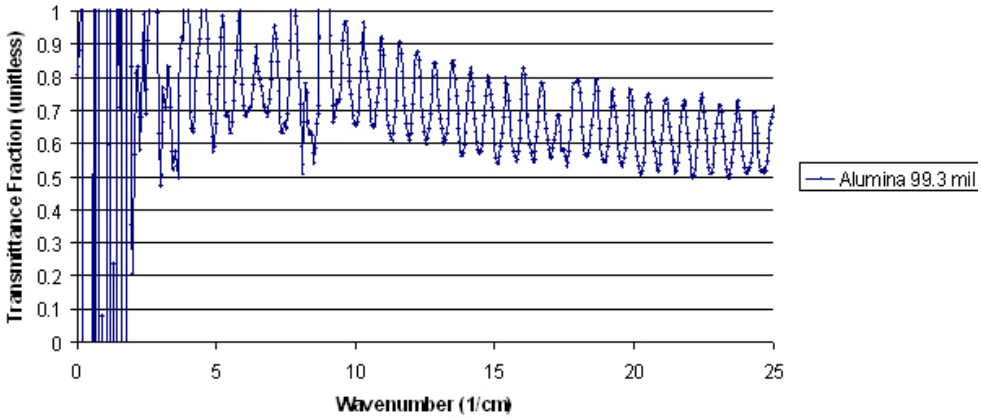

Figure A.3: Alumina Transmittance. The alumina sample was 0.0993″ thick. The Fabry-perot fringes indicate an index $n_{alumina} = 3.1$. The sample was ground from an amporphous alumina ball bearing purchased through Boca Bearings.

A.3 Silicon

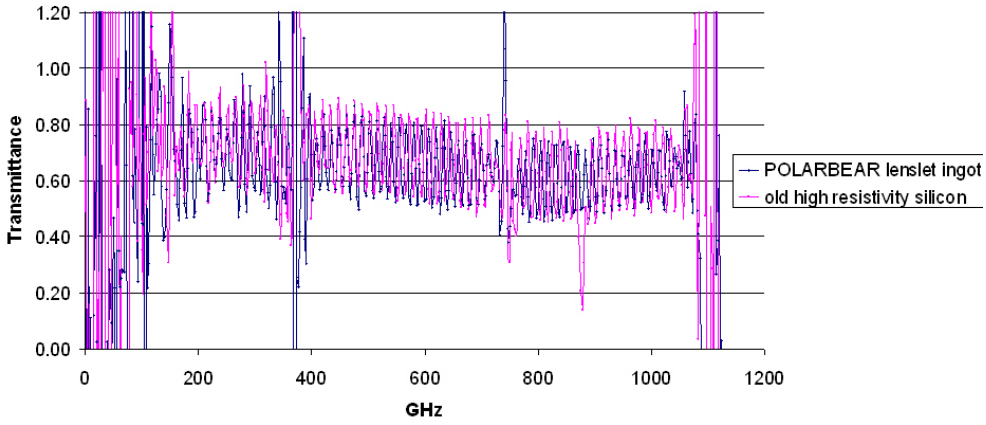

Figure A.4: High resistivity silicon transmittance. The transmittance level of silicon for the POLARBEAR-I lenslet array (from Rayotek) was compared to a known high resistivity sample. Both samples should be >1000 Ohm-cm and 5-nines pure. The transmittance graphs are relatively flat with frequency showing low loss. Assuming constant index over the frequency range showm, the optical index is $n_{silicon} = 3.37$.